



Aerodynamic drag analysis of an autonomous battery- electric truck

by

Kameel Anirood

Thesis submitted in fulfilment of the requirements for the degree

Master of Engineering in Mechanical Engineering

In the Faculty of Engineering and the Built Environment

at the

Cape Peninsula University of Technology

Supervisor: Dr Ali Rugbani

Bellville

October 2021

CPUT Copyright Information

The dissertation/thesis may not be published either in part (in scholarly, scientific or technical journals) or as a whole (as a monograph) unless permission has been obtained from the University

Declaration

I, Kameel Anirood, declare that the contents of this thesis represent my own unaided work, and the thesis has not been previously submitted for any academic exemption towards any qualification. Furthermore, it represents my own opinions and not necessarily those of the Cape Peninsula University of Technology.

Signed

Abstract

This research applies an aerodynamic drag analysis of an autonomous battery electric truck by means of using computational fluid dynamics (CFD) as a simulation tool.

Aerodynamic drag on a conventional truck at highway speeds accounts for roughly 65% of the total energy demand of the truck. This results in increased fuel usage and greenhouse gas (GHG) emissions compared to other land freight options. Battery electric trucks (BETs) are seen as a viable technology path towards reducing global GHG emissions from heavy truck-trailers. Autonomous BETs present an opportunity to further increase aerodynamic efficiency of heavy trucks, as the exterior design and smoother driving profile of such a vehicle can be more streamlined compared to conventional trucks.

The CFD simulation utilises the Reynolds-averaged Navier-Stokes (RANS) equations with a realizable $k-\varepsilon$ turbulence model and non-equilibrium wall functions to model the near-wall region of the domain. The simulation also considers the effect of a moving ground plane on aerodynamic drag. The simulation accuracy is validated against empirical results for the aerodynamic drag on the conventional generic model (GCM) truck, as tested in a wind tunnel.

It was found that an autonomous BET can reduce aerodynamic drag by approximately 18% without any modification to existing trailers, and by approximately 35.5% with the addition of low cost commercial trailer drag reduction devices.

The main conclusion of this research is that autonomous BETs can greatly reduce the overall aerodynamic drag of a truck, thereby reducing energy consumption and GHG emissions for the land freight sector. Further improvements can be made in refining the geometry of both the tractor and the trailer, as well as considering platoon formation driving for greater reductions in aerodynamic drag.

Keywords: Autonomous truck, CFD analysis, Driverless truck, Long haul BET, Zero-emission truck

Acknowledgements

I would like to express my gratitude to:

- My supervisor, Professor Ali Rugbani for his advice and guidance throughout the duration of this work.
- Professor Graeme Oliver and the CPUT mechanical engineering department for allowing me to be part of this MENG Mechanical Engineering programme.
- All of the researchers mentioned in this work, who have created the foundation upon which my work has been based.
- My partner Trisha Chunderduth, for all her patience, motivation and encouragement during this time of unprecedented difficulty.

Table of contents

Declaration	i
Abstract	ii
Acknowledgements	iii
List of symbols	x
List of tables	iv
List of Figures	v
Abbreviations	ix
Introduction	1
1.1 Background.....	1
1.2 Problem statement.....	2
1.3 Research rationale	3
1.4 Research questions	3
1.5 Research aim	3
1.6 Research significance.....	3
1.7 Delineation of the research	4
1.8 Research structure.....	4
Literature review	6
2.1 Aerodynamic drag.....	6
2.2 The freight transportation industry	7
2.3 Aerodynamic drag as a contributor to GHG emissions	9
2.3.1 Truck ancillaries.....	9
2.3.2 Mud flaps.....	11
2.3.3 Boat tails.....	12
2.3.4 Trailer side panels	13
2.3.5 Truck-trailer gap	14
2.3.6 Deflector panel	14
2.3.7 Future design approaches	15
2.4 Future design requirements.....	15
2.5 Influence of previous work on this research	17
2.6 Decarbonisation of the transport industry.....	18
2.7 The adoption of BEVs in the global vehicle market	20
2.8 Batteries	22
2.8.1 Evolution of battery capacity	23
2.8.2 Current and future battery development	23
2.9 Autonomous vehicles.....	26

2.10 Sensors used by autonomous vehicles	27
2.10.1 Cameras	27
2.10.2 Radar	28
2.10.3 Ultrasound	29
2.10.4 Lidar.....	30
2.10.5 Sensor fusion.....	30
Technical background.....	32
3.1 Introduction	32
3.2 Aerodynamics	32
3.2.1 Aerodynamic drag	33
3.2.2 Bluff bodies	34
3.2.3 Boundary layer	35
3.2.4 Boundary layer separation	36
3.2.5 Aerodynamic forces and moments.....	37
3.2.6 Aerodynamic field.....	38
3.3 Computational Fluid Dynamics (CFD)	41
3.3.1 Fluid dynamic laws of conservation	42
3.3.2 Reynolds-averaged Navier-Stokes equations.....	42
3.3.3 Turbulence modelling.....	44
3.3.4 Turbulent viscosity and turbulent diffusivity	45
3.3.5 The $k-\varepsilon$ turbulence model	46
Experimental methods and design.....	48
4.1 BET drivetrain components	48
4.2 BET drivetrain configuration	49
4.2.1 Configuration 1	49
4.2.2 Configuration 2.....	50
4.2.3 Configuration 3.....	50
4.3 BET drivetrain features	51
4.4 Evaluation of BET drivetrain configurations	52
4.5 Autonomous BET power consumption	53
4.6 Electric motor drives	54
4.6.1 Electric motor and inverter selection	55
4.7 Battery requirements	57
4.7.1 Battery selection.....	57
4.8 Transmission.....	59
4.9 Autonomous systems	61
4.10 Technology roadmap.....	62
4.10.1 Electric motor development.....	62
4.10.2 EV energy storage development.....	63

4.10.3 Inverter drive development	63
4.10.4 Policy barriers.....	63
4.10.5 Financial barriers	64
4.10.6 Autonomous BET development.....	64
4.11 Truck size constraints	67
Numerical modelling.....	68
5.1 CFD Validation Model	68
5.2 Computational domain	69
5.3 Boundary conditions.....	70
5.4 Mesh.....	70
5.5 CFD solver setup	74
5.6 GCM drag coefficient validation	74
5.7 Analysis of the GCM CFD simulation	75
Concept discussion	79
6.1 Concept autonomous BET	79
6.1.1 Concept One	79
6.1.2 Concept Two.....	81
Results and discussion	82
7.1 Concept One – Results.....	82
7.2 Concept Two – Results.....	83
7.2.1 Concept Two – Revision A.....	85
7.2.2 Concept Two – Revision B.....	87
7.2.3 Concept Two – Revision C.....	90
7.2.4 Concept Two – Revision D.....	92
Conclusion and recommendations.....	99
8.1 Conclusion	99
8.2 Recommendations.....	100
References	101
Appendix.....	107

List of tables

Table 1. Generic truck model, comparison of mass flow and drag coefficient for various deflector geometries.....	10
Table 2. Total force and fuel improvement for all the models	13
Table 3. Effect of deflector angle on drag coefficient.....	15
Table 4. GHG emissions from European tractor-trailers for baseline, fuel cell vehicle-intensive, and electric vehicle-intensive scenarios for 2050, with associated change in emissions	19
Table 5. Overview of the SAE driving automation levels	26
Table 6. Number of additional transport equations needed for each turbulence model.....	44
Table 7. Categorisation of drivetrain features in terms of overall drivetrain priority .	52
Table 8. Comparison of drivetrain configurations	53
Table 9. Eaton 4-speed EV transmission specifications.....	60
Table 10. Basic dimensions of the GCM.....	69
Table 11. CFD computational domain dimensions	70
Table 12. Comparison of CD values for all CFD simulated models	93

List of Figures

Figure 1. Horsepower required to overcome aerodynamic drag and rolling friction/accessories as a function of travel speed for a typical Class 8 tractor-trailer 2

Figure 2. Camille Jenatzy’s creation, the *La Jamais Contente* (David, 2013) 6

Figure 3. Mercedes-Benz EQS 7

Figure 4. Daimler Freightliner Cascadia truck 7

Figure 5. Global vehicle stock, distance travelled, and life-cycle road transport greenhouse gas emissions by vehicle type in 2015, 8

Figure 6. Projected global freight activity and life-cycle greenhouse gas emissions from 2015 to 2050 9

Figure 7. The wide and narrow side deflector models on a generic truck model 10

Figure 8. Showing various mud flap designs. From left to right: Full, half slats and half..... 11

Figure 9. Drag force coefficients of trucks with various mud flaps..... 11

Figure 10. Graphic depicting the distribution of aerodynamic drag for a heavy vehicle tractor-trailer truck..... 12

Figure 11. Various boat tail CAD models 12

Figure 12. Comparison of the effect of side panels on flow streamlines around vehicle: (a) Without side panel; (b) With side panel 13

Figure 13. Fuel increase as function of gap 14

Figure 14. Left: A truck without a deflector, Right: A truck with a deflector 14

Figure 15. Example of “crash nose” or “soft nose” 15

Figure 16: Lifecycle CO₂e emissions from Europe heavy-duty tractor-trailer fleet from 2015–2050, with base case, efficiency improvements, fuel cell-intensive, and electric-intensive scenarios. 16

Figure 17. The Volvo Vera concept autonomous BET..... 17

Figure 18. European emission pathways for three technology approaches to reducing CO₂ emissions..... 19

Figure 19. Global electric vehicle stock from 2010 to 2020 20

Figure 20. The savings per kilometre for vehicles with various energy sources 21

Figure 21. Evolution of the global electric car stock, 2010-16 22

Figure 22. Evolution of battery capacity for batteries used in automobiles from 1983 to 2022 23

Figure 23. Evolution of battery energy density and cost 24

Figure 24. A comparison of battery technologies..... 25

Figure 25. Expected battery developments 25

Figure 26. Camera vision in autonomous vehicles 28

Figure 27. Radar field of view in an autonomous vehicle	29
Figure 28. Ultrasonic field of view in an autonomous vehicle.....	29
Figure 29. General LiDAR field of view in an autonomous vehicle	30
Figure 30. Sensor fusion in an autonomous vehicle.....	31
Figure 31. The lift and drag acting on a body as a result of being immersed in an airflow.	32
Figure 32. The effects of skin friction drag and pressure drag for various geometries	33
Figure 33. Streamline diagram with the plan view above and side view below	34
Figure 34. Typical airflow around an un-aerodynamic truck (left) and an aerodynamically effective truck (right).....	35
Figure 35. Boundary layer: Velocity distribution in direction perpendicular to the... surface. The separation point is also represented (Genta & Morello, 2020:123).	36
Figure 36. Attached flow over (a) a streamlined car and (b) the locally separated flow behind a more realistic automobile shape	37
Figure 37. Reference frame often used to express aerodynamic forces	38
Figure 38. Streamlines over a vehicle	39
Figure 39. Effect of streamlining the underbody of a vehicle on the aerodynamic drag coefficient.....	40
Figure 40. The moving ground problem: (a) On the road there is a boundary layer on the vehicle underbody, and (b) In a wind tunnel with stationary floor, there are two boundary layers under the car, and the flow is different	41
Figure 41. Central motor + single ratio reduction transmission + differential	49
Figure 42. Central motor + multiple ratio transmission + differential	50
Figure 43. Two by-wheel or hub motors + single ratio transmission	50
Figure 44. Heavy-duty truck on a slope and applied forces.....	53
Figure 45. CAD model of a radial-flux electric motor	55
Figure 46. The basic dimensions of the DANA TM4 SUMO range of electric motors	56
Figure 47. The basic dimensions of the DANA TM4 CO150 inverter	56
Figure 48. A Proterra S Series battery pack	58
Figure 49. The placement of the battery packs in a conventional BET	59
Figure 50. Eaton 4-speed EV transmission	60
Figure 51. The Mercedes-Benz Future Truck.....	61
Figure 52. The Tesla Semi	62
Figure 53. The possible roll out of autonomous BETs in the USA.....	65
Figure 54. Class 8 truck width limit	67
Figure 55. Class 8 truck length limits	67

Figure 56. Generic Conventional Model (GCM).....	68
Figure 57. Basic dimensions of the GCM.....	68
Figure 58. CFD computational domain.	69
Figure 59. Generated polyhedral mesh.	71
Figure 60. Mesh refinement box around the GCM.	71
Figure 61. Inflation layer on the GCM.	73
Figure 62. Drag coefficient graph for the GCM.	74
Figure 63. Wall Y^+ value for the GCM.....	75
Figure 64. Pressure distribution over the GCM.	76
Figure 65. Flow velocity magnitude (top), flow vorticity magnitude (middle), and flow pressure coefficient as seen from the top view of the GCM (Bottom).	77
Figure 66. Autonomous BET Concept One.	80
Figure 67. Concept one schematic shown in isometric view (top), plan view (bottom left), and side view (bottom right).	80
Figure 68. Autonomous BET Concept Two.	81
Figure 69. The flow pressure coefficient (top), and flow velocity magnitude (bottom) over Concept One.	83
Figure 70. Flow pressure coefficient over Concept Two (left), and a magnified view of the frontal area (right).	83
Figure 71. Flow velocity magnitude (top), and flow vorticity magnitude (bottom) over Concept Two.	84
Figure 72. Tractor side (top) and floor (bottom) radius changes for Concept Two - Revision A, highlighted in orange.	85
Figure 73. Comparison of pressure coefficient between Concept Two baseline (left), and Concept Two - Revision A (right).	86
Figure 74. Comparison of vorticity magnitude between Concept Two baseline (left), and Concept Two - Revision A (right).	86
Figure 75. Concept Two – Revision B.	87
Figure 76. Side view comparison of the turbulent intensity of the flow between Concept Two – Revision A (top), and Concept Two – Revision B (bottom).	88
Figure 77. Plan view comparison of the turbulent intensity of the flow between Concept Two – Revision A (top), and Concept Two – Revision B (bottom).	88
Figure 78. Side view comparison of the vorticity magnitude of the flow between Concept Two – Revision A (top), and Concept Two – Revision B (bottom).	89
Figure 79. Concept Two – Revision B – full view (top), modified tractor rear (bottom – highlighted in orange).	90
Figure 80. Side view comparison of the pressure coefficient of the flow between Concept Two – Revision B (top), and Concept Two – Revision C (bottom).	91
Figure 81. Plan view comparison of the pressure coefficient of the flow between Concept Two – Revision B (top), and Concept Two – Revision C (bottom).	91

Figure 82. Plan view comparison of the turbulent intensity of the flow between Concept Two – Revision B (top), and Concept Two – Revision C (bottom).....	92
Figure 83. Concept Two – Revision D, removed geometry for the tapered roof feature is highlighted in orange.....	92
Figure 84. Pressure coefficient over the GCM body.	96
Figure 85. Pressure coefficient over the Concept Two – Revision D body.....	96
Figure 86. Side view (top) and plan view (bottom) of the airflow turbulent intensity over Concept Two – Revision D.....	97
Figure 87. Side view (top) and plan view (bottom) of the airflow turbulent intensity over the GCM.	97
Figure 88. Side view (top) and plan view (bottom) of the airflow pressure coefficient over Concept Two – Revision D.....	98
Figure 89. Side view (top) and plan view (bottom) of the airflow pressure coefficient over the GCM.	98

Abbreviations

AV	Autonomous vehicle
BET	Battery Electric Truck
BEV	Battery Electric Vehicle
CAD	Computer-aided Design
CFD	Computational Fluid Dynamics
CPUT	Cape Peninsula University of Technology
DCM	Direct Current Motor
DOE	Department Of Energy
EMI	Electromagnetic Interface
GCM	Generic Conventional Model
GHG	Greenhouse Gas
HVAC	Heating, Ventilation, and Air Conditioning
ICE	Internal Combustion Engine
IM	Induction Motor
LHF	Low Hanging Fruit
LiDAR	Light Detection And Ranging
PC	Personal Computer
PHEV	Petrol Hybrid Electric Vehicle
PMSM	Permanent Magnet Synchronous Motor
RADAR	Radio Detection And Ranging
RANS	Reynolds-Averaged Navier-Stokes
RPM	Revolutions Per Minute
SAE	Society of Automotive Engineers
SRM	Switched Reluctance Motor
SVT	Single Stage Variable Transmission
WtW	Wheel To Wheel

List of symbols

ρ	[kg/m ³] Density
\vec{f}	[N] Vector body force
δ_{99}	[m] Boundary layer thickness at 99% of the free stream velocity
Δy_1	[m] Height of the first prism cell in the inflation layer
μ	[N.s/m ²] Dynamic viscosity
Γ	[m ² /s] Eddy diffusivity
ε	[m ² /s ³] Turbulent kinetic energy dissipation rate
σ	[-] Prandtl/Schmidt number
ν	[m ² /s] Kinematic viscosity
τ	[N/m ²] Wall shear stress
A, A_f	[m ²] Frontal area
C_D	[-] Coefficient of drag
C_f	[-] Coefficient of skin friction
C_{rr}	[-] Coefficient of rolling resistance
D_h	[m] Domain height
D_l	[m] Domain length
D_w	[m] Domain width
F_D	[N] Drag force
F_x	[N] Longitudinal aerodynamic force
F_y	[N] Lateral aerodynamic force
F_z	[N] Normal aerodynamic force
g	[m/s ²] gravity
H_m	[m] Height of tractor-trailer
k	[m ² /s ²] Turbulent kinetic energy
L_b	[m] Length of the domain behind the trailer rear face
L_f	[m] Length of the domain in front of the tractor front face

L_m	[m] Length of the tractor-trailer
m	[kg] mass
M_x	[N.m] Rolling moment
M_y	[N.m] Yawing moment
M_z	[N.m] Pitching moment
r	[m] Radius of truck wheel
Re	[-] Reynolds number
β	[deg] Road gradient
t, T	[s] Time
u	[m/s] Velocity
v	[m/s] Velocity
V_∞	[m/s] Free stream velocity
w	[m/s] Velocity
W_m	[m] Width of the tractor-trailer
Y^+	[-] Wall distance

Chapter 1

Introduction

1.1 Background

Since the advent of the car by Carl Benz in 1886, people have sought to improve upon its design, to go faster, and more safely and efficiently. As time passed and cars became faster, the importance of the aerodynamics of the car became a significant performance factor. This is especially true for motorsport. Specifically, the aerodynamic drag of a vehicle is an important performance metric. In heavy vehicles, aerodynamic performance is geared towards fuel saving, keeping fleet costs down.

In the land freight industry, heavy trucks are a major contributor to greenhouse gas emissions. For trucks travelling at average highway speeds, aerodynamic drag represents the majority of the opposing force that the truck's diesel engine must overcome. Figure 1 shows the horsepower required to overcome aerodynamic drag and rolling friction/accessories at different levels of travel speed for a typical Class 8 tractor-trailer (McCallen et al., 2004:2). This inefficiency contributes greatly towards increasing the emission of greenhouse gases, as well as increasing fuel costs for the trucking company.

A significant amount of research has been done on investigating drag reduction devices that can be fitted to existing internal combustion engine (ICE) heavy-duty trucks (Cooper, 2003; Den Boer et al., 2013; Hariram et al., 2019; Hjelm & Bergqvist, 2009; Hyams et al., 2011; Humphreys & Bevly, 2016; Khosravi et al., 2015; McCallen et al., 2004; Miralbes & Castejon, 2012; Mohamed-Kassim & Filippone, 2010; Selenbas et al., 2010; Skrucany et al., 2016).

Work has also been done on ground-up design improvements for the purpose of aerodynamic drag reduction. Legislation that has been implemented on the grounds of pedestrian safety has also had a knock-on effect of allowing for more streamlined truck designs.

While these improvements have been commercialised for decades and ancillary options are available to fleet owners, the current trajectory of greenhouse gas (GHG) emissions for the truck-dominated land freight sector does not meet the long term goals of successfully tackling climate change.

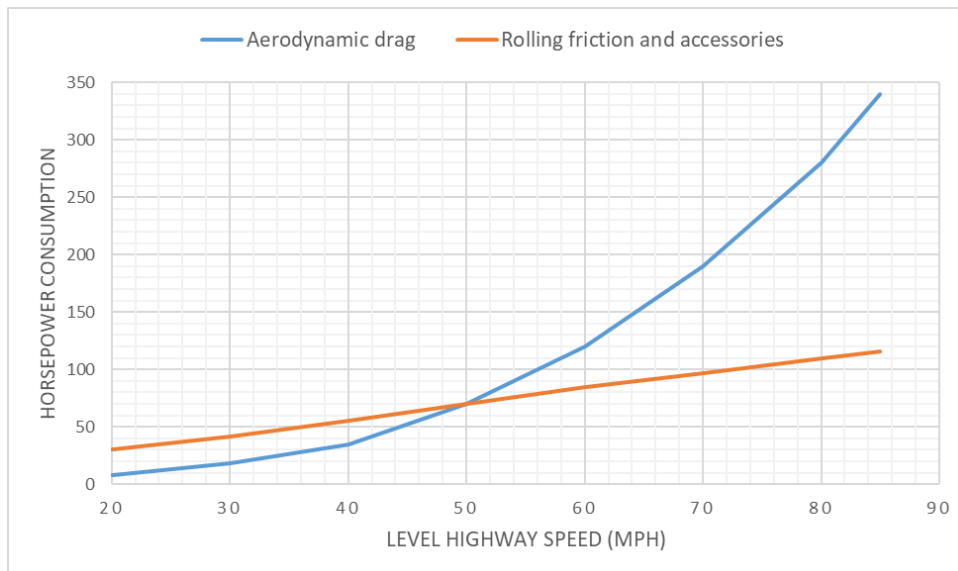


Figure 1. Horsepower required to overcome aerodynamic drag and rolling friction/accessories as a function of travel speed for a typical Class 8 tractor-trailer. Redrawn from (McCallen et al., 2004:2).

In moving towards the future goals of a zero-emission truck, battery electric drivetrains represent a favourable future technology path. This push towards an electric future is running parallel with the rapid advancement in autonomous driving technology. This provides the scope for investigating concepts of a driverless battery electric truck (BET) with the ultimate goal of optimising the truck-trailer exterior geometry for the purpose of aerodynamic drag reduction.

Aside from the potential geometrical and topological layout improvements of an autonomous BET, an autonomous driving mode is potentially smoother, more consistent, more efficient and safer than a human driver. The long term economics of cost of ownership for autonomous BETs is also lower than for conventional diesel ICE trucks (Sanguesa et al., 2021:373).

1.2 Problem statement

Aerodynamic drag accounts for 65% of the total energy demand in heavy trucks (McCallen et al., 2004:2). This manifests as low fuel efficiency and results in a much greater contribution to global greenhouse gas emissions. The current design of heavy duty tractor-trailers is heavily constrained by the need of having a large ICE, its associated cooling and exhaust packages, a driver cabin with heating, ventilation and air conditioning (HVAC), and driver safety systems. Great strides have been made in improving the aerodynamic drag of heavy-duty tractor-trailers over the decades. However, the more recent improvements have been marginal and the long term prospects of achieving GHG emissions goals for the future using conventional diesel ICE trucks is very difficult.

1.3 Research rationale

The global automobile market is moving toward an electric vehicle (EV) future, and it is incorporating autonomous driving technology to improve efficiency as well as safety. The trucking industry will need to adopt a similar technology in order to meet the climate change goals of the future. With the incorporation of autonomous battery electric trucks (BET), the exterior geometry of such a truck needs to be optimised for drag reduction.

Any significant improvements in drag reduction serve to move the industry closer to the GHG emission goals of the future as well as to reduce fuel costs for truck owners.

Research that is aligned with this goal is beneficial for attaining sustainability goals for the planet in terms of GHG emissions. Computational fluid dynamics (CFD) analysis is also a cost- and time-effective tool for baselining concepts and design trends without having to spend on large prototype and testing budgets.

1.4 Research questions

The driving demands of a heavy-duty tractor-trailer are very high, in transportation of heavy loads across vast distances and road grades. Research questions that this work aims to answer are listed below:

- Whether there any currently available batteries, electric motors, transmissions and autonomous systems which can meet the demands of a long-haul heavy-duty truck?
- Which are the best CFD solver parameters to use for such a study and for the available computing resources.?
- What coefficient of aerodynamic drag can be achieved for an autonomous BET in comparison to a conventional truck simulated under the same conditions?

1.5 Research aim

This research aims to ascertain what basic exterior geometry of an autonomous BET provides the greatest reduction in the overall aerodynamic drag of the truck-trailer, without hindering the practical functions of a long-haul heavy truck-trailer.

1.6 Research significance

In a world where the demand for products and services grow, the trucking industry is expected to grow as well. With heavy trucks being a major source of GHG emissions, increasing fuel usage results in the depletion of natural resources of the planet. Any improvement made to the overall energy efficiency of the truck-trailer, will contribute greatly to reducing the usage of natural resources. It will also contribute to the reduction of global GHG emissions.

The trucking industry also stands to benefit from a reduction in aerodynamic drag, reducing the energy consumption of its fleet, thereby reducing operating costs.

Automated trucks are seen as the first type of vehicle to be introduced on public roads as a fully autonomous vehicle (Kouchak & Gaffar, 2017). This research will contribute towards reaching the year 2050 goal of having zero-emission trucks.

1.7 Delineation of the research

The simulation needs to be optimized for the available computing power and storage space for each iteration of the simulation.

Only airflow over the exterior surfaces of the vehicle will be simulated. No airflow through the interior of the vehicle (for the cooling of electric motors and batteries) will be considered due to the increase in computing power and simulation time that this will demand.

This study will only be concerned with the average highway driving profile of a long-haul heavy truck-trailer. No urban stop-start driving profiles will be considered. As aerodynamic drag increases with vehicle speeds, only highway speeds in excess of 90km/h will be considered, where the aerodynamic drag is the dominant opposing force to the vehicle.

Since the simulation will be considering the highway driving profile of a truck-trailer, only incompressible flow will be considered in the CFD analysis.

The downstream effect of airflow coming off the vehicle, and its interaction with other road vehicles will not be considered.

Yawed flow will not be considered due to the increase in simulation run time this would take, as well as the increased computing power requirement for such a simulation.

The effects of a dynamic suspension which results in the variation of the ride height of the truck-trailer will not be considered due to the increase in complexity of the CFD analysis and resulting increase in computing power and simulation time needed.

1.8 Research structure

The basic structure of this research is listed below, with descriptions of each chapter.

Chapter 1 – Introduction: This chapter gives an overview of the background of the industry and the impact of aerodynamic drag on the entire land freight industry. It also introduces the reader to the significance of an autonomous BET in terms of moving the sector closer to the long term goals of addressing climate change. The aim of this research is described, as well as questions that this research aims to answer. Lastly the research is delineated.

Chapter 2 – Literature review: The literature review chapter provides an overview to the theoretical background of the topic. It also provides the reader with an understanding of the physics and engineering fundamentals which underpin the

research. The literature review focuses on the main aspects which define the research area, namely: autonomous vehicles and systems, truck aerodynamics, and battery technology. Other aspects discussed are: GHG emissions in the land freight sector, decarbonisation of the trucking sector, future battery technologies, and the financial viability of large scale adoption of EVs into the mainstream vehicle market.

Chapter 3 – Technical background: This chapter aims to provide insight on aspects of vehicle aerodynamics, and in particular bluff body aerodynamics, and the technical aspects of CFD simulation and solver parameter selection.

Chapter 4 – Experimental methods and design: This chapter gives a holistic view on the requirements of an autonomous BET to perform its function. The chapter examines the optimal drivetrain topology for such a vehicle. An overview is provided of the individual drivetrain component requirements and their selection from commercial offerings. The chapter also provides a future technology roadmap of each drivetrain component, an overview of the financial and political barriers that currently exist for mainstream EV adoption, and lastly a development path for autonomous BETs with rough timelines for the next three decades.

Chapter 5 – Numerical modelling: This chapter outlines the CFD setup, the validation of the simulation against empirical data, as well as defining the metrics used to measure simulation accuracy.

Chapter 6 – Concept discussion: This chapter introduces the initial autonomous BET CAD concepts, and considers the topology of the drivetrain system. Each design iteration of the concept is informed by CFD simulation of the previous concept, with changes and results discussed in detail. Aspects of the flow such as the coefficient of pressure, coefficient of drag, vorticity, and wake are also discussed.

Chapter 7 – Results and discussion: Simulation results of the various concepts are compared and discussed.

Chapter 8 – Conclusion and recommendations: The concluding statements given in this chapter relate to the primary aims and objectives of the research set out in Chapter 1. Recommendations are provided for future research avenues which could contribute to the body of work.

Chapter 2

Literature review

2.1 Aerodynamic drag

Aerodynamic drag is defined as the sum of pressure drag and skin friction drag on a body (Anderson, 2010:1040).

The first use of aerodynamically streamlined vehicles was by Belgian racing car driver Camille Jenatzy. He created the vehicle that was the first road car to go beyond 100km/h and it was also electrically powered (David, 2013). Figure 2 below shows Camille's design.

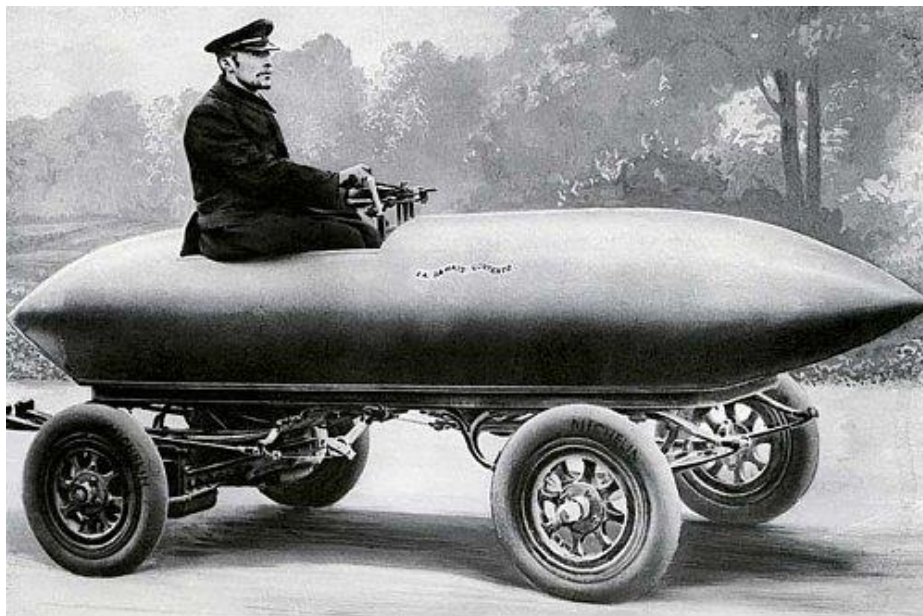


Figure 2. Camille Jenatzy's creation, the *La Jamais Contente* (David, 2013).

Fast forward ninety nine years to 2021, and the production car with the lowest aerodynamic drag coefficient (0.2) is the Mercedes-Benz EQS (Daimler, 2021). The most aerodynamic truck is the Daimler Freightliner Cascadia (Daimler, 2007).

Both the Mercedes-Benz EQS and the Daimler Freightliner Cascadia can be seen in Figure 3 and Figure 4 respectively.



Figure 3. Mercedes-Benz EQS (Weiss, 2021).



Figure 4. Daimler Freightliner Cascadia truck (Cascadia, 2021).

2.2 The freight transportation industry

We live in a very interconnected world, where billions of tons of goods are transported across countries and continents. The global transport industry is a multi-trillion-dollar business, which is expected to continue growing in the coming decades. In the Americas, Europe and Nordic countries the transport industry is so large, that it is the leading source of greenhouse gases (GHG), and therefore the largest contributor to global climate change for these regions (Ambel et al., 2017).

Road freight in Europe and Nordic countries account for 90% of the total GHG emissions, and heavy-duty vehicles, like large trucks account for 25% of this figure. As stated previously, the usage of heavy-duty trucks within the transport industry is expected to increase in the coming decades (Ambel et al., 2017).

Figure 5 below shows the global vehicle stock, distance travelled, and life-cycle GHG emissions by vehicle type in 2015.

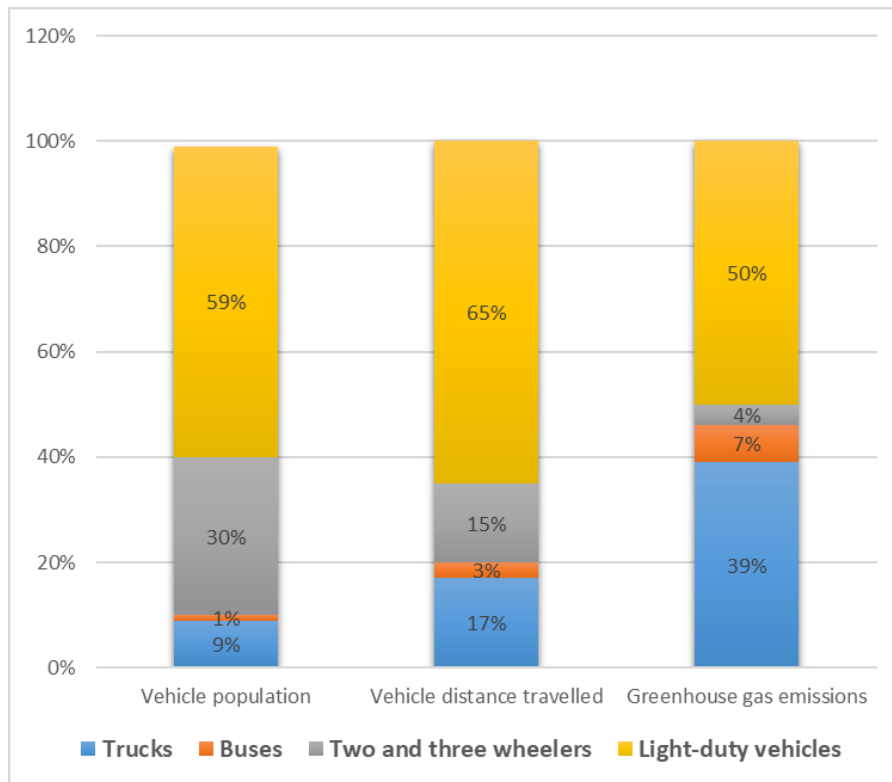


Figure 5. Global vehicle stock, distance travelled, and life-cycle road transport greenhouse gas emissions by vehicle type in 2015, Redrawn from (Moultak et al., 2017:1).

From Figure 5, it is evident that freight trucks represent 9% of the total vehicle stock, and 17% of the distance travelled, yet they account for 39% of GHG emissions (Moultak et al., 2017).

As seen in Figure 6, this disproportionality is only set to grow larger in the coming decades as the global transport industry grows larger. From this, it is evident that heavy truck activity is set to increase in activity at a faster rate than that of other vehicles in the transportation industry (Moultak et al., 2017). What is more, should business continue as is, heavy trucks are projected to represent over 60% of the total freight activity, and account for over 75% of the life-cycle CO₂ emissions in the transportation industry (Moultak et al., 2017). From the grey line, which represents total heavy-duty truck carbon dioxide equivalent (CO₂e) emissions, it is also clear that emissions from heavy trucks are set to at least double by the year 2050 compared to levels measured in 2015.

Aside from CO₂ emissions, the heavy-duty truck industry also contributes to local air pollution, particularly emissions of harmful nitrogen oxides and particulates. In areas with high freight activity, like depots, this local air pollution negatively affects the health and livelihood of the community living nearby. In most cases, these communities are made up of low-income households, for whom effective healthcare may be financially out of reach (Moultak et al., 2017).

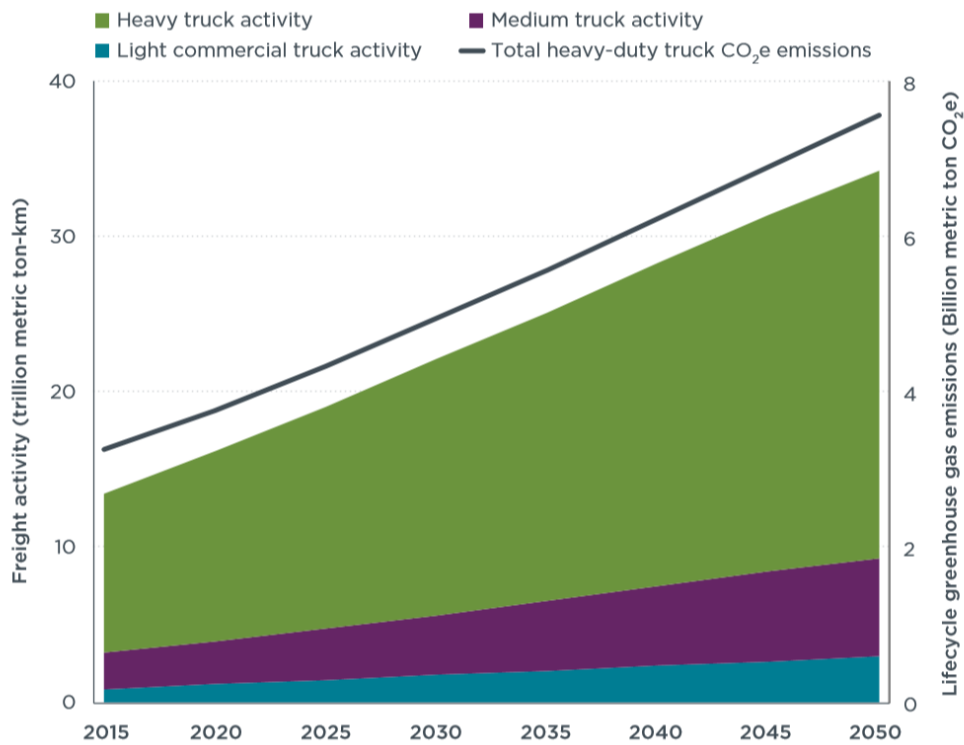


Figure 6. Projected global freight activity and life-cycle greenhouse gas emissions from 2015 to 2050 (Moultak et al., 2017:2).

2.3 Aerodynamic drag as a contributor to GHG emissions

Throughout the last few decades, progress has been made in reducing aerodynamic drag from the initial design phase. Research has also been completed to assess various aerodynamic drag reduction technologies, as well on designing add-on structures that can be added to existing truck designs.

2.3.1 Truck ancillaries

Truck ancillaries such as wind deflectors, wind visors, and side mirrors can all be designed to contribute towards reducing the overall drag of the truck. CFD is a powerful design tool which can quickly evaluate the aerodynamic benefit of making design changes to these truck ancillaries. Selenbas et al., (2010) have shown how CFD can be used to optimise truck ancillaries and how that modification can reduce the overall aerodynamic drag of the truck.

A total of thirteen different designs for wind deflectors at the front of the truck were investigated with respect to their role in reducing the overall aerodynamic drag of the truck, particularly the drag effects emanating from the truck's rear wheels. Figure 7 below shows the wide and narrow side deflector models on a generic truck model (Selenbas et al., 2010).

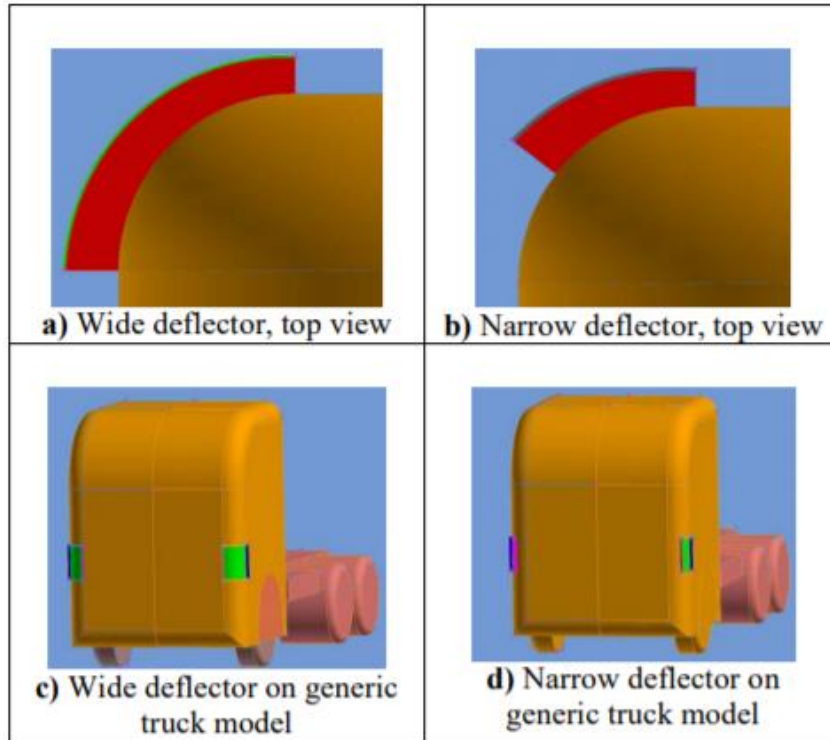


Figure 7. The wide and narrow side deflector models on a generic truck model (Selenbas et al., 2010:6).

Table 1 below shows thirteen generic truck models, comparison of mass flow, and drag coefficient for various deflector geometries (Selenbas et al., 2010:7).

Table 1. Generic truck model, comparison of mass flow and drag coefficient for various deflector geometries, redrawn from (Selenbas et al., 2010:7).

Case	Section Ratio A_{outlet} / A_{inlet}	Mass Flow Rate (kg/s)	Drag Coefficient C_D
1	-	-	0.430
2	0.70	0.726	0.433
3	0.70	0.715	0.431
4	1.00	1.034	0.430
5	1.00	0.954	0.431
6	0.44	0.458	0.450
7	0.44	0.642	0.420
8	0.70	0.702	0.444
9	0.70	0.640	0.430
10	0.66	1.045	0.437
11	0.66	1.002	0.426
12	0.47	0.717	0.446
13	0.47	0.722	0.429

2.3.2 Mud flaps

The mud flaps on a truck are exposed to the airflow passing through the underside of the trailer. As a result, they influence the overall aerodynamic drag of the truck-trailer.

Simulations have been done by Hyams et al. (2011) to investigate the effect of various mud flap designs on the drag coefficient of trucks. Figure 8 below shows three mud flap designs. From left to right: Full, half slats and half (Hyams et al., 2011:38-39).

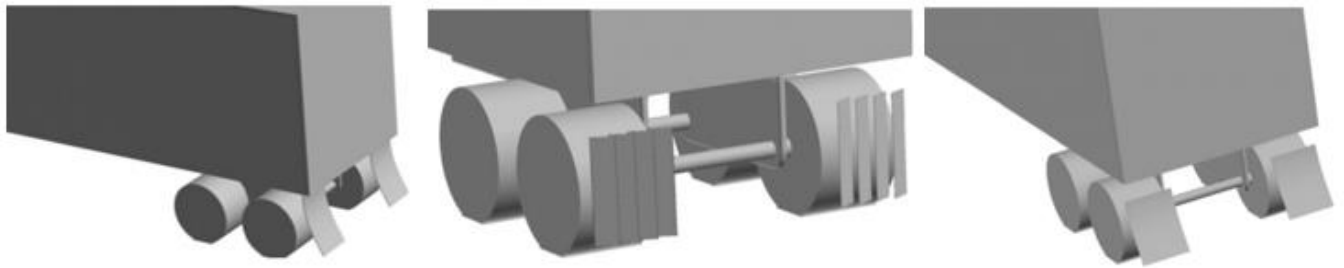


Figure 8. Showing various mud flap designs. From left to right: Full, half slats and half (Hyams et al., 2011:38-39).

Results from Hyams et al. (2011) show that the full mud flap design produces the highest drag force coefficient of 0.377 and adds 8.6% to the total drag on the truck. See Figure 9 below.

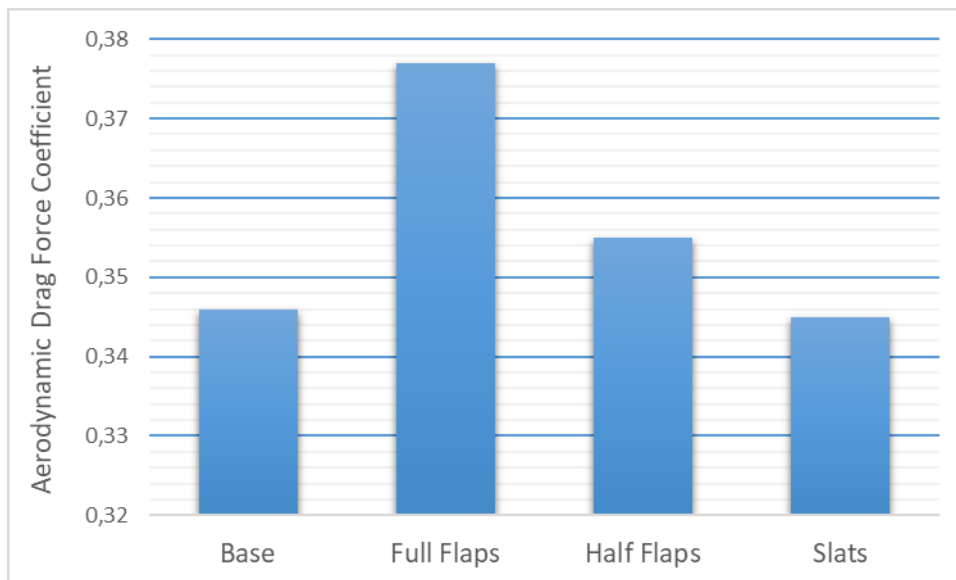


Figure 9. Drag force coefficients of trucks with various mud flaps, redrawn from (Hyams et al., 2011:39).

2.3.3 Boat tails

The rear end of the trailer in heavy trucks usually ends abruptly in a squared-off shape, as shown in Figure 10 below. This shape causes airflow separation and turbulence in the area just behind the rear of the trailer.

Miralbes & Castejon (2012) have done work on investigating the effect of adding a fairing to the rear of the trailer in truck-trailer vehicles. This fairing is known in the industry as a boat tail. Boat tails serve to improve drag reduction at the rear of trailer, an area responsible for roughly 25% of the total aerodynamic drag on the truck. This can be seen in the area behind the truck in Figure 10 below.

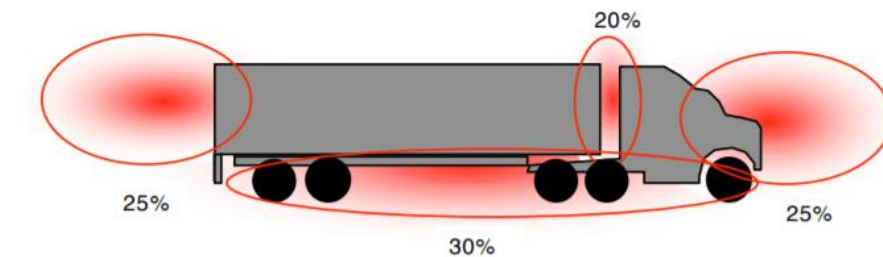


Figure 10. Graphic depicting the distribution of aerodynamic drag for a heavy vehicle tractor-trailer truck (Wood, 2006:3).

Figure 11 below shows the five different boat tail concepts that were investigated, with the resultant percentage of drag reduction and the corresponding percentage increase in fuel economy shown in Table 2.

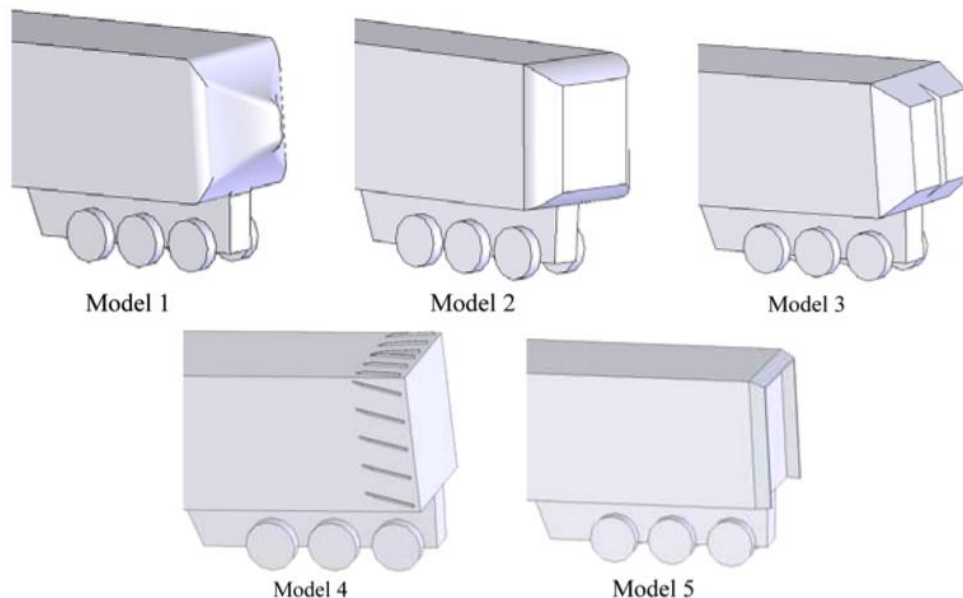


Figure 11. Various boat tail CAD models (Miralbes & Castejon, 2012:118).

Table 2. Total force and fuel improvement for all the models, redrawn from (Miralbes & Castejon, 2012:123).

	Pressure force (N)	Viscous force (N)	Total force (N)	% Drag reduction	% Fuel economy
Original model	2364.22	158.78	2523.00	-	-
Model 1	2036.76	160.06	2196.82	12.93	5.65
Model 2	2112.00	161.38	2273.38	9.89	3.96
Model 3	2008.22	158.40	2166.62	14.13	5.17
Model 4	2345.64	159.14	2504.78	0.72	0.29
Model 5	2106.70	161.98	2268.68	10.08	4.03

2.3.4 Trailer side panels

The wheels and tyres on a truck cause airflow disruption over the sides of the truck. This resultant turbulence increases the aerodynamic drag of the truck. In some modern trucks, the use of trailer side panels has been shown to reduce the overall drag of the truck. Khosravi et al. (2015) have modelled the effects of having a trailer side panel running along the rear of the trailer. They found that the addition of a trailer cover reduced the aerodynamic drag by 3.9%. Figure 12 below shows the comparison of the effect of side panels on flow streamlines around vehicle: (a) Without side panel; (b) With side panel (Khosravi et al., 2015:4649).

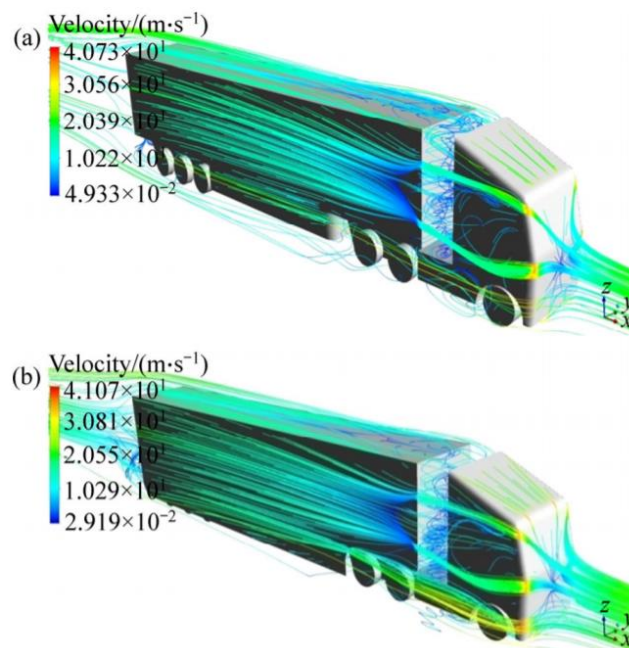


Figure 12. Comparison of the effect of side panels on flow streamlines around vehicle: (a) Without side panel; (b) With side panel (Khosravi et al., 2015:4649).

2.3.5 Truck-trailer gap

The gap between the rear of the truck cab and the front of the trailer has significant influence on the aerodynamic drag of the truck-trailer combination. Turbulent airflow develops in the gap between the rear of the cab and the front of the trailer which results in increasing the aerodynamic drag. Work has been done by Hjelm & Bergqvist (2009) in investigating the effect of this gap on fuel usage. The relationship between this gap and the percentage of fuel increase of the truck was tested on a Volvo VN 1/2-scale model truck and trailer during tests in the Volvo wind tunnel (PVT) in Gothenburg. See Figure 13 below.

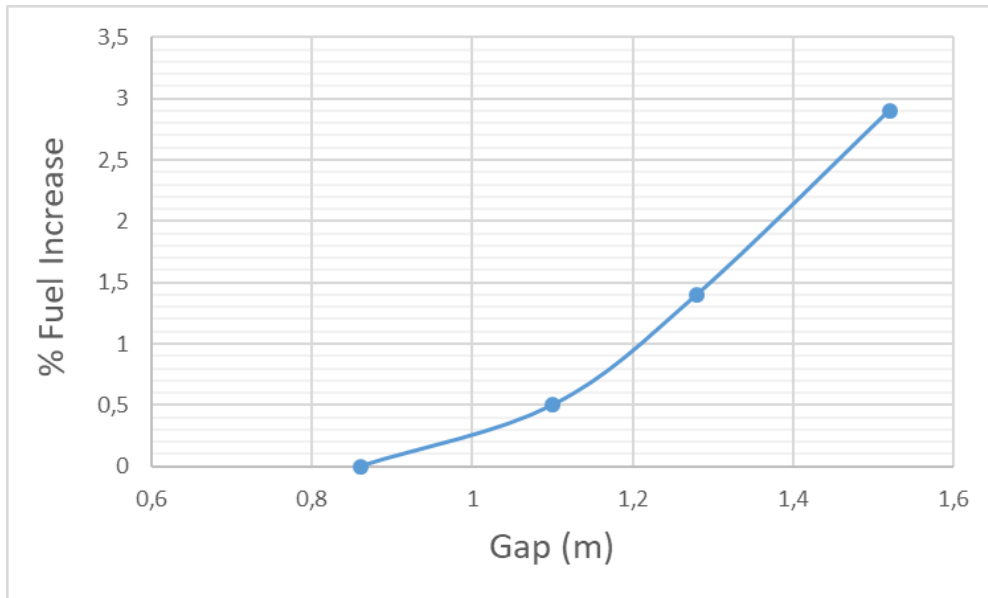


Figure 13. Fuel increase as function of gap, redrawn from (Hjelm & Bergqvist, 2009:471).

2.3.6 Deflector panel

Deflector panels have long been used on trucks and have shown to be useful in reducing aerodynamic drag. Figure 14 below shows the smoke flow patterns over a truck with and without a deflector added

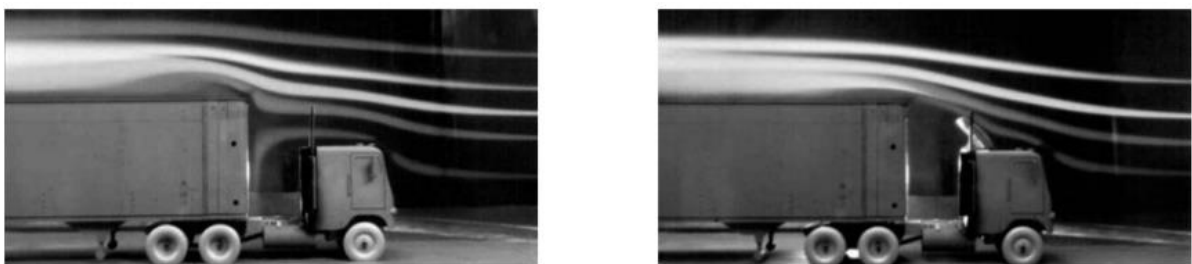


Figure 14. Left: A truck without a deflector, Right: A truck with a deflector (Cooper, 2003).

Deflector panels are generally flat in its geometry. The angle of the deflector panel relative to the horizontal, influences its effect on aerodynamic drag. Table 3 below

shows the changes in the aerodynamic drag coefficient (C_D) for various angles of the deflector panel.

Table 3. Effect of deflector angle on drag coefficient, redrawn from Khosravi et al. (2015:4647).

(H_1-H_2) [mm]	Angle [Degrees] $^\circ$	Force [N]	C_D
-758	5	1796	0.8130
-562.5	10	1673	0.7574
-361	15	1544	0.6990
-150	20	1402	0.6347
0	23	1450	0.6564
74.5	25	1490	0.6745
318.5	30	1623	0.7347
588.5	35	1760	0.7967

2.3.7 Future design approaches

Work has also been done that looks toward the future of truck aerodynamics, with respect to trucks that use a conventional ICE as a means of a power source for the vehicle drive. Legislation is being discussed in Europe to introduce a 300mm extension to the front of trucks to improve pedestrian safety. This additional area could provide scope for improving the truck aerodynamic efficiency (Hjelm & Bergqvist, 2009). An example of such an extension known as a “crash nose” or “soft nose” can be seen in Figure 15, highlighted by the green dashed rectangle.



Figure 15. Example of “crash nose” or “soft nose”, redrawn from Davis (2020).

2.4 Future design requirements

In the modern world, factors like GHG emissions, sustainability of the diminishing natural resources of the planet, and increasing fuel costs have made a huge impact on the passenger car industry. With the low fuel efficiency and high GHG emissions,

truck design for the future needs to be more energy efficient and less polluting (Miralbes & Castejon, 2012).

Goals set out by governments with a focus on future GHG emissions, require a reduction of emissions by 80% to 95% by 2050 in comparison with 1990 GHG emission percentages. A more immediate goal is a reduction in emission levels by 40% by 2030, compared to the emission levels in 1990 (Graichen, 2016:6).

To meet the year 2050 goal, heavy trucks used in the land freight industry will need to become zero-emission vehicles by 2050 (Earl et al., 2018; Moultaq et al., 2017).

The carbon dioxide equivalent (CO_{2e}) emissions for the various truck propulsion technologies are illustrated in Figure 16, as predicted by (Moultaq et al., 2017:28).

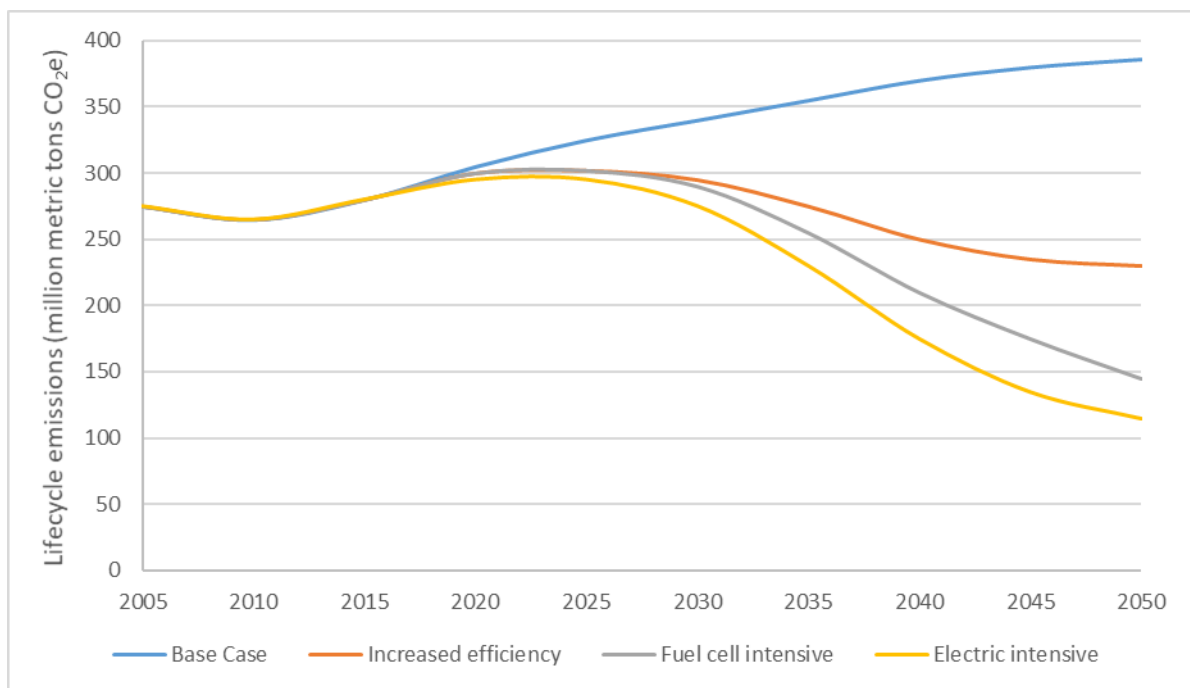


Figure 16: Lifecycle CO_{2e} emissions from Europe heavy-duty tractor-trailer fleet from 2015–2050, with base case, efficiency improvements, fuel cell-intensive, and electric-intensive scenarios. Redrawn from (Moultaq et al., 2017:28).

Studies have found that in order to meet the goals of a zero-emission truck, direct electric drivetrains are the most energy efficient solution (Earl et al., 2018; Moultaq et al., 2017).

In recent years, the development of Battery Electric Vehicles (BEV) and autonomous vehicles (AV) has seen rapid growth in the passenger car market. The benefits in safety, fuel efficiency, and global GHG emissions that autonomous BEVs exhibit, have seen this technology being adopted by the transportation industry at a rapid rate (Kouchak & Gaffar, 2017).

Vehicles in some countries operate in a full-autonomous mode, which require no driver inputs during dynamic driving. Due to the special features in its operation –

being used on set routes and at set times – designing autonomous trucks is a simpler task compared to designing an autonomous passenger vehicle (Kouchak & Gaffar, 2017).

Most recently, Volvo has shown a concept autonomous Battery Electric Truck (BET) with their Vera concept truck (Volvo, 2018).

The Vera truck pictured in Figure 17 below shows what scope exists for research of aerodynamic optimisation on an autonomous BET, namely:

- Not having a cab for a driver allows for minimising the total area exposed to the air, which should translate to a reduced aerodynamic drag.
- Not having an exhaust system or driveline underneath the vehicle provides scope for smoothing out the floor of the vehicle as much as possible.
- Evaluation of existing trailer aerodynamic drag reduction devices in combination with an autonomous BET.
- Evaluation of new devices for trailer drag reduction in combination with an autonomous BET.



Figure 17. The Volvo Vera concept autonomous BET (Cargo-Partner, n.d.).

2.5 Influence of previous work on this research

The previous work outlined in section 2.3 will serve as a reference point for this research. Of particular interest is the work done with regards to trailer drag reduction.

As airflow for the trailer section of the truck is greatly influenced by the front section of the truck, not all of the solutions identified in the previous sections can be assumed to work as is for an autonomous BET.

Batteries cannot be run until they are flat as this will damage the cells. The United States Department of Energy (DOE) recommends using a battery utilisation rate of

85% to 90% (Earl et al., 2018:8). For this research, a battery utilisation rate of 90% will be assumed for the battery packs.

When a truck is moving along the road, the proximity of the road to the underbody of the truck has an aerodynamic effect. Krajnović & Davidson (2005) have investigated the aerodynamic effects of this moving ground plane on a vehicle body. With the possibility of BETs having a smooth underbody due to the fact that they do not require an exhaust system, transmission, and driveline, the effects of a moving ground plane will be investigated. Their findings for the time-averaged pressure drag coefficient for a stationary ground plane is 0.292 and 0.269 for a moving ground plane (Krajnović & Davidson, 2005:684).

McCallen et al. (2004:2) states that the average C_D for a large truck-trailer is 0.6. This figure will serve as a reference for what C_D is found to be possible for an autonomous BET from this research.

With CFD simulations, correct and proper meshing techniques, as well as setting up the correct initial conditions for the simulation are of prime importance. Humphreys & Bevely (2016) demonstrated various CFD meshing techniques as well as a CFD environment setup to good effect. The sectioning of the mesh density for a large truck is particularly useful for this research as it allows the computing power to be used more efficiently.

2.6 Decarbonisation of the transport industry

For light and medium duty trucks, battery electric drivetrains are widely accepted as the most efficient and cost-effective method for decarbonisation of the sector for these types of vehicles (Ambel et al., 2017).

In Figure 18 below, the different emission pathways for various technology approaches are shown for the year range of 2000 to 2050, for the European and Nordic regions. The vertical axis represents the CO₂ emission in millions of tons (Mt). The low hanging fruit (LHF) approach is described as an approach that focuses on improving fuel efficiency of diesel engines in trucks and moving more freight onto railways (Ambel et al., 2017).

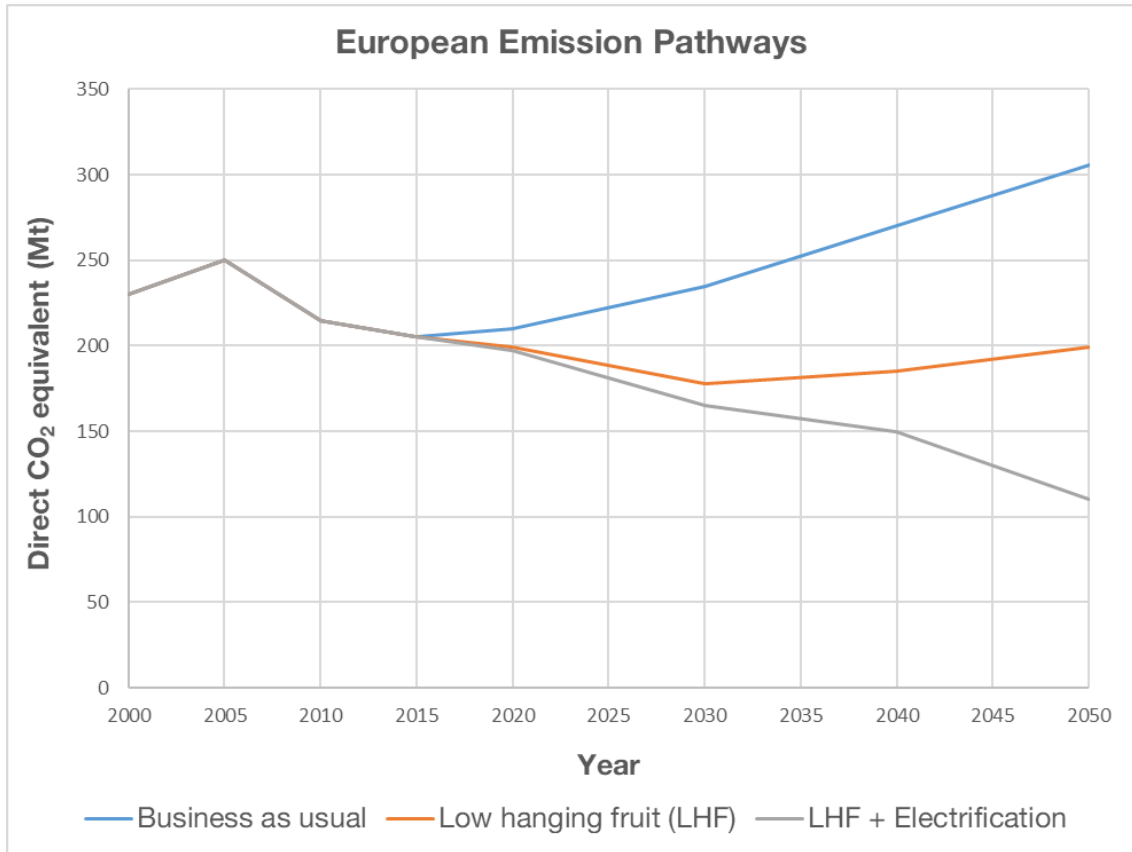


Figure 18. European emission pathways for three technology approaches to reducing CO₂ emissions, redrawn from (Ambel et al., 2017:3).

Table 4 below shows the GHG Emissions from European heavy-duty trucks as the baseline, heavy duty trucks that have been optimised using the LHF approach, fuel cell technology approach, and electric drivetrain technology approach for the period 2015 to 2050.

Table 4. GHG emissions from European tractor-trailers for baseline, fuel cell vehicle-intensive, and electric vehicle-intensive scenarios for 2050, with associated change in emissions. Redrawn from (Moultak et al., 2017:29).

Scenario	Emissions by year (million-ton CO ₂ e)			Change in emissions	
	2005	2015	2050	2015 to 2050	From 2050 base case
Base case	275	280	386		
Increased efficiency	275	280	230	-18%	-40%
Fuel cell intensive	275	280	145	-48%	-63%
Electric intensive	275	280	115	-59%	-70%

It is clear from Table 4 that an electric intensive technology approach to heavy duty trucks represents the biggest reduction in GHG emissions for the specified timeframe (Moultak et al., 2017:29).

It is important to note that these figures represent a drivetrain and powertrain change only. In other words, the trucks used in the study are not driverless trucks. It is reasonable to expect that the reduction in GHG emissions will be improved further in driverless BET where the mass saving and aerodynamic gains are considered.

By the year 2030, BET technology is predicted to have the capability to achieve large gains in reducing global GHG emissions in a cost-effective way. The key to achieving the cost effectiveness of adopting heavy duty BETs are the costs of the battery packs used in these vehicles.

A key figure with regards to this is the cost of battery packs dropping below \$150 per kilowatt hour (Moultak et al., 2017:32).

To meet the emission targets for the year 2050, the transportation sector needs to move towards an electric drive fleet. This transition is strongly underway in the passenger vehicle market, which in turn drives improvements in battery technology as well as infrastructure development.

2.7 The adoption of BEVs in the global vehicle market

Light duty trucks and vans are also shifting towards and electric drivetrain future, leveraging of the technology advancements gained in the electric passenger vehicle market. To fully realise the emission targets of 2050, heavy duty trucks will also need to become zero emission vehicles. Figure 19 below shows the growth in EV stock across the globe for the period 2010 to 2020.

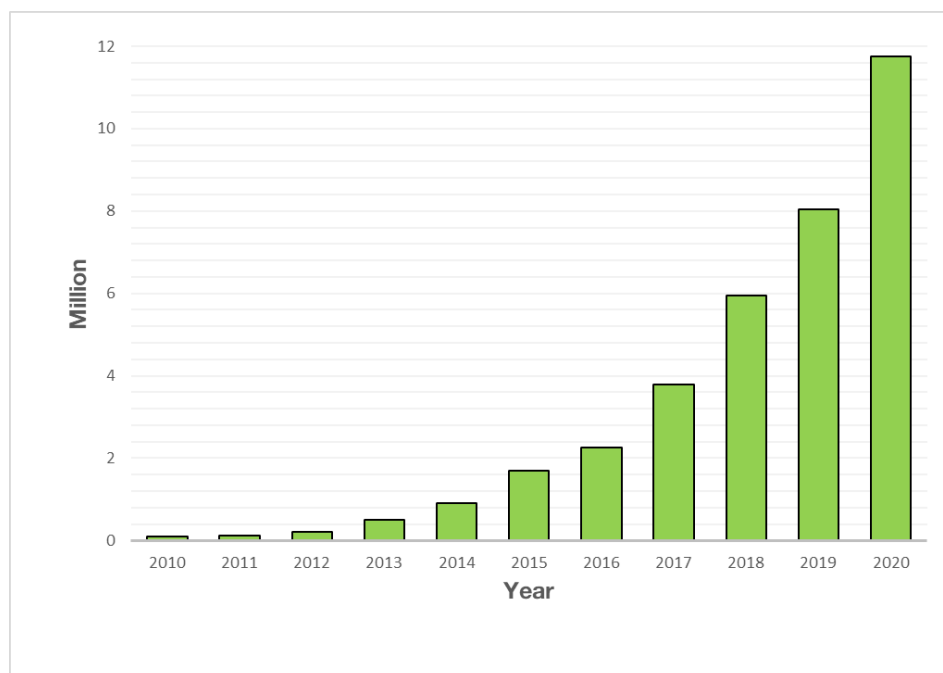


Figure 19. Global electric vehicle stock from 2010 to 2020, redrawn from IEA (2021:7).

It is clear that the BEV stock has grown rapidly in this period, surpassing 1 million units at the end of 2016 (Cazzola & Gorner, 2017). By the end of 2017, this figure rose to over 2 million vehicles sold across the globe (Moultak et al., 2017:3).

BEVs are an attractive proposition for many reasons. Sanguesa et al. (2021:372-373) mentions a few:

- Emission reduction – BEVs do not emit any carbon dioxide (CO₂) or any nitrogen dioxide (NO₂).
- Simplicity – electric motors have fewer moving components than an ICE. This makes maintenance simpler and cheaper. Electric motors also do not require a cooling circuit, transmission, clutch, and extensive sound deadening material as is the case with ICEs.
- Reliability – as electric motors have fewer moving parts, the risk of component failure is reduced. Wear and tear is also reduced.
- Cost – the maintenance and electricity costs for BEVs are lower than the maintenance and fuel costs for traditional ICE vehicles. This is illustrated in Figure 20 below.
- Comfort – BEVs benefit from electric motors in that they are much quieter than ICE vehicles. They also have less vibration.
- Efficiency – BEV efficiency is related to the energy efficiency of the source of the electricity used to charge the BEV. The wheel to wheel (WtW) efficiency, that is the efficiency of the vehicle type when the energy extraction and refining of its fuel is considered, for BEVs is up to 70% when the electricity is produced from a renewable source. In contrast, the WtW efficiency of petrol ICEs is between 11% and 27%, and between 13% to 31% for diesel ICEs.

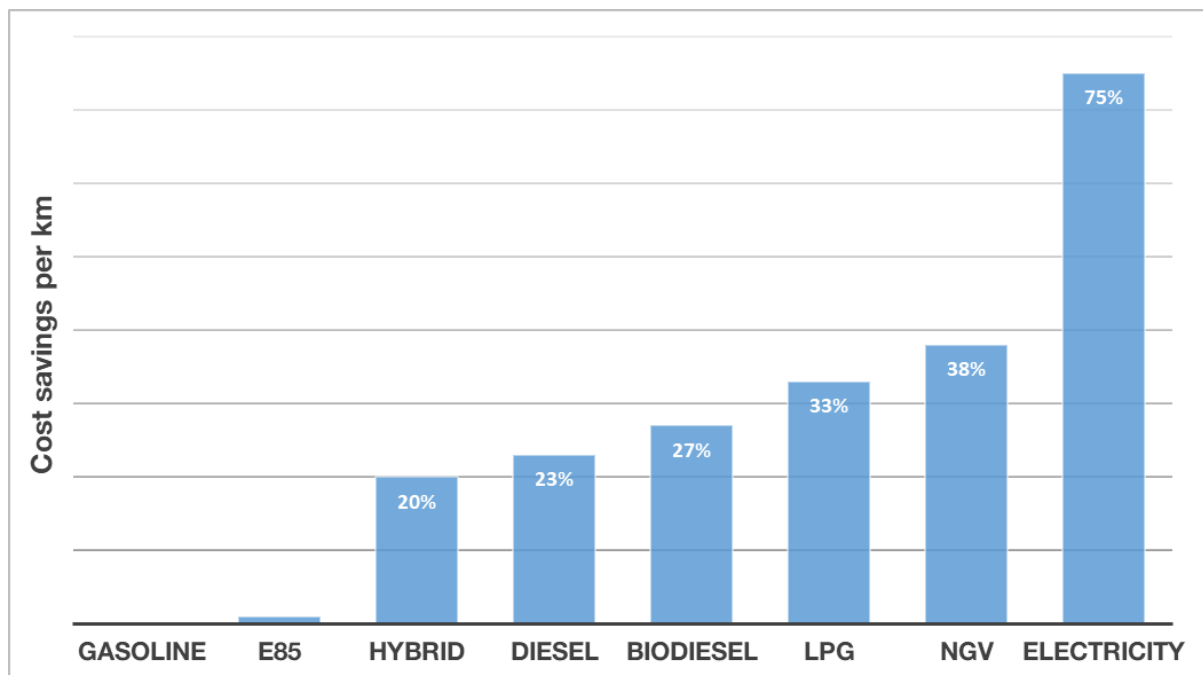


Figure 20. The savings per kilometre for vehicles with various energy sources, redrawn from Sanguesa et al. (2021:373).

What is also interesting to note is the comparison between BEVs and PHEVs in their introduction and uptake into the global vehicle market.

In Figure 21 below, it is clear that from the year 2013, BEVs have had a higher growth rate than petrol hybrid electric vehicles (PHEVs) in terms of being adopted into the global car stock (Cazzola & Gorner, 2017:22).

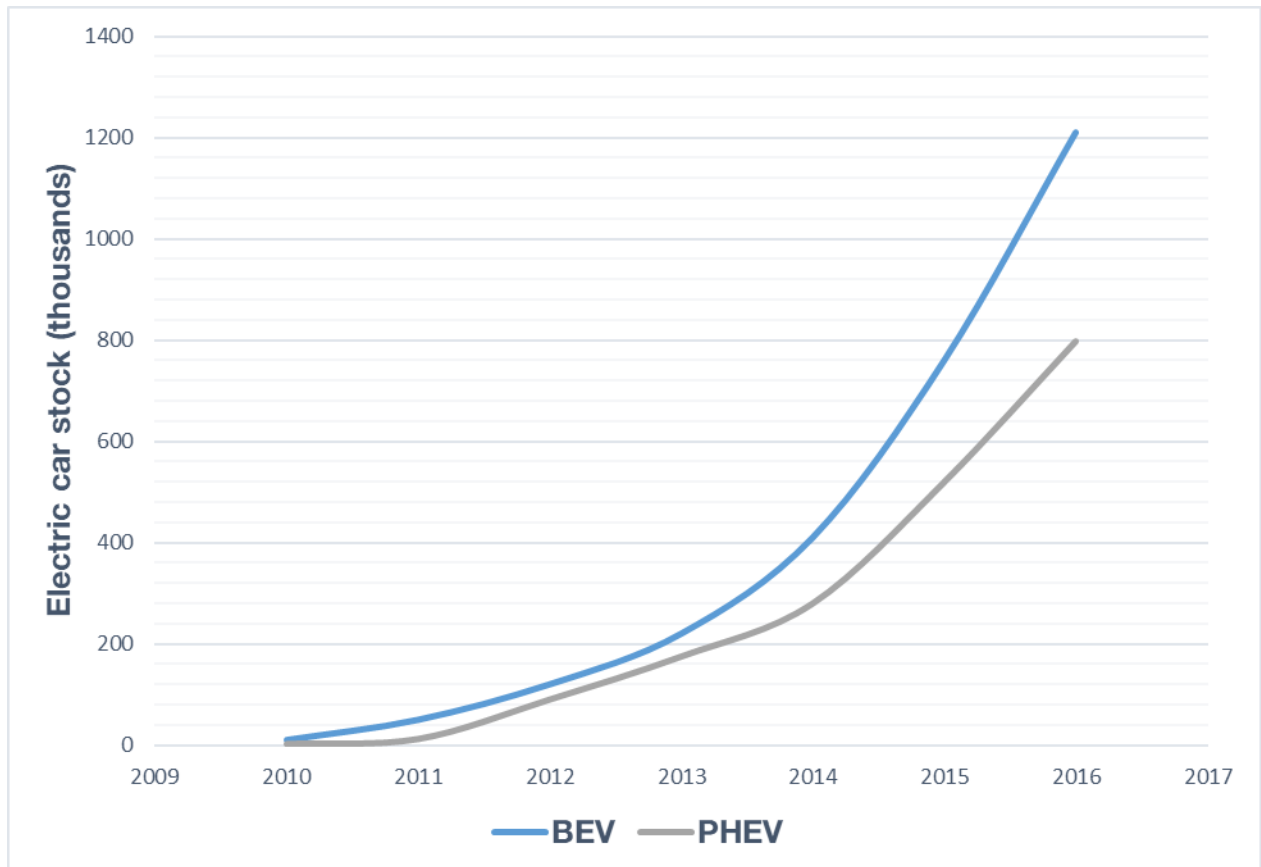


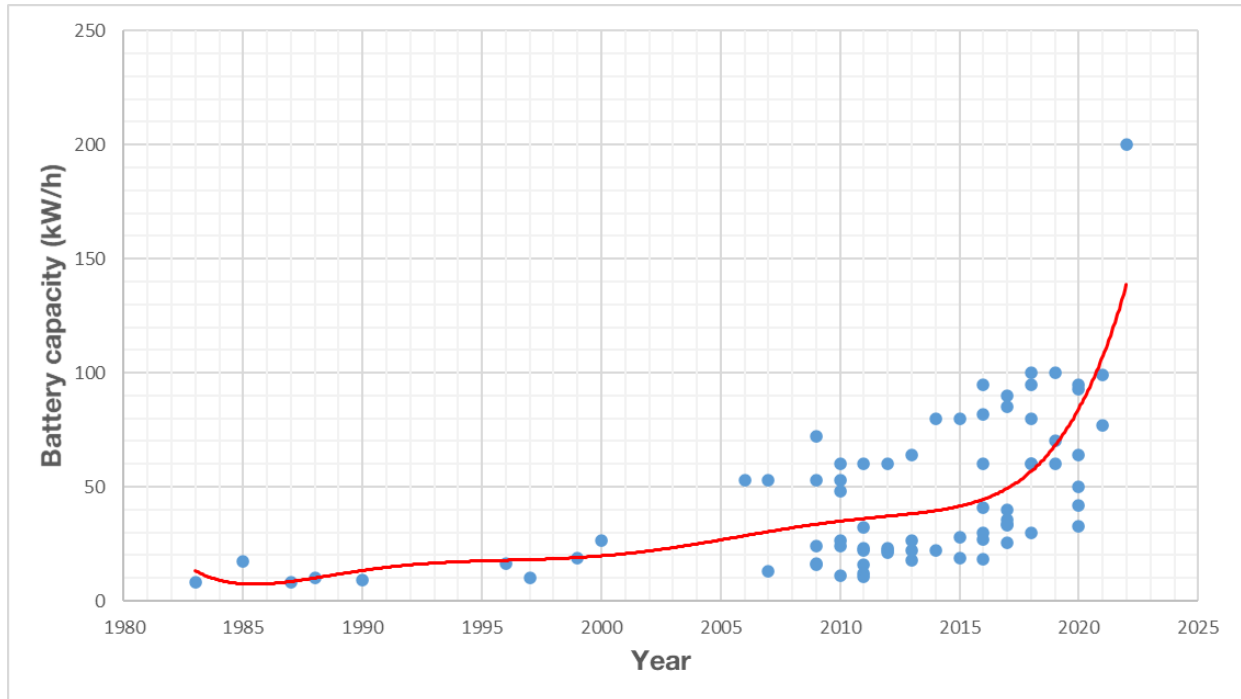
Figure 21. Evolution of the global electric car stock, 2010-16. Redrawn from (Cazzola & Gorner, 2017:22).

2.8 Batteries

The rapid adoption of BEVs into the global vehicle market has increased competition between manufacturers, which has resulted in battery technology making great strides over time. The advancement of battery technology in terms of increasing energy density and lowering manufacturing costs, has resulted in passenger vehicles becoming cheaper, as well as having longer driving ranges (Moultak et al., 2017).

2.8.1 Evolution of battery capacity

The figure below shows the progress that has been made in increasing the battery capacity for applications in automotive vehicles since 1983. The data point corresponding to 200 kW/h is the battery capacity for the Tesla Roadster, due to be on sale in 2022.



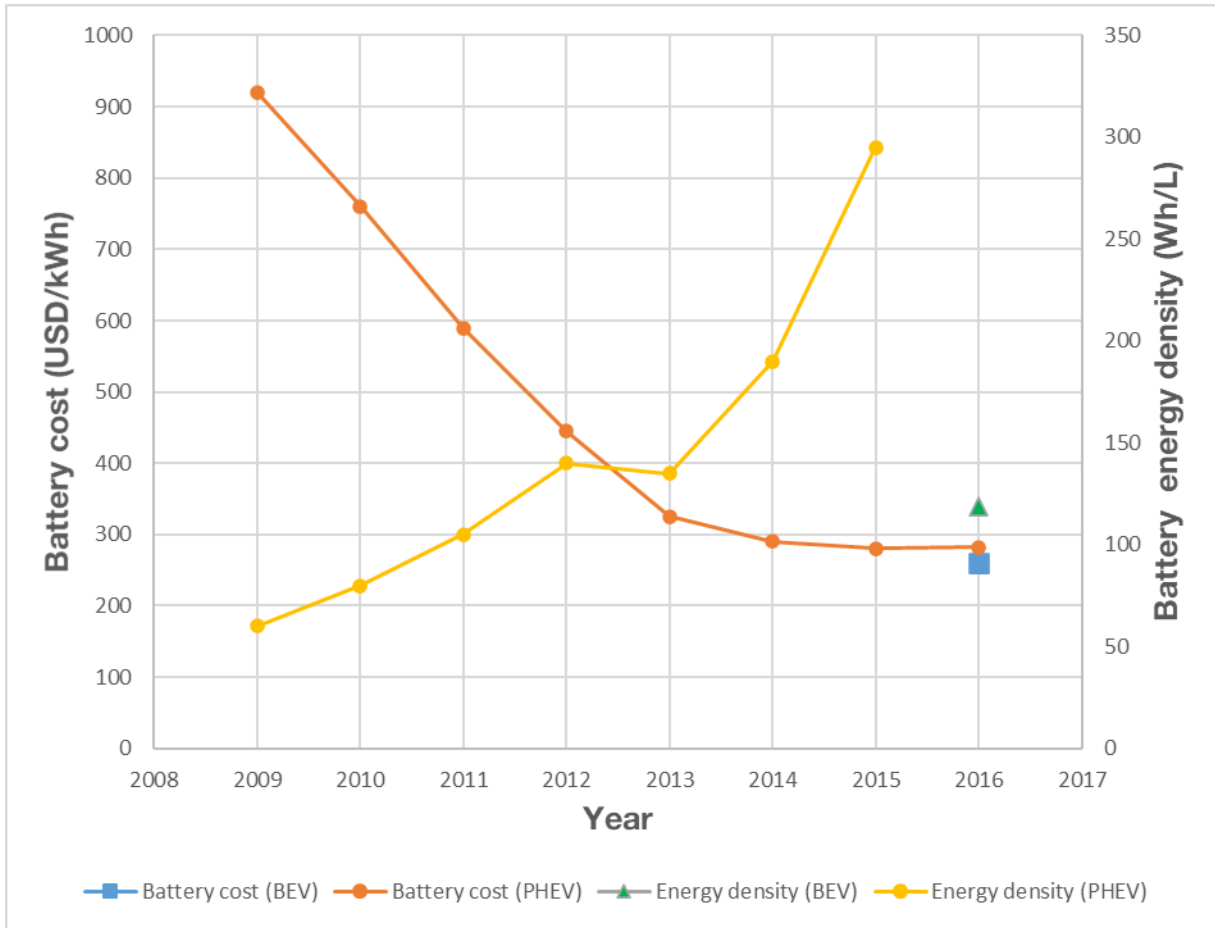


Figure 23. Evolution of battery energy density and cost, redrawn from Gazzola & Gorer (2017:14).

Figure 24 below compares the characteristics of various batteries in terms of their cycle durability (x-axis) and their energy density (y-axis). The bubble size represents specific energy. The bubble colour represents the working temperature (warmer colours represent higher working temperatures) (Sanguesa et al., 2021:385). From this it is clear that Li-Ion batteries represent the best balance between energy density and cycle durability.

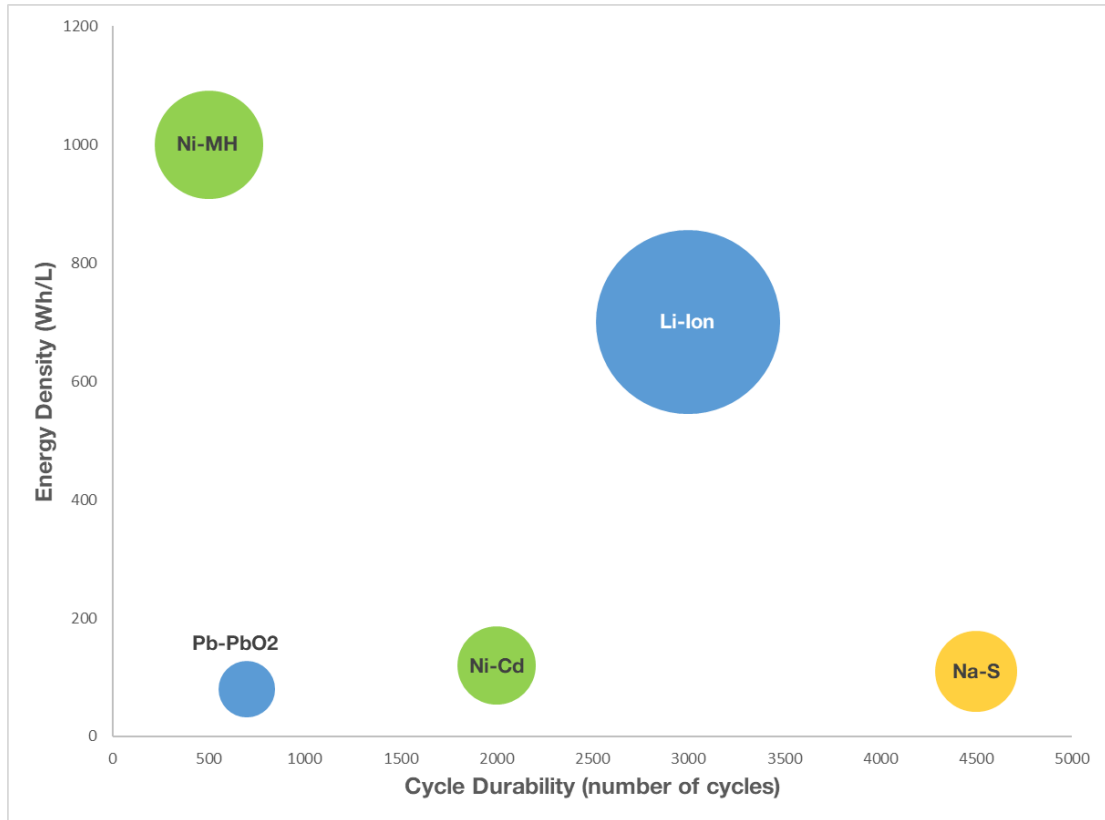


Figure 24. A comparison of battery technologies, redrawn from Sanguesa et al. (2021:385).

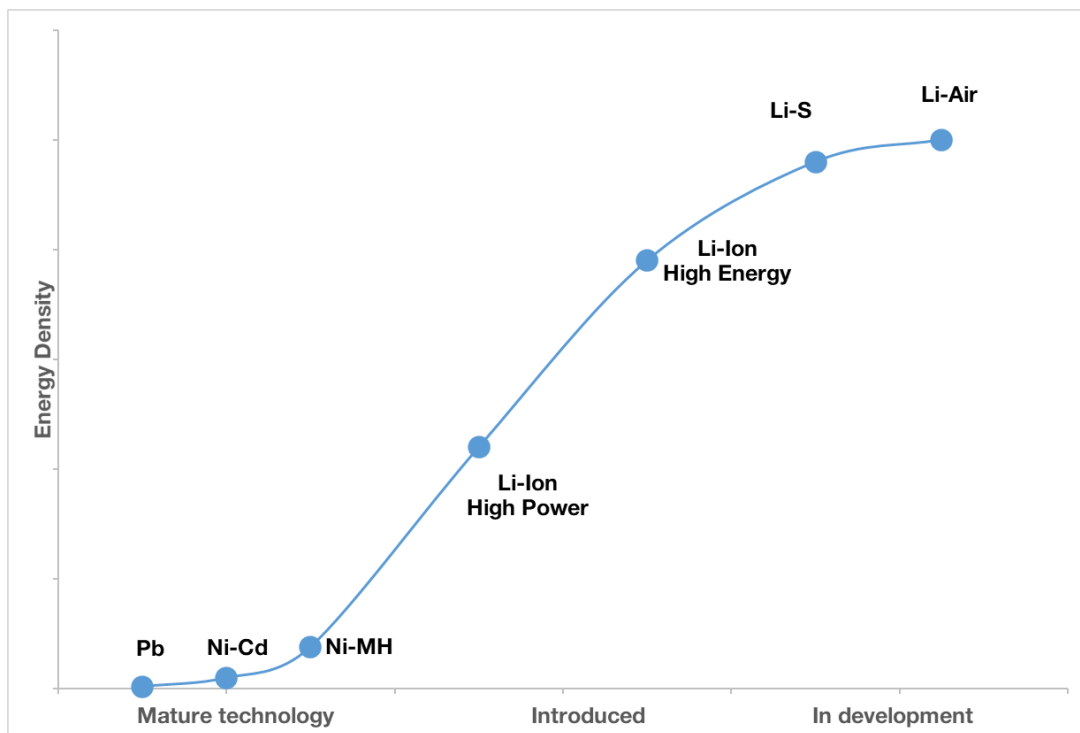


Figure 25. Expected battery developments, redrawn from Den Boer et al. (2013:22).

As depicted in Figure 25 above, Lithium-sulphur (Li-S) and Lithium-air (Li-air) are battery technologies that are currently understood to be the optimal battery chemistry for BEV applications (Den Boer et al., 2013).

Lithium-air batteries require a constant supply of oxygen (Sanguesa et al., 2021:394). This type of battery is estimated to have specific energies roughly 45 times higher than that of Li-Ion batteries (Kosivi et al., 2014:206).

2.9 Autonomous vehicles

In 2016, according to the Global Status Report, the annual road traffic deaths were 1.35 million (World Health Organization, 2018:2). In the European Union, 90% of the fatalities were directly caused by human error (Mobility and Transport, n.d.). In South Africa, this figure was 80% for the year 2015 (Verster & Fourie, 2018:5). In the USA, this figure was 94% in the year 2015 (Singh, 2018). With the high percentage of accidents caused by human error during driving, the global vehicle market has invested heavily in autonomous technology that would improve safety by allocating the decision-making process to the on-board computer (Mobility and Transport, n.d.).

In the autonomous vehicle industry, there are six levels of autonomous driving modes. These levels are shown in Table 5 below. The levels were introduced by the Society of Automotive Engineers (SAE) in 2014 (Yeong et al., 2021:2). SAE level 0 represents a driving mode where the driver is in complete control of the vehicle, including all dynamic driving tasks. SAE level 5 represents a driving mode in which the vehicle is in complete control of all dynamic driving tasks, with no human intervention required. Current manufacturers such as Audi, Volkswagen, and Tesla adopt the SAE standards in their vehicle design (Yeong et al., 2021:2).

Table 5. Overview of the SAE driving automation levels, redrawn from Yeong et al. (2021:2).

SAE Level 0	SAE Level 1	SAE Level 2	SAE Level 3	SAE Level 4	SAE Level 5
NO AUTOMATION	DRIVER ASSISTANCE	PARTIAL AUTOMATION	CONDITIONAL AUTOMATION	HIGH AUTOMATION	FULL AUTOMATION
The human driver performs all driving aspects of driving tasks, e.g., steering, acceleration, etc.	The vehicle features a single automated system for driver assistance, such as steering or acceleration/deceleration and with the anticipation that the human driver performs all remaining aspects of the driving tasks.	ADAS, The vehicle can perform steering and acceleration/deceleration. However, the human driver is required to monitor the driving environment and can take control at any time.	The vehicle can detect obstacles in the driving environment and can perform most driving tasks. Though, human override is still required.	The vehicle can perform all aspects of the dynamic driving tasks under specific scenarios. Geofencing is required. Human override is still an option.	The vehicle performs all driving tasks under all conditions and scenarios without human intervention.
The human drivers monitor the driving environment			The automated system monitors the driving environment		

2.10 Sensors used by autonomous vehicles

Autonomous vehicles are able to operate without human intervention, or human control. They are able to perform this operation due to the variety of sensors on-board the vehicle, such as cameras, ultrasonic radar and LiDAR (light detection and ranging). Sensors are pivotal for the perception and interpretation of the environment in which an autonomous vehicle navigates.

All of these sensors provide an input for the vehicle's computer system regarding the objects that are sensed in the vehicles environment. The vehicle makes sense out of all of these inputs using a process known as sensor fusion. In this process, the sensor inputs are fed into a central computer, which combines the data to enable the computer to make driving decisions (Liu et al., 2017:41-45). The benefit of sensor fusion is that the vehicle does not rely on only one type of sensor for information of its surroundings.

Much in the same way that current blind-spot sensors and warning systems serve as a backup for the human driver, multiple sensor types in autonomous vehicles provide redundancy which improves the safety of the system.

A brief summary on the various types of sensors is given below.

2.10.1 Cameras

The use of cameras in vehicles is not a new phenomenon. The majority of new vehicles being sold are fitted with cameras to aid in parking and manoeuvring, adaptive cruise control, and lane departure warnings. Cameras provide a wealth of information, colour video, texture and contrast data (Liu et al., 2017:3). This data is evaluated by the vehicle's computer to reliably identify road markings, road signs, traffic lights, other vehicles and pedestrians (Yeong et al., 2021:6).

While cameras are useful in providing the input data mentioned above, they have some shortcomings as well. They are not very reliable sources of data in adverse weather or darkness since they rely on the objects they detect being illuminated. They do not provide any distance information with regards to the objects they detect.

Figure 26 below shows the general field of view of camera systems fitted to autonomous vehicles.

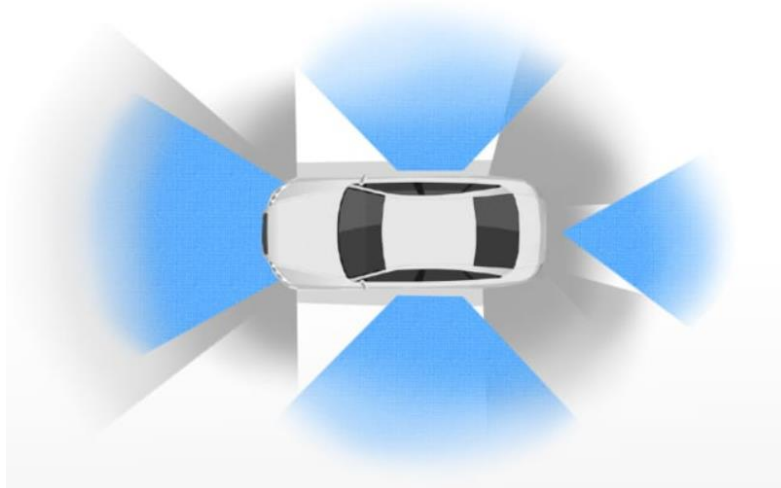


Figure 26. Camera vision in autonomous vehicles (Petit, 2020).

2.10.2 Radar

Radio Detection and Ranging (radar) has long been used in the transport industry. It is the underlying technology used in traffic speed cameras. Radar works by emitting short pulses of electromagnetic waves at an object. The waves bounce off the object and back to the sensor. The speed of this wave is a known quantity, thus from this the distance to the object can be ascertained with great accuracy. When doing several measurements one after the other, the speed of the object can also be determined.

Radar has been introduced in mainstream vehicles in the form of parking aids, emergency brake assistance systems, adaptive cruise control and collision avoidance. Unlike cameras, radar is cheap, and works even in adverse conditions. Radar however, does not provide high resolution data. In other words, radar is able to detect objects but lacks the resolution needed to classify them.

Autonomous vehicles use two types of radar systems: short-range and long-range. Short-range radar provides information for objects within 30 meters of the vehicle. This data is used for parking aids, blind spot monitors and collision warning. Long-range radar provides information for objects up to 250 meters away from the vehicle, and also provides information about their speed. The data from long-range radar is used in the adaptive cruise control and emergency brake assistance systems (Liu et al., 2017:3,44). Figure 27 below shows the general placement and field of view of radar systems in autonomous vehicles.

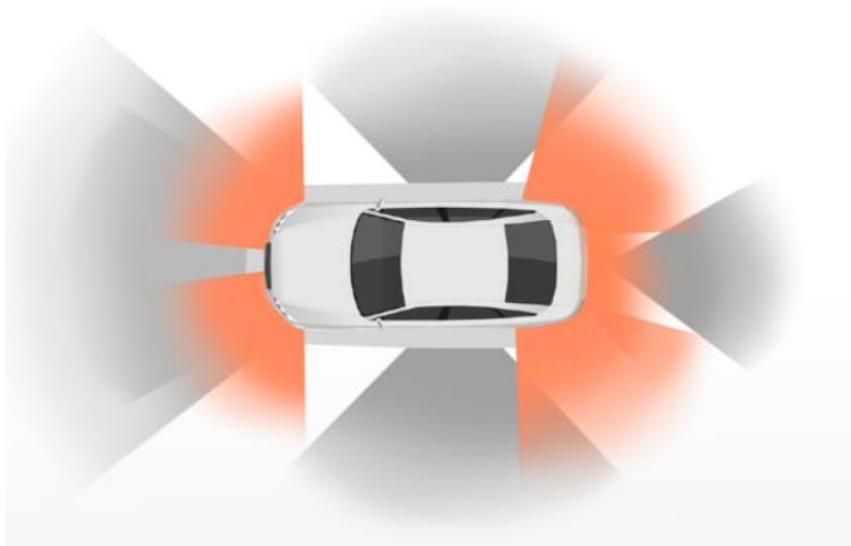


Figure 27. Radar field of view in an autonomous vehicle (Petit, 2020).

2.10.3 Ultrasound

Ultrasonic sensors are now almost standard equipment on new vehicles. They are spotted as small round inserts in the front and rear bumpers of cars. They provide the distance information for objects in the near vicinity of the vehicle. Generally, these sensors have a sensing range below 10 meters (Liu et al., 2017:51). Figure 28 below shows the limited range of ultrasonic sensors.

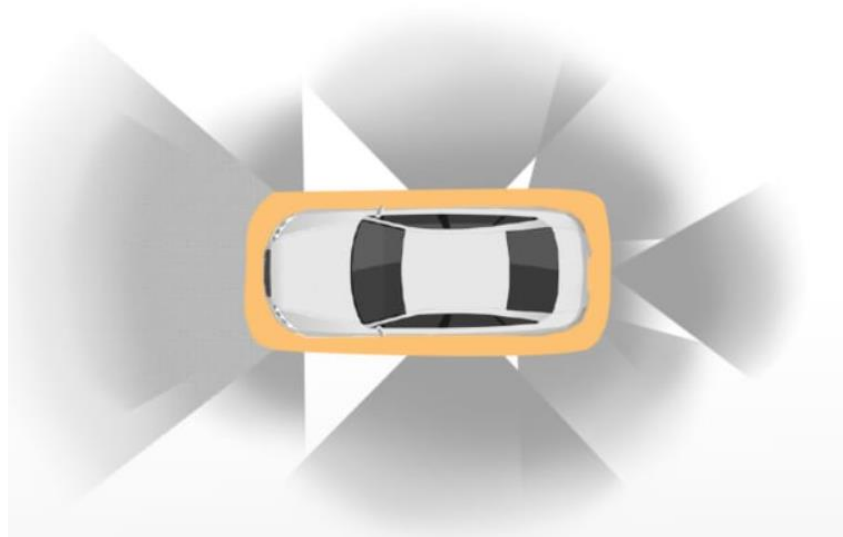


Figure 28. Ultrasonic field of view in an autonomous vehicle (Petit, 2020).

2.10.4 Lidar

Perhaps the most important technology for the advancement of the autonomous vehicle industry is LiDAR. LiDAR sensors provide high quality, reliable, high resolution 3D data of a vehicle's environment. It can provide this data at low or high speeds and over a long range (Petit, 2020).

LiDAR sensors send out nearly one million laser pulses per second to objects. The reflected pulses are received by a detector. The data received allows the computer to create a very high-resolution 3D map of the environment in the form of a point cloud (Yeong et al., 2021:8). The richness of the detail in this map allows not just for object recognition, but also for these objects to be categorized (Liu et al., 2017:5).

Figure 29 below shows the general placement and field of view of LiDAR systems in an autonomous vehicle.



Figure 29. General LiDAR field of view in an autonomous vehicle (Petit, 2020).

2.10.5 Sensor fusion

The prime focus of autonomous vehicles, and a major factor in their adoption into the global automotive market, is safety. The combination of the various sensors mentioned above in the sensor fusion process enables the computer to make more informed and reliable driving decisions (Liu et al., 2017:41-45). With each system complementing and assisting the others, the weaknesses of one is compensated for by the others. Figure 30 below shows the overlap of the various sensor systems.

Camera | Radar | Ultrasonic | Lidar

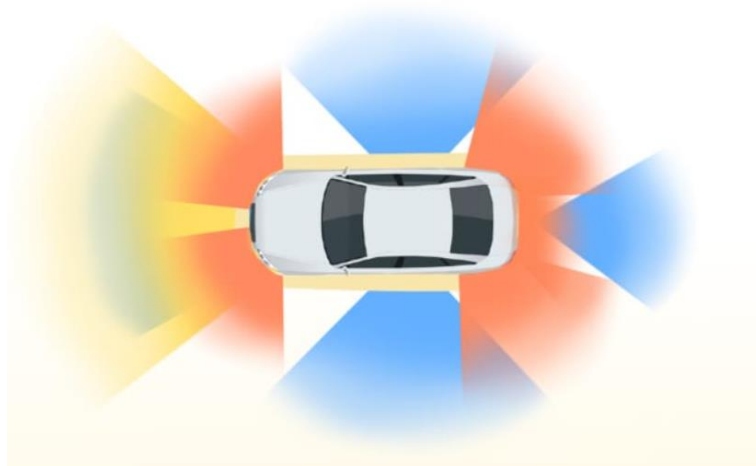


Figure 30. Sensor fusion in an autonomous vehicle (Petit, 2020).

Chapter 3

Technical background

3.1 Introduction

The main objective of this research is to ascertain what C_D can be expected of an optimised autonomous battery electric truck-trailer combination, and to ascertain the energy saving of an autonomous BET compared to a modern ICE truck-trailer. Since a modern truck has very complex geometry, the truck geometry used for this research was treated as a bluff body. In modern BEVs, the side mirrors are replaced by small cameras in an aerodynamic housing. This serves to reduce the aerodynamic drag of the vehicle, thereby increasing energy efficiency and extending the driving range. Since a bluff body was used to represent the truck in this study, the side mirror cameras were excluded from the geometry. This reduced the complexity of the model and also reduced the time it needed for the CFD simulation to complete. Other features such as headlights and their housings, vehicle number plate, various sensor housings, and cooling ducts were omitted for the reason stated previously. This chapter expands on the theory and technical background of the research problem.

3.2 Aerodynamics

Aerodynamics is defined as the study of motion and forces acting on objects in a moving fluid (Anderson, 2010:11). Consider Figure 31 below: if an object is placed in an airflow, then the lift force is defined as the component of the net force acting perpendicular to the airflow, and the drag force is defined as the component of the net force acting parallel to the airflow.

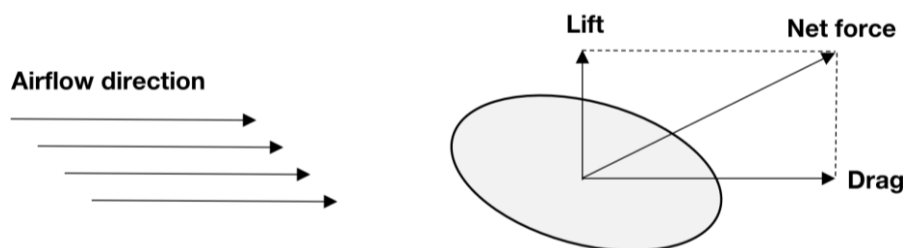


Figure 31. The lift and drag acting on a body as a result of being immersed in an airflow.

3.2.1 Aerodynamic drag

A body that is in motion through a fluid will experience a drag force. This drag force is divided into two kinds of aerodynamic drag: pressure drag and skin frictional drag (Anderson, 2010:1040).

Frictional drag is caused by the friction which is created by the fluid flowing over body surface, and pressure drag results from the eddy characteristics created in the fluid when the body passes through it (Anderson, 2010:79).

Figure 32 below shows the contributions of skin friction drag and pressure drag acting on various geometries. Pressure drag is dominant in bluff bodies due to the airflow wake that these bodies leave behind them.

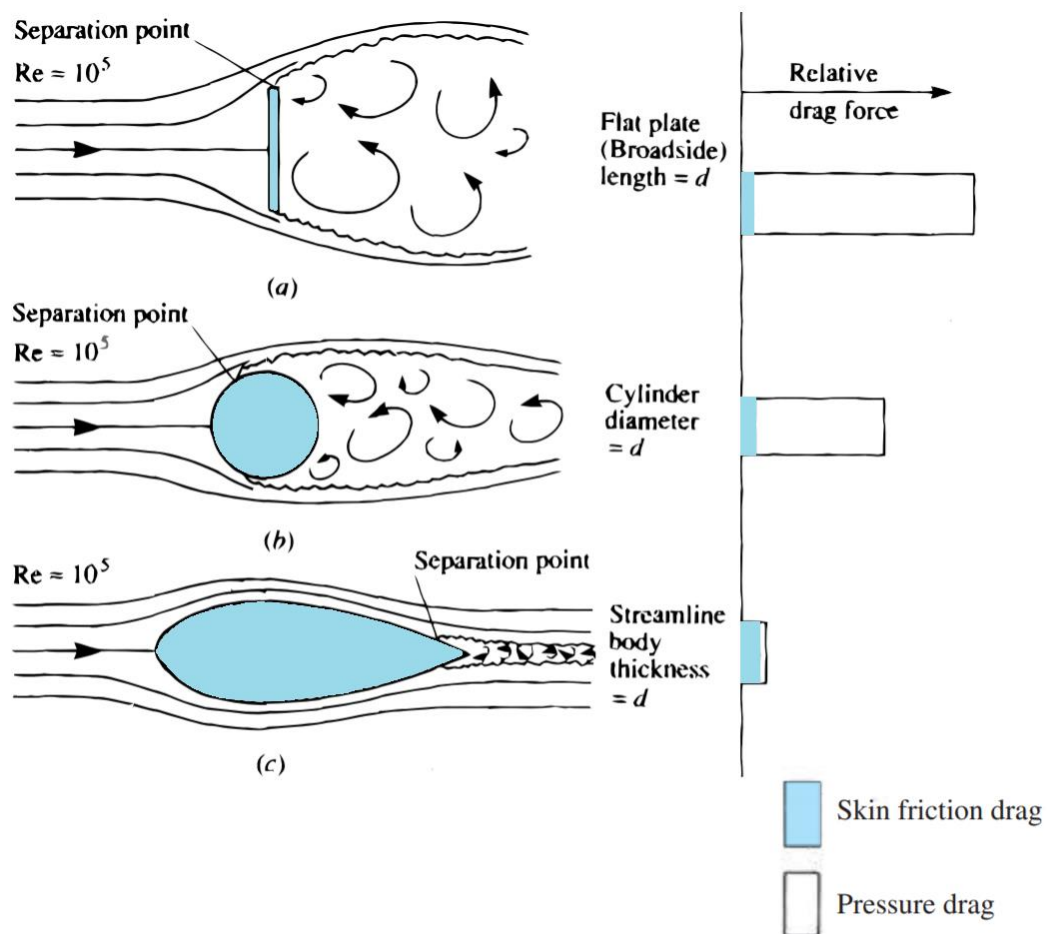


Figure 32. The effects of skin friction drag and pressure drag for various geometries, redrawn from (Talay, 1975).

Experiments have shown that aerodynamic drag is directly proportional to the square of the velocity of the vehicle, with other components of drag changing only marginally (Katz, 2016:6).

The coefficient of drag (C_D) is a non-dimensional number which can be thought of as a number which quantifies the aerodynamic sleekness of a vehicle (Katz, 2016:6).

The mathematical description of C_D is given by:

$$C_D = \frac{F_D}{0.5\rho V_\infty^2 A} \quad (3.1)$$

Where F_D is the drag force, V_∞ is the free stream velocity, ρ is the density of the fluid, and A is the projected cross-section frontal area of the vehicle.

3.2.2 Bluff bodies

Bluff body aerodynamics is the study of aerodynamics where the drag force is considered to be most important aspect of the airflow over a body. When the aerodynamic drag on an object is dominated by the effect of pressure drag, then this body is called a bluff body (Fan et al., 2020:2).

In commercial trucks, pressure drag accounts for more than 80% of the total aerodynamic drag acting upon it (Motor Industry Research Association, 2001:6). The main contributor to pressure drag is flow separation, where the airflow detaches from the contours of the body over which it is flowing. Further downstream from this separation, the airflow begins to rotate or spiral in an unsteady way. This rotational airflow (eddies) dissipates energy and decrease the pressure in these separated regions of the airflow (Motor Industry Research Association, 2001:6). Figure 33 below shows some of these effects on a simplified truck body.

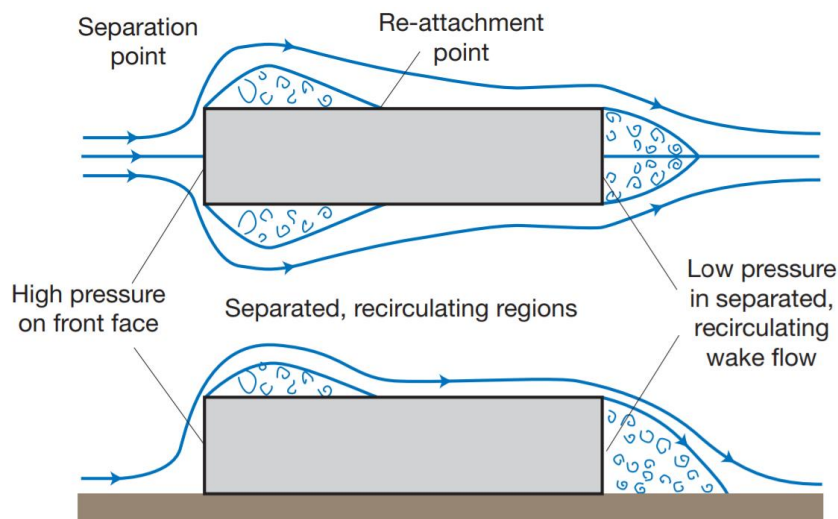


Figure 33. Streamline diagram with the plan view above and side view below (Motor Industry Research Association, 2001:6).

From Figure 33 above, it is clear that there is a large pressure difference between the front of the truck and the rear of the truck, due to flow separation regions. This large pressure difference results in increased pressure drag.

The sharp corners at the front and the rear of this geometry promotes the occurrence of flow separation. It can also be seen that separated flow can eventually reattach to the body further downstream.

Figure 34 below shows the difference in flow characteristics between a typical un-aerodynamic truck and a subtly aerodynamically improved truck.

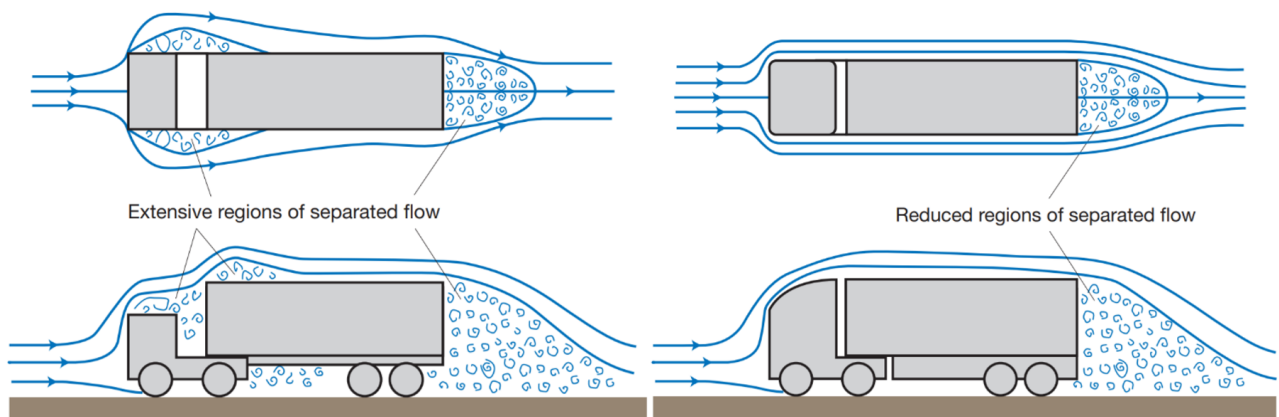


Figure 34. Typical airflow around an un-aerodynamic truck (left) and an aerodynamically effective truck (right) (Motor Industry Research Association, 2001:9).

From the figure above it is clear that subtle rounding of the edges of the front of the truck, adding a cab deflector, as well as reducing the gap between the cab and the trailer results in greatly reduced flow separation in these regions. This reduction in flow separation reduces the overall pressure drag on the truck. The process of altering the geometry of a shape to minimise flow separation as much as possible is called “streamlining” (Motor Industry Research Association, 2001:9).

3.2.3 Boundary layer

As an object moves through a fluid, air for example, the molecules of air that are close to the object are disturbed and have to move around the object. The result of this is that aerodynamic forces between the airflow and the object are created (Anderson, 2010:11-12).

These aerodynamic forces are greatly influenced by the viscosity of the airflow. Consider the airflow over a surface; the air molecules just on the surface tend to stick to that surface. These stagnant molecules at the surface influence the moving air molecules just above them, causing the airflow above the stagnant molecules to be slowed down. Moving further away from the surface, the air molecules are less impeded by slower air molecules closer to the surface. The result of this phenomenon is that there is a thin layer of air molecules at the surface of the object. Within this thin layer, the velocity changes from zero at the surface of the object to the free stream velocity of the airflow at some distance away from the surface. This thin layer is called the boundary layer (Katz, 2016:132).

The boundary layer increases in thickness as it moves further downstream along the surface (Genta & Morello, 2020:122). The airflow within the boundary layer can

eventually come to a stop, creating a stagnation zone. Once this happens the airflow separates from the object surface, which could then lead to wake formation and a pressure drop which increases the aerodynamic drag (Genta & Morello, 2020:123).

Figure 35 below shows the increase in boundary layer thickness, velocity changes as well as the airflow separation point.

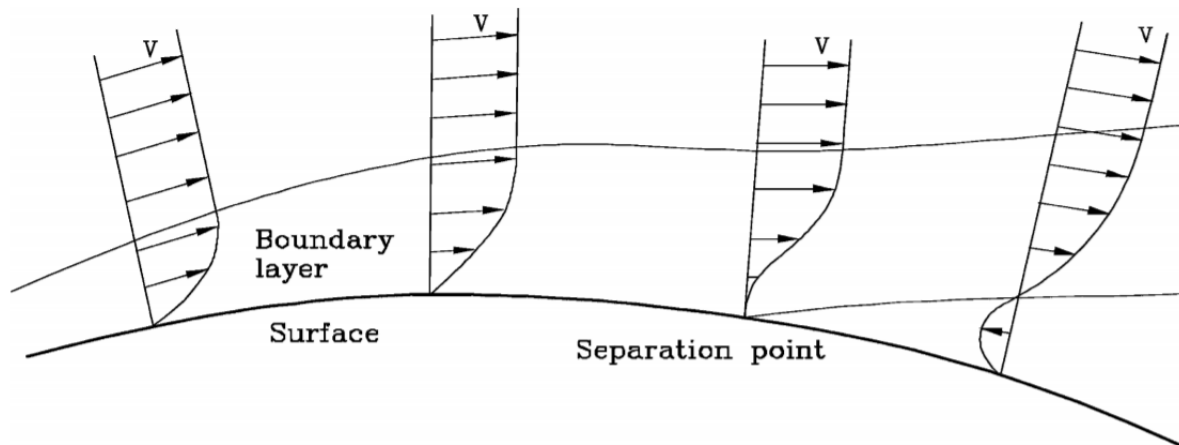


Figure 35. Boundary layer: Velocity distribution in direction perpendicular to the surface. The separation point is also represented (Genta & Morello, 2020:123).

The boundary layer can either be laminar or turbulent depending on what the Reynolds number value is for the airflow. The Reynolds number is simply a ratio of inertial forces to viscous forces (Anderson, 2010:38). The Reynolds number is related to the kinematic viscosity of the airflow, the velocity of the object moving through the medium (air), as well as the length of the object over which the air flows.

The boundary layer can be considered to be laminar for low Reynolds number flows. This laminar flow regime is characterised by uniform stream-wise velocity changes as distance from the surface increases (Anderson, 2010:376).

The boundary layer can be considered turbulent for high Reynolds numbers. This turbulent flow regime is characterised by unsteady stream-wise velocity changes (Anderson, 2010:376).

The boundary layer can also transition between laminar to turbulent depending on the Reynolds number related to the airflow.

3.2.4 Boundary layer separation

When an object geometry transitions sharply, or progresses from a smooth profile to a blunt profile, then the airflow is said to separate. This phenomenon is known as boundary layer separation, sometimes referred to as airflow separation, or simply flow separation. This separation can be seen in case (b) in Figure 36 below.

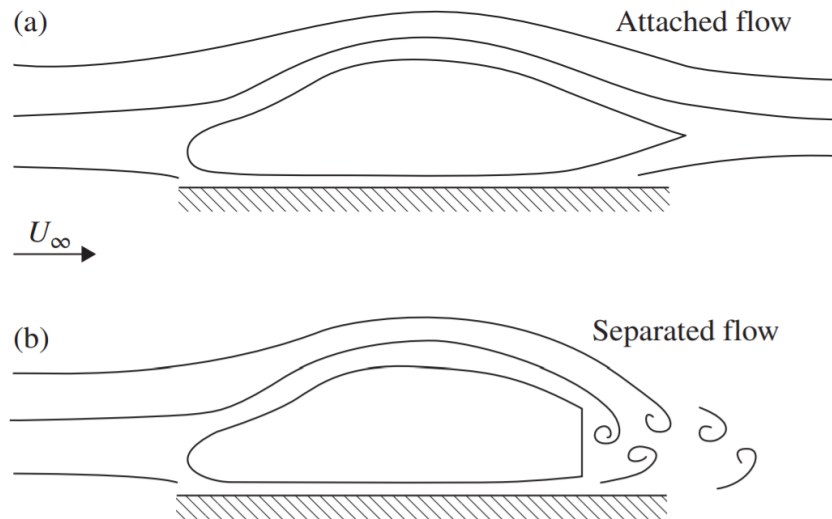


Figure 36. Attached flow over (a) a streamlined car and (b) the locally separated flow behind a more realistic automobile shape (Katz, 2016:13).

Separation can also occur over smooth edges without a sharp change in geometry, which can happen if the flow velocity around a body drops considerably. When this happens, the static pressure increases to a point where it forces the flow to push in the opposite direction, as can be seen in the fourth velocity distribution plot in Figure 35.

Airflow separation results in large increases in pressure drag over the object. The energy that is dissipated in the turbulent region, or wake just after the separation point, results in a large pressure drop over a body. This pressure drop across the object is what gives rise to the large increase in pressure drag due to flow separation (Anderson, 2010:895-899).

3.2.5 Aerodynamic forces and moments

For automotive vehicles, the components of aerodynamic force and moment are decomposed with reference to some frame xyz (Genta & Morello, 2020:125). With reference to Figure 37:

- The longitudinal aerodynamic force is shown as F_x
- The lateral aerodynamic force is shown as F_y
- The normal aerodynamic force is shown as F_z
- The rolling moment is shown as M_x
- The pitching moment is shown as M_y
- The yawing moment is shown as M_z

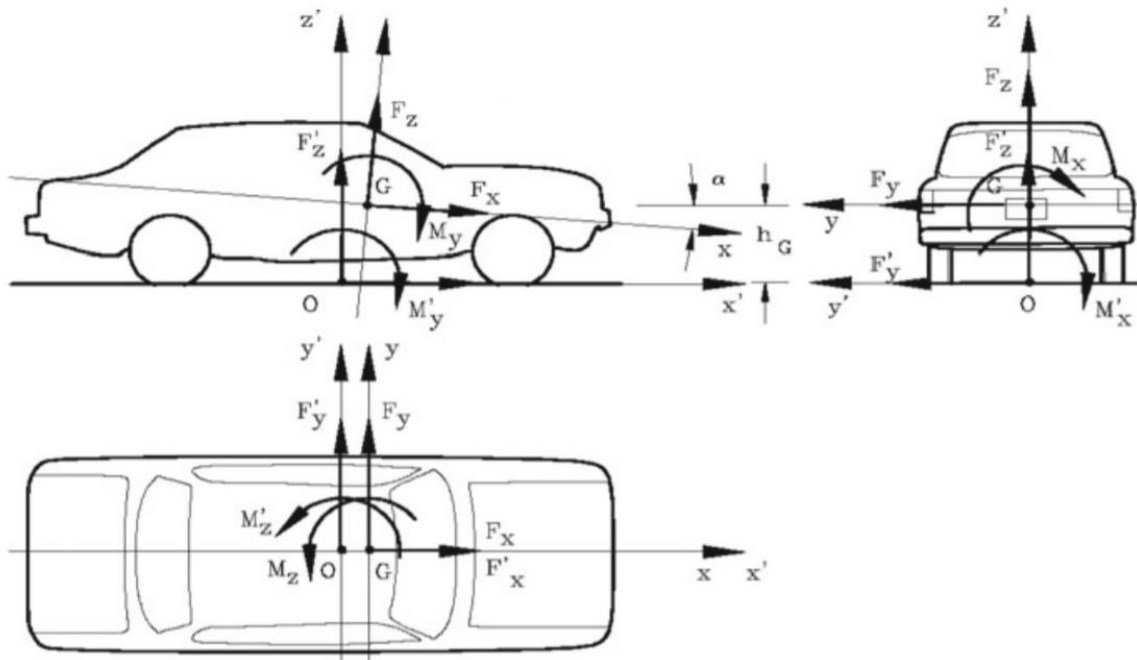


Figure 37. Reference frame often used to express aerodynamic forces, redrawn from (Genta & Morello, 2020:126).

With reference to Figure 37, in wind tunnel tests the forces and moments on the vehicle are expressed as components to a reference frame that is placed with its origin located at mid-wheelbase (Genta & Morello, 2020:126).

The angle α is known as the aerodynamic angle of attack, and in most cases is assumed to be equal to zero (Genta & Morello, 2020:126).

3.2.6 Aerodynamic field

If we consider a stationary vehicle which has air flowing over it, as in Figure 38 below:

- At point A, the flow divides below and above the vehicle. Point A is the stagnation point of the stream (Genta & Morello, 2020:134).
- At point C, the airflow detaches from the vehicle surface. A separation bubble is created between points C and D. In this zone the airflow is turbulent and the pressure is high (Genta & Morello, 2020:135).
- Between points E and F, the pressure is low as the air velocity increases.
- After point F, the airflow slows down and the pressure rises. A result of this is that the airflow becomes detached as the rear window slopes away sharply.
- There are some cases where the airflow can reattach to the body surface, as in Figure 38 (b). This reattachment can sometimes give rise to another separation bubble.
- The detachment can be delayed if the rear window slopes away at a shallower angle, as can be seen in Figure 38 (c). In this case the airflow remains attached after flowing over the roof, only detaching at the end of the body. This results

in the creation of a smaller wake behind the car, as can be seen when comparing the airflow behind the vehicle in cases (b) and (c).

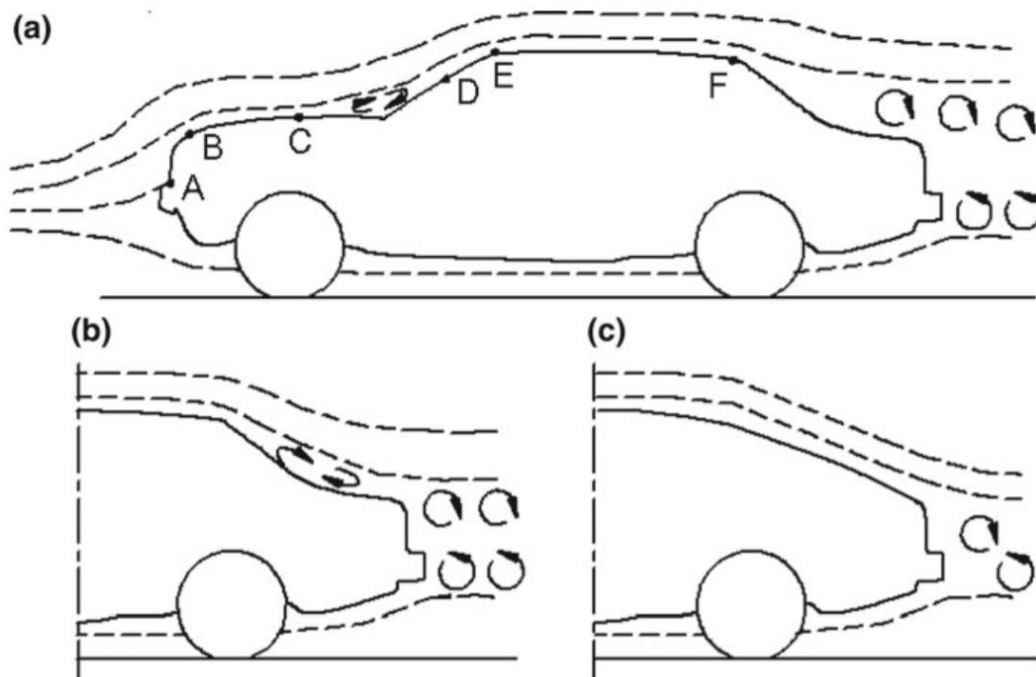


Figure 38. Streamlines over a vehicle (Genta & Morello, 2020:134).

The airflow under the vehicle is complex and dependant on factors like the streamlining of the underbody, the height of the underbody relative to the ground, roughness of the underbody, as well as other factors.

The airflow under the vehicle can reduce the overall drag of the vehicle, as it increases the pressure in the wake created behind the vehicle (Genta & Morello, 2020:137). The underbody of a vehicle can be streamlined as well, and this in turn adds to a drag reduction effect.

With reference to Figure 39 below, it is clear that a well streamlined underbody can reduce the overall drag of the vehicle up to between 10-15% (Genta & Morello, 2020:138).

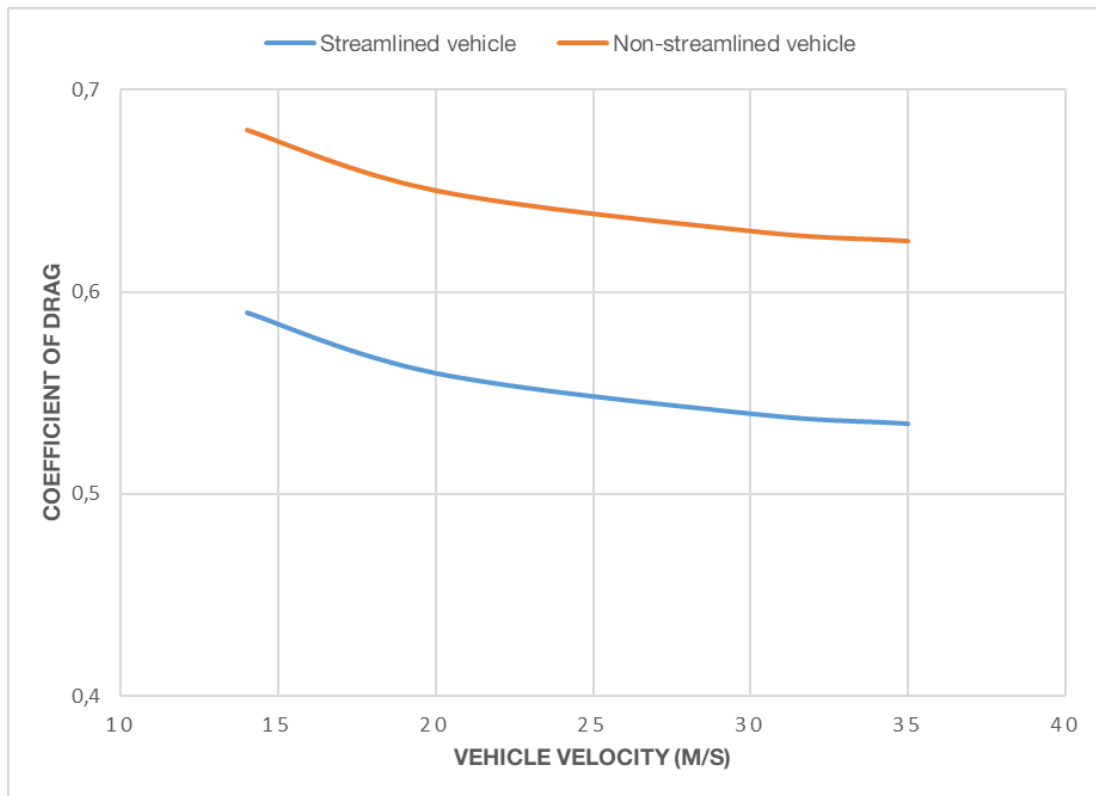


Figure 39. Effect of streamlining the underbody of a vehicle on the aerodynamic drag coefficient, redrawn from (Genta & Morello, 2020:138).

With an autonomous BEV, the underbody streamlining is easier to achieve as there are fewer mechanical systems to navigate over and around. A flat underbody promotes airflow attachment over its surface, reducing turbulence and drag (Genta & Morello, 2020:135-138).

In wind tunnel simulations the ground is stationary relative to the vehicle, which does not represent reality which is that the ground is stationary relative to the air (Genta & Morello, 2020:135). Therefore, it is important to simulate the effects of a moving road, or a moving ground plane, to account for the aerodynamic effect this has on the airflow under the vehicle.

Figure 40 below shows the boundary layer formed underneath a vehicle travelling along the road (a), and remaining stationary in a wind tunnel (b). It can be seen that the velocity profile of the airflow, shown in the second detail view of case (b), is dramatically different to that of the velocity profile of the airflow under the vehicle in case (a). With reference to case (b), this velocity profile is a result of two boundary layers forming underneath the vehicle; one from the floor surface and one from under the vehicle.

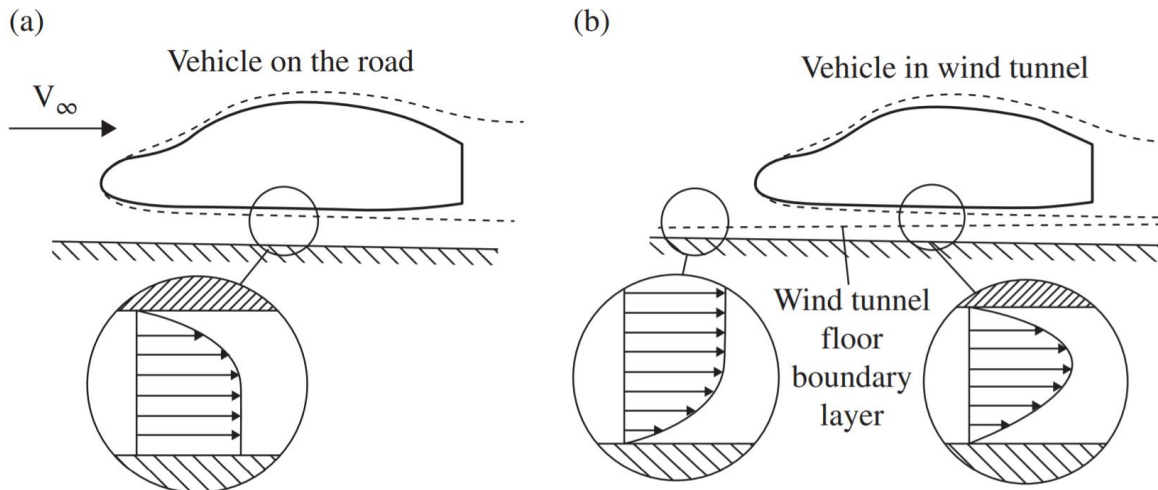


Figure 40. The moving ground problem: (a) On the road there is a boundary layer on the vehicle underbody, and (b) In a wind tunnel with stationary floor, there are two boundary layers under the car, and the flow is different (Katz, 2016:281).

3.3 Computational fluid dynamics (CFD)

In basic terms, CFD is the analysis of complex fluid dynamic systems by the use of computer based simulation. It is a technique used across many industries, namely automotive, aerospace, ship hydrodynamics, turbomachinery, and biomedical engineering among various other industries. The benefits of CFD is that it provides reliable data for conceptual studies, redesigns, and as well as reducing the cost of having to do laboratory experiments where CFD analysis could be trusted instead.

The mathematical equations defining fluid dynamics in a three dimensional space are highly complex, and very difficult to solve for an arbitrary case. Added to this complexity, the classical approach is limited in terms of visualising flow fields and takes a significant amount of time to solve.

In past decades and especially in the last 5 years, computing power and capacity has increased significantly, as well as improvements in the numerical methods of solving fluid problems. This has allowed for software to be created that can solve complex three dimensional nonlinear fluid dynamics problems (Katz, 2016:316).

This numerical approach starts by first creating a numerical approximation for the equations for the fluid dynamics. The domain is then discretized into smaller cells, sometimes called a grid. The fluid dynamic equations are then applied to this grid. At each point on the grid, the equations are specified. This allows for the complex nonlinear partial differential equations to be replaced by basic algebraic equations which can be solved iteratively (Katz, 2016:316).

3.3.1 Fluid dynamic laws of conservation

As stated by Versteeg & Malalasekera (2007:9), the equations that accurately describe fluid dynamics are mathematical representations of the basic laws of conservation in physics, namely: the mass of the fluid is conserved and the total of all forces on a fluid particle is equal to the rate of change in momentum for that particle. These two laws are described by the equations below.

Unsteady three dimensional conservation of mass at any point in an incompressible fluid:

$$\frac{\partial(\rho u)}{\partial x} + \frac{\partial(\rho v)}{\partial y} + \frac{\partial(\rho w)}{\partial z} = 0 \quad (3.2)$$

Unsteady three dimensional conservation of linear momentum at any given point in an incompressible fluid:

$$\rho \left(\frac{\partial v_x}{\partial t} + v_x \frac{\partial v_x}{\partial x} + v_y \frac{\partial v_x}{\partial y} + v_z \frac{\partial v_x}{\partial z} \right) = -\frac{\partial \rho}{\partial x} + \mu \left(\frac{\partial^2 v_x}{\partial x^2} + \frac{\partial^2 v_x}{\partial y^2} + \frac{\partial^2 v_x}{\partial z^2} \right) + \rho g_x \quad (3.3)$$

$$\rho \left(\frac{\partial v_y}{\partial t} + v_x \frac{\partial v_y}{\partial x} + v_y \frac{\partial v_y}{\partial y} + v_z \frac{\partial v_y}{\partial z} \right) = -\frac{\partial \rho}{\partial y} + \mu \left(\frac{\partial^2 v_y}{\partial x^2} + \frac{\partial^2 v_y}{\partial y^2} + \frac{\partial^2 v_y}{\partial z^2} \right) + \rho g_y \quad (3.4)$$

$$\rho \left(\frac{\partial v_z}{\partial t} + v_x \frac{\partial v_z}{\partial x} + v_y \frac{\partial v_z}{\partial y} + v_z \frac{\partial v_z}{\partial z} \right) = -\frac{\partial \rho}{\partial z} + \mu \left(\frac{\partial^2 v_z}{\partial x^2} + \frac{\partial^2 v_z}{\partial y^2} + \frac{\partial^2 v_z}{\partial z^2} \right) + \rho g_z \quad (3.5)$$

Where g is gravity, ρ is the fluid density, (u, v, w) are the velocity components of the fluid, μ is the viscosity of the fluid, t is time, and (x, y, z) are Cartesian coordinates.

(3.3), (3.4), and (3.5) are known as the Navier-Stokes equations.

3.3.2 Reynolds-averaged Navier-Stokes equations

Most CFD software does not actually aim to solve the Navier-Stokes equations directly, because for high Reynolds number flows the computing power demands are too high.

The Reynolds-averaged Navier-Stokes (RANS) equations consider the effects of fluctuations in turbulence of the airflow, with respect to the Navier-Stokes equations. RANS are time-averaged equations which provide approximate solutions for the Navier-Stokes equations (Versteeg & Malalasekera, 2007:62).

Most scientific instruments used today which measure pressure or velocity do not report instantaneous quantities, rather they report average quantities. The reason for this averaged reporting over quantised volumes and time periods is that the instruments are not sensitive enough to report instantaneous fluctuations in velocity and pressure, as found in turbulent flow.

The RANS equations simplify things by splitting the instantaneous time dependant velocity and pressure into an average velocity and pressure (Birk, 2019:82). This splitting and simplifying process also introduces an unknown variable called the Reynolds stress tensor. Turbulence models and equations are developed to solve for the unknowns.

As stated by Birk (2019:82), dividing the properties of the fluid flow into an averaged value and a turbulent fluctuation gives the following equations:

$$\begin{aligned}
 u(t) &= \bar{u}(t) + u'(t) \\
 v(t) &= \bar{v}(t) + v'(t) \\
 w(t) &= \bar{w}(t) + w'(t) \\
 \rho(t) &= \bar{\rho}(t) + \rho'(t) \\
 p(t) &= \bar{p}(t) + p'(t)
 \end{aligned} \tag{3.6}$$

Average values for any specific time range can be found by integrating the range over the time and dividing by the duration of the range. This is given by the following equation:

$$\bar{u} = \frac{1}{T} \int_0^T u(t) dt \tag{3.7}$$

Replacing the time dependant velocity in (3.2) by the sum of the average velocity and turbulence fluctuation in (3.6) gives the following equations for the average velocities (3.8), and the turbulent velocities (3.9).

$$\frac{\partial \bar{u}}{\partial x} + \frac{\partial \bar{v}}{\partial y} + \frac{\partial \bar{w}}{\partial z} = 0 \tag{3.8}$$

$$\frac{\partial \bar{u}'}{\partial x} + \frac{\partial \bar{v}'}{\partial y} + \frac{\partial \bar{w}'}{\partial z} = 0 \tag{3.9}$$

The RANS equations are given by (3.10).

$$\begin{aligned}
 \frac{\partial \bar{u}}{\partial t} + (\bar{\underline{v}}^T \underline{\nabla}) \bar{u} &= \bar{f}_x - \frac{1}{\rho} \frac{\partial \bar{p}}{\partial x} + \nu \Delta \bar{u} - \left[\frac{\partial}{\partial x} \overline{(u'u')} + \frac{\partial}{\partial y} \overline{(v'u')} + \frac{\partial}{\partial z} \overline{(w'u')} \right] \\
 \frac{\partial \bar{v}}{\partial t} + (\bar{\underline{v}}^T \underline{\nabla}) \bar{v} &= \bar{f}_y - \frac{1}{\rho} \frac{\partial \bar{p}}{\partial y} + \nu \Delta \bar{v} - \left[\frac{\partial}{\partial x} \overline{(u'v')} + \frac{\partial}{\partial y} \overline{(v'v')} + \frac{\partial}{\partial z} \overline{(w'v')} \right] \\
 \frac{\partial \bar{w}}{\partial t} + (\bar{\underline{v}}^T \underline{\nabla}) \bar{w} &= \bar{f}_z - \frac{1}{\rho} \frac{\partial \bar{p}}{\partial z} + \nu \Delta \bar{w} - \left[\frac{\partial}{\partial x} \overline{(u'w')} + \frac{\partial}{\partial y} \overline{(v'w')} + \frac{\partial}{\partial z} \overline{(w'w')} \right]
 \end{aligned} \tag{3.10}$$

Where ν is the kinematic viscosity, and $\underline{\bar{f}}$ is the vector body force.

3.3.3 Turbulence modelling

The averaged methodology used to develop the RANS equations results in the creation of six new unknown variables. These unknown variables are the turbulent velocity products $\overline{(u'u')}$, $\overline{(v'u')}$, $\overline{(w'u')}$, $\overline{(v'v')}$, $\overline{(w'v')}$, and $\overline{(w'w')}$.

These unknowns are called the Reynolds stresses, and can be collected into a term called the Reynolds stress tensor $\underline{\underline{\tau}}$ (Birk, 2019:89).

$$\underline{\underline{\tau}} = \begin{pmatrix} \tau'_{xx} & \tau'_{yx} & \tau'_{zx} \\ \tau'_{xy} & \tau'_{yy} & \tau'_{zy} \\ \tau'_{xz} & \tau'_{yz} & \tau'_{zz} \end{pmatrix} = \begin{pmatrix} \overline{u'u'} & \overline{v'u'} & \overline{w'u'} \\ \overline{u'v'} & \overline{v'v'} & \overline{w'v'} \\ \overline{u'w'} & \overline{v'w'} & \overline{w'w'} \end{pmatrix} \quad (3.11)$$

The Reynolds stress tensor allows for equation (3.10) to be written in a vector form, given by equation (3.12) below.

$$\frac{\partial \underline{v}}{\partial t} + (\underline{v} \nabla) \underline{v} = \underline{f} - \frac{1}{\rho} \nabla p + \nu \Delta \underline{v} + \frac{1}{\rho} (\nabla^T \underline{\underline{\tau}})^T \quad (3.12)$$

Turbulence models create additional equations to solve for the unknowns that have been created. Two of the most widely used turbulence models are the $k-\varepsilon$ and the Reynolds stress model (Versteeg & Malalasekera, 2007:65-66). These turbulence models predict the scalar transport terms, and the Reynolds stresses to close the system of equations (3.8), (3.9), (3.10), and (3.12) (Versteeg & Malalasekera, 2007:66).

RANS turbulence models are ranked according to the number of additional transport equations that are required to be solved together with the RANS equations (Versteeg & Malalasekera, 2007:66). Table 6 below shows the various turbulence models and the amount of extra transport equations they require.

Table 6. Number of additional transport equations needed for each turbulence model, redrawn from (Versteeg & Malalasekera, 2007:67).

No. of extra transport equations	Turbulence model
0	Mixing length
1	Spalart-Allmaras
2	$k-\varepsilon$
2	$k-\omega$
2	Algebraic stress
7	Reynolds stress

The computing power required to achieve a fairly accurate result using these models is relatively low, particularly for the mixing length and $k-\varepsilon$ models, hence their popularity in being used for CFD work in industry today.

3.3.4 Turbulent viscosity and turbulent diffusivity

The two most commonly used turbulence models in industry are the mixing length and the $k-\varepsilon$ models. The common assumption of both models is that there is a relationship between the Reynolds stresses and the action of the viscous stresses on the average flow (Versteeg & Malalasekera, 2007:67).

In other words, the rate of deformation of individual fluid elements are directly proportional to the viscous stresses within the fluid. This is shown in equation (3.13) below, for an incompressible fluid.

$$\tau_{ij} = \mu_{ij} = \mu \left(\frac{\partial u_i}{\partial x_j} + \frac{\partial u_j}{\partial x_i} \right) \quad (3.13)$$

Where the suffix i or j corresponds to Cartesian directions. For example i or $j = 1$ corresponds to the x -direction, i or $j = 2$ corresponds to the y -direction, and i or $j = 3$ corresponds to the z -direction (Versteeg & Malalasekera, 2007:67).

Experimental evidence has shown that turbulence decays in the absence of shear stress, and that turbulent stresses are proportional to the rate of deformation (Versteeg & Malalasekera, 2007:67). From this, we get equation (3.14), which further defines the relationship between the Reynolds stresses and the average rates of deformation of the fluid.

$$\tau_{ij} = -\overline{\rho u'_i u'_j} = \mu_i \left(\frac{\partial U_i}{\partial x_j} + \frac{\partial U_j}{\partial x_i} \right) - \frac{2}{3} \rho k \delta_{ij} \quad (3.14)$$

Where $k = \frac{1}{2} (\overline{u'^2} + \overline{v'^2} + \overline{w'^2})$ is the turbulent kinetic energy per unit mass, μ_i is the turbulent or eddy viscosity, and δ_{ij} is the Kronecker delta (Versteeg & Malalasekera, 2007:67).

From (7.14), the assumption which can be made is that the average gradients of momentum per unit mass is proportional to the turbulent momentum transport. In other words the turbulent transport of a scalar property of the fluid can be assumed to be proportional to the gradient of the average value of the transported quantity (Versteeg & Malalasekera, 2007:68). From this, equation (3.15) is developed.

$$-\overline{\rho u'_i \varphi'} = \Gamma_t \frac{\partial \Phi}{\partial x_i} \quad (3.15)$$

Where Γ_t is the turbulent or eddy diffusivity, φ' is the time varying fluctuating component of the flow, and Φ is steady mean component of the flow.

The turbulent momentum transport, turbulent heat transport and turbulent mass transport are due to the same eddy mixing mechanism. Thus, the eddy diffusivity Γ_t can be assumed to be close in value to the turbulent viscosity μ_t .

This assumption is called the Reynolds analogy (Versteeg & Malalasekera, 2007:68).

The ratio between Γ_t and μ_t is called the Prandtl/Schmidt number given by the equation (3.16) below.

$$\sigma_t = \frac{\mu_t}{\Gamma_t} \quad (3.16)$$

Most CFD packages used in industry assume that this ratio is nearly constant, and assign a value close to unity for σ_t .

The assumption that this number remains nearly constant is based on numerous experiments investigating flows.

It is clear that turbulent stresses and levels change from point to point within a turbulent flow. The mixing length and $k-\varepsilon$ models attempt to describe these turbulent stresses.

The mixing length model does this by simpler algebra for the turbulent viscosity as a function of position. The $k-\varepsilon$ model however is more complex in the manner in which it attempts to describe the turbulent stresses. It describes turbulence by allowing for the effects of transport on turbulence properties by diffusion and convection, and for the generation and destruction of turbulence (Versteeg & Malalasekera, 2007:68).

3.3.5 The $k-\varepsilon$ turbulence model

In the $k-\varepsilon$ model two transport equations are solved. These two are for the turbulent kinetic energy and the rate of dissipation of the turbulent kinetic energy (Versteeg & Malalasekera, 2007:68).

The equation for the turbulent kinetic energy k , is given by equation (3.17) below.

$$\frac{\partial(\rho k)}{\partial t} + \text{div}(\rho k \mathbf{U}) = \text{div} \left(-\overline{p' \mathbf{u}'} + 2\mu \overline{\mathbf{u}' s'_{ij}} - \rho \frac{1}{2} \overline{u'_i u'_i u'_j} \right) - 2\mu \overline{s'_{ij} \cdot s'_{ij}} - \overline{\rho u'_i u'_j} \cdot S_{ij} \quad (3.17)$$

Where \mathbf{U} is the mean flow, \mathbf{u}' is the fluctuating component of the flow, S_{ij} is the mean rate of deformation of a fluid element, and s'_{ij} is the fluctuating rate of deformation of a fluid element

With regards to the left hand side of equation (3.17), the first term is the rate of change of turbulent kinetic energy, and the second term is the transport of turbulent kinetic energy by convection.

With regards to the right hand side of equation (3.17), the first term is the transport of the turbulent kinetic energy by pressure. The second term is the transport of turbulent kinetic energy by viscous stresses. The third term is the transport of turbulent kinetic energy by Reynolds stress. The fourth term is the rate of dissipation of turbulent kinetic energy. Lastly, the fifth term is the rate of production of turbulent kinetic energy.

The standard $k-\varepsilon$ model uses (3.18) and (3.19) as the transport equations for k and ε respectively (Versteeg & Malalasekera, 2007:75).

$$\frac{\partial(\rho k)}{\partial t} + \text{div}(\rho k \mathbf{U}) = \text{div} \left[\frac{\mu_t}{\sigma_k} \text{grad } k \right] + 2\mu_t S_{ij} \cdot S_{ij} - \rho \varepsilon \quad (3.18)$$

$$\frac{\partial(\rho\varepsilon)}{\partial t} + \text{div}(\rho\varepsilon\mathbf{U}) = \text{div}\left[\frac{\mu_t}{\sigma_\varepsilon}\text{grad } \varepsilon\right] + C_{1\varepsilon}\frac{\varepsilon}{k}2\mu_t S_{ij}\cdot S_{ij} - C_{2\varepsilon}\rho\frac{\varepsilon^2}{k} \quad (3.19)$$

Where $C_{1\varepsilon}$ and $C_{2\varepsilon}$ are dimensionless constants of proportionality.

Some of the advantages of the standard $k-\varepsilon$ model are:

- It is the most simple turbulence model where only boundary or/and initial conditions are required (Versteeg & Malalasekera, 2007:80).
- From all the various turbulence models available commercially, it is the most validated model.
- It requires relatively low computing power.
- It has high performance with regards to separation and boundary layers.

Some of the disadvantages of the standard $k-\varepsilon$ model are:

- It may predict excessive separation in flows, which requires a higher degree of mesh resolution at the vehicle surface to curb.
- Flows with large rotations are not dealt with well.
- Compared to the mixing length model, it is more demanding on computing power.

Chapter 4

Experimental methods and design

4.1 BET drivetrain components

There are various electric motors that have been used in vehicles over the decades. Some of the motors which are used are:

- Induction motors (IM).
- Direct current motors (DC).
- Switched reluctance motors (SRM).
- Permanent magnet synchronous motors (PMSM).

An electric motor used in a vehicle application, has the following general requirements:

- High power to size ratio.
- Constant power delivery across the speed range.
- High torque delivery at low speeds.
- High efficiency.
- High controllability.
- It is reliable and robust.
- Low electromagnetic interference (EMI) noise generation.
- Relatively low cost.

In general, EV drivetrains consist of sub-systems which act to convert the electrical energy within a battery system into mechanical torque which then drive the wheels (Arora et al., 2021:39).

The components which make up the sub-systems are:

- Electric motor.
- Transmission.
- Motor controller.
- Battery.
- Inverter.

To determine the drivetrain configuration for a BET, first the performance requirements of a BET need to be defined. Some of these requirements are listed below:

- Be able to start from standstill and maintain acceleration through varying road inclinations (Arora et al., 2021:39).

- Be able to perform stops and starts.
- High overall efficiency.
- Adequate supply of electrical energy to perform a given route.
- Relatively low mass and cost.

While electric motors themselves are greatly more efficient than diesel ICEs, the power and torque they generate has to be delivered via transmissions and differentials. Through these transmissions and differentials, losses are generated that reduce the overall drivetrain efficiency.

The system level drivetrain efficiency of an EV in city traffic conditions is near 60% (Arora et al., 2021:39).

4.2 BET drivetrain configuration

Heavy-duty BEVs can have their drivetrains configured in a multitude of ways; according to Arora et al (2021), the three configurations below are the most common.

4.2.1 Configuration 1

A central electric motor, a single ratio transmission, and a differential. This configuration is shown in Figure 41 below, it is the most common configuration used in electric trucks (Arora et al., 2021:39). The electric motor provides the torque which is converted by a single ratio transmission and differential, which is then used to drive the wheels.

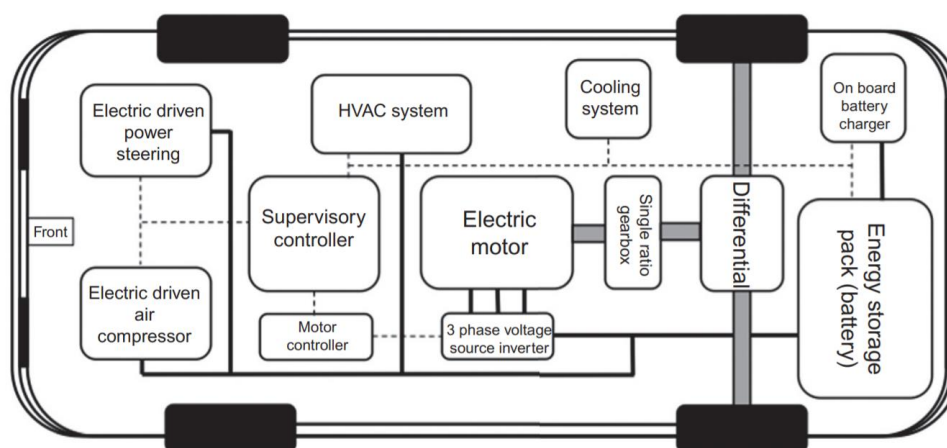


Figure 41. Central motor + single ratio reduction transmission + differential (Arora et al., 2021:40).

4.2.2 Configuration 2

A central electric motor, a multiple ratio transmission mated to a differential. Compared to configuration 1, this configuration has a multiple ratio transmission. The advantage of multiple gear ratios is that the maximum required torque for the electric motor is lower. This usually means the cost and size of the electric motor required is reduced. The multiple ratio transmission does add cost into the system in terms of the added control system required for it. Figure 42 shows this EV drivetrain configuration.

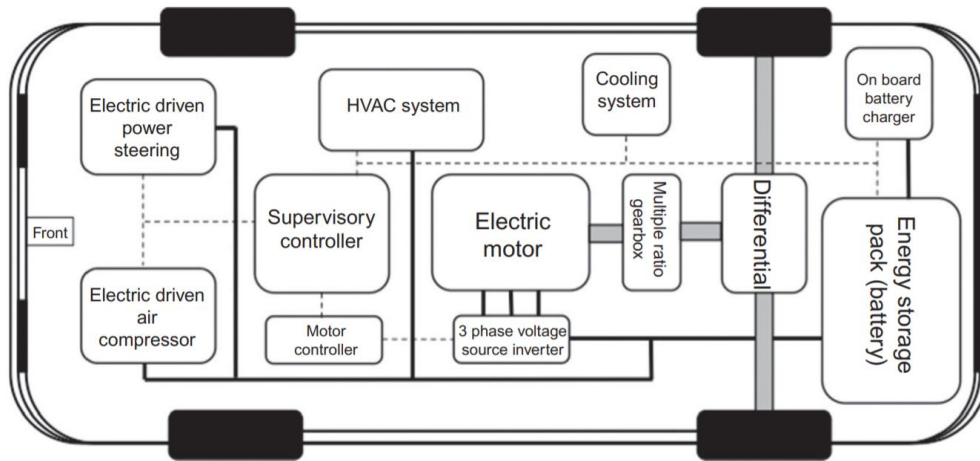


Figure 42. Central motor + multiple ratio transmission + differential (Arora et al., 2021:40).

4.2.3 Configuration 3

Two in wheel electric motors and a single ratio transmission for each motor. The required power from each motor for this configuration is lower when compared to the previous configurations. This is due to each of the drive wheels being powered independently. As with configuration 2, additional control systems are needed for synchronising both motors (Arora et al., 2021:41). Figure 43 below shows this configuration.

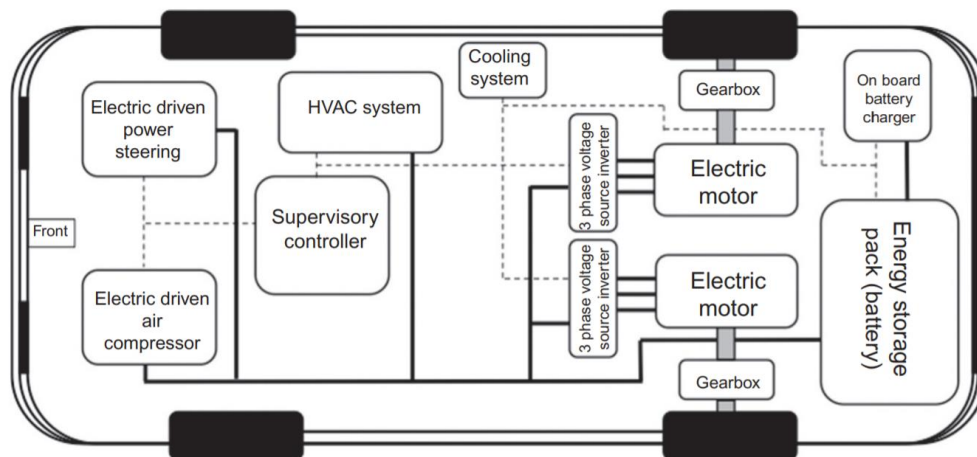


Figure 43. Two by-wheel or hub motors + single ratio transmission (Arora et al., 2021:41).

The selection of BET drivetrain components is dependent on the performance requirements for such a vehicle. BETs require battery packs that have a relatively high energy density, which is needed to ensure sufficient electrical energy to complete the mileage for a given travel route. BETs also require electric motors with very high torque at low speeds to ensure that the drivetrain can overcome the large inertia of the fully loaded truck.

4.3 BET drivetrain features

According to Arora et al (2021:42), other factors which are important for a BET drivetrain are:

Powertrain efficiency: The overall efficiency of the powertrain, as well as the individual efficiency of all the sub-components which are a part of the powertrain.

Modularity: This is the interchangeability and independence of the components. Being modular allows the BET to receive future upgrades and modifications in an almost plug-and-play manner.

Drivetrain control: In general, the smaller the amount of control systems, the simpler the system development and the lower the cost.

Ease of servicing: This is the simplicity with which maintenance can be done on subsystems.

Low mass and volume: Lower mass means a lower energy demand on the drivetrain. Smaller components are also easier to fit during assembly and maintenance.

Low vibration: Vibrations cause losses and decrease the overall efficiency of the drivetrain. Vibrations also cause accelerated wear on components.

Low cost: Cost is an important factor in any project. Low lead time components are also an important factor, as is the future serial production of components and spare components.

Safety and durability: With the high voltages used in BETs, it is critical that the BET can operate in a fail safe manner as well as conform to all relevant safety regulations.

Compliance: All components and subsystems must conform to existing international standards for EVs.

4.4 Evaluation of BET drivetrain configurations

The following numeric values are assigned to evaluate each drivetrain feature:

1. Very poor
2. Poor
3. Normal
4. Good
5. Very good

The features mentioned in 4.3 can be further categorized in terms of their importance to the drivetrain. Table 7 below shows the categorisation of the features in terms of their priority (Arora et al., 2021:44-45). When evaluated, the highest priority features will be multiplied by a factor of three, the moderate priority features will be multiplied by a factor of two, and the lowest priority features will be multiplied by a factor of one. This multiplication by the given factor is to emphasise the importance of each feature to the overall drivetrain configuration. This can be seen later in Table 8.

Table 7. Categorisation of drivetrain features in terms of overall drivetrain priority.

Highest priority	Moderate priority	Lowest priority
Efficiency	Ease of servicing	Low acoustic noise
Modularity	Safety and durability	Low vibration
Low mass/volume	Compliance	
Low cost		
Low servicing time		
Control simplicity		

As stated previously, torque conversion reduces the overall efficiency. As such, motors connected directly to a differential will have the highest efficiency. However, this configuration results in very poor performance for vehicles with large inertias like BETs.

All three configurations require an electric motor which has relatively low torque and high speeds. This attribute makes all three concepts quite modular since these types of motors are manufactured by many companies in the EV market (Arora et al., 2021:45).

An advantage of configuration 4 is that should one of the electric motors fail, the BET could still continue until reaching a serviceable stop.

Table 8 shows a comparison of the three drivetrain configurations.

From the table, it is clear that configuration 3 is the most suitable configuration for a BET drivetrain. Configuration 3 has also been found to be optimal by another system level analysis of an electric truck (Verbruggen et al., 2020).

Table 8. Comparison of drivetrain configurations, redrawn from Arora et al. (2021:47).

Criteria	Configuration 1		Configuration 2		Configuration 3	
Highest priority		X3		X3		X3
High efficiency	3	9	2	6	3	9
Modularity	4	12	4	12	5	15
Low mass/volume	3	9	3	9	4	12
Low drivetrain cost	3	9	2	6	3	9
Low servicing time	3	9	2	6	4	12
Control simplicity	3	9	2	6	3	9
Moderate priority		X2		X2		X2
Ease of servicing	3	6	3	6	3	6
Safety and durability	5	10	2	4	3	6
Compliance	4	8	5	10	3	6
Lowest priority		X1		X1		X1
Low acoustic noise	2	2	2	2	4	4
Low vibration	2	2	1	1	4	4
Overall score		85		68		92

There are many manufacturers who have already put into serial production the type of electric drive axle specified by configuration 3. ZF and Dana are examples of companies which have done this (Arora et al., 2021:48).

4.5 Autonomous BET power consumption

For an autonomous BET, many auxiliary systems normally found in conventional EVs are absent because the autonomous BET does not have a driver. Some of these redundant systems are the Heating, Ventilation, and Air Conditioning (HVAC) system, the driver instrumentation binnacle, safety systems for the driver, windscreen wiper and washing, electro-hydraulic steering wheel system, and audio/video entertainment.

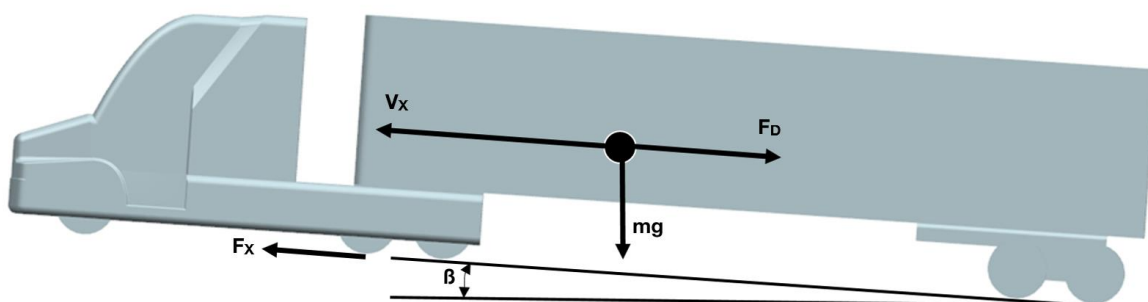


Figure 44. Heavy-duty truck on a slope and applied forces.

With reference to Figure 44, Verbruggen et al (2020:9) describes the tractive force of the truck at any moment in time by equation (4.1) below, which takes rolling friction, aerodynamic drag and the resistance from the incline of the road into account.

$$F_x(t) = m \frac{dv}{dt} + \frac{1}{2} \rho C_D A_f v(t)^2 + mg C_{rr} \cos(\beta(t)) + mg \sin(\beta(t)) \quad (4.1)$$

Where F_x is the tractive force, C_{rr} is the coefficient of rolling resistance, A_f is the frontal area, β is the road gradient, and m is the truck mass.

Further to this, the torque required at the wheels is given by Verbruggen et al (2020:9) in equation (4.2) below.

$$\tau_w(t) = F_x(t) r_w \quad (4.2)$$

Where τ_w is the torque requirement at the wheels, and r_w is the radius of the wheel.

4.6 Electric motor drives

The complexities of an electric motor used in an EV system will not be described here but its brief descriptions will be given. Although many studies considered the comparison between electric motor drives in conventional passenger EVs, there are few studies which compare the performance of electric motors in heavy-duty EVs such as a BET.

In principle an electric drive is a power converting unit, containing an inverter drive and an electric motor (Arora et al., 2021:49). The inverter drive converts direct electric current power into alternating current power. This creates a torque on the rotor of the electric motor. In some applications this power conversion can be reversed, thereby allowing the motor to effectively act as a generator which can recover kinetic energy and supply this energy back into the battery pack, effectively charging it.

Within an electrical motor are the rotor and the stator. The inverter of the electric drive controls the stator, which has windings which conduct electrical current. The current through these windings create a magnetic field which causes the rotor to spin. The axis of revolution of rotor and the stator are concentric to each other.

In EV applications, the electric motor which is most used is the radial flux type. In this type of motor, as the name suggests, the magnetic field flows radially around the stator-rotor configuration (Arora et al., 2021:50). Figure 45 below shows a sectioned view of a radial-flux electric motor.

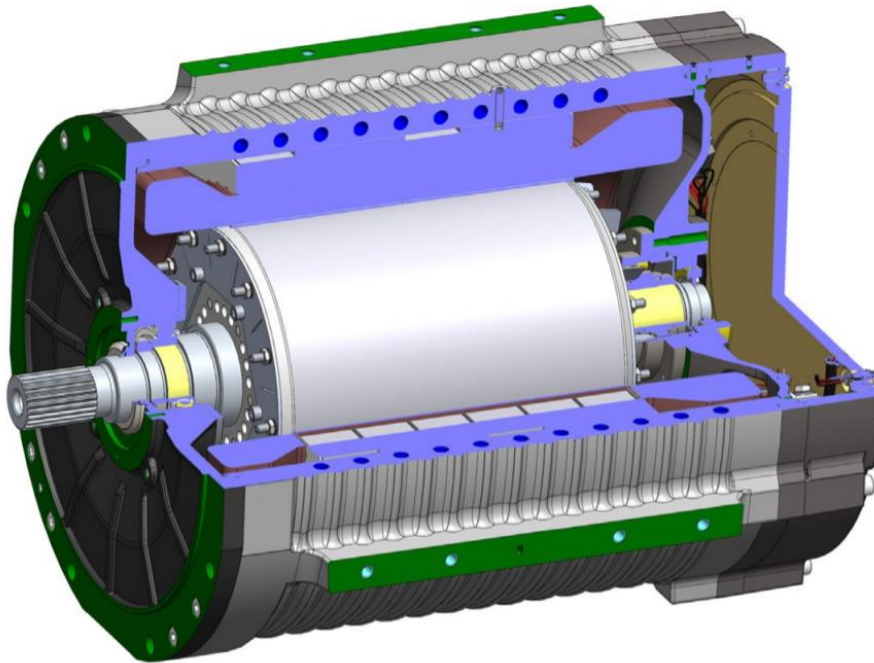


Figure 45. CAD model of a radial-flux electric motor (Arora et al., 2021:51).

Permanent magnet synchronous motors (PMSMs) are one of the most common motor types used in the EV industry (Arora et al., 2021:52). PMSMs are more efficient than other types of electric motors with respect to the amount of torque they can generate at higher rotation speeds.

The attributes of a PMSM are high power/size ratio, high efficiency, and quick torque response. These attributes make them particularly useful in EVs, and have resulted in their being the most common motor type in the EV industry (Tashakori et al., 2011).

Essentially, the primary task of the inverter is to convert direct current to alternating current. A particular requirement for EV inverters is that they need to accurately control the torque of the motor at low speeds.

4.6.1 Electric motor and inverter selection

Verbruggen et al (2020:15-17) have found the optimal peak power required by the electric motors of a heavy-duty truck to be approximately 410kW. Mareev et al (2018:6) found this figure to be 376kW. For the purposes of this research, and again being conservative, the figure of 410kW will be used for the electric motor system peak power requirement.

In terms of the type of electric motor which best suits the requirements of a long-haul BET, the PMSM type has been found to be optimal (Morozov et al., 2018:31; Wolff et al., 2021:3; Verbruggen et al., 2020:11).

The most common electric motor manufacturer cited in the literature is Dana. Browsing their extensive range of electric motors for various vehicle applications, the

TM4 SUMO HP range was found to be most suitable. This electric motor range is designed for class-8 heavy-duty vehicles in mind. The specific model selected for use in this research is the HV1000-3P (traction) motor (Dana TM4, 2021). The HV1000-3P has a peak power output of 205kW and a peak torque output of 1000Nm. As per configuration 3 in section 4.2.3, two of these motors are required which brings the peak power and torque figures to 410kW and 2000Nm respectively.

The basic exterior dimensions of the motor are shown in Figure 46 below. These dimensions will be used when creating the basic topology of the drivetrain.

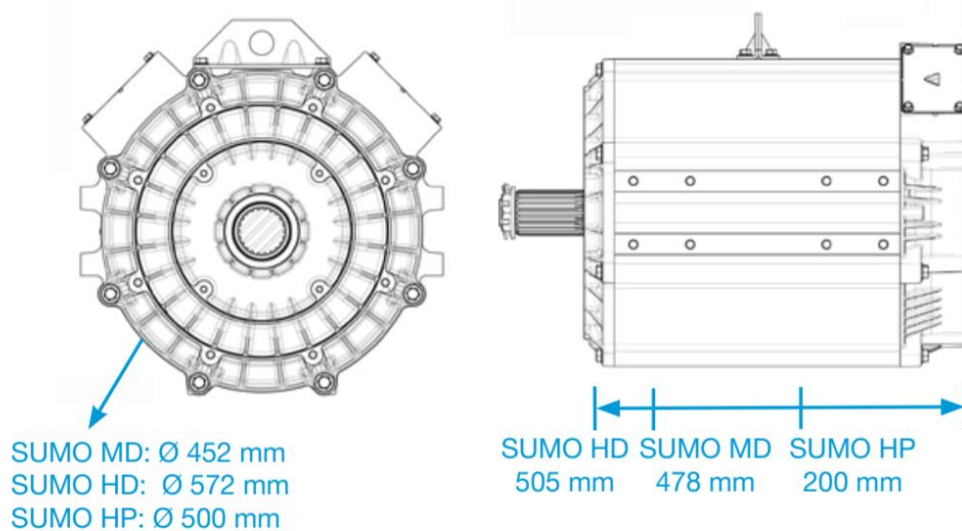


Figure 46. The basic dimensions of the DANA TM4 SUMO range of electric motors (Dana TM4, 2021).

The manufacturer suggests the motor be coupled to a specific inverter, namely, the DANA TM4 CO150 inverter (Dana TM4, 2021). This inverter is shown in Figure 47 below and will also be 3D modelled for use in the overall drivetrain topology.

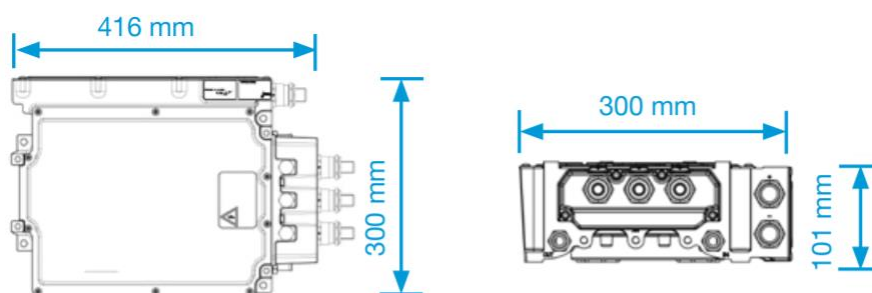


Figure 47. The basic dimensions of the DANA TM4 CO150 inverter (Dana TM4, 2021).

4.7 BET battery requirements

As discussed in chapter 2.8, Li-Ion batteries represent the optimal currently commercially available solution for energy source in BETs. Within this type of battery, lithium iron phosphate (LFP) chemistry benefits from excellent thermal stability and low resistance, which provides excellent safety. LFP batteries also have a long cycle life, are durable and have a low manufacturing cost (Campagnol et al., 2021; National Academies of Sciences and Medicine, 2020:250; Feng & Dong, 2020).

Verbruggen et al. (2020:15) have found that for heavy-duty electric trucks, the optimal battery capacity falls into the range 221kWh to 210kWh. It should be noted that their research was based on a conventional electric heavy-duty truck, simulated on a conventional long-haul European drive cycle. As such, this battery specification is based on a truck which needs a driver and the associated auxiliary power demands of such a configuration.

Verbruggen et al (2020:13) used a value of 4.86kW for this auxiliary power requirement. In an autonomous BET none of these auxiliary systems are required as there is no driver in the vehicle, therefore the overall power required is reduced by 4.86kW for an autonomous BET.

Estimates for the power consumption of an autonomous system range between 1-4kW (Ramey, 2017; Dunietz, 2018). For the purpose of this research, the figure of 221kWh will be used for the battery energy requirement. This is a conservative figure when considering the lack of auxiliary systems and cab structure in an autonomous BET, as well as advances in battery energy density and computing power which would be available in the coming decades when such a vehicle may become commercialised.

4.7.1 Battery selection

The largest LFP manufacturer in the world is BYD Auto, a Chinese auto manufacturer. At the time of writing, BYD had no commercial LFP battery pack data or specifications available for viewing to select for an autonomous BET application. In the USA and Europe one of the largest battery manufacturers is Proterra, which is predominantly an electric bus manufacturer. Proterra also manufactures and supplies class-8 heavy-duty electric truck battery packs.

Reading through their product literature, the S Series battery pack meets the requirements of a minimum energy requirement of 221kWh. Added to meeting this basic performance requirement, the battery pack also has the following benefits, as stated by the manufacturer (Proterra, 2021).

- Industry leading energy density
- Customizable/modular design can be expanded lengthwise
- Liquid cooled
- Multi-layered passive and safety standards
- International safety standard compliance
- Environmental durability testing exceeds 12 years of operation

The S Series battery pack can be seen in Figure 48 below:

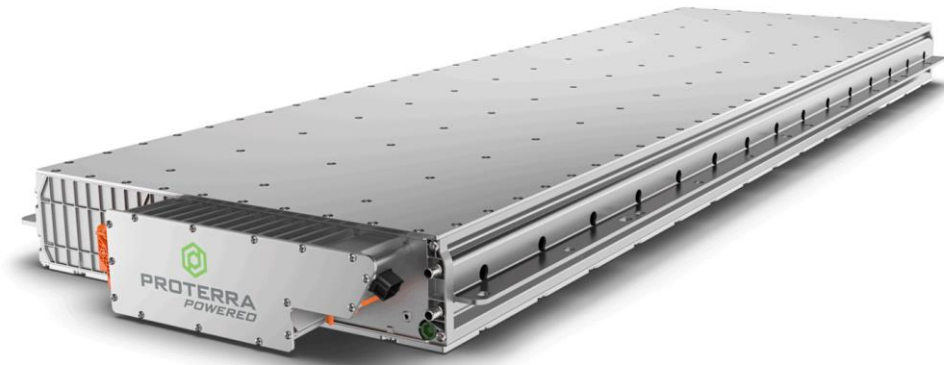


Figure 48. A Proterra S Series battery pack (Proterra, 2021).

A single S Series battery pack has 125kWh of energy storage, hence for this autonomous BET concept two battery packs will be required which amounts to a total energy store of 250kWh. This figure is well above the 221kWh requirement.

Proterra (2021) specify the exterior dimensions of each pack is as follows:

- Length: 2802mm (This is the maximum scaled up length for 125kWh)
- Width: 175mm
- Height: 860mm

The battery pack can be installed in the horizontal or vertical position.

A common battery topology in electric trucks is to have the battery packs arranged symmetrically along the length of the chassis, as seen in Figure 49 below, which shows the EFORCE electric truck.

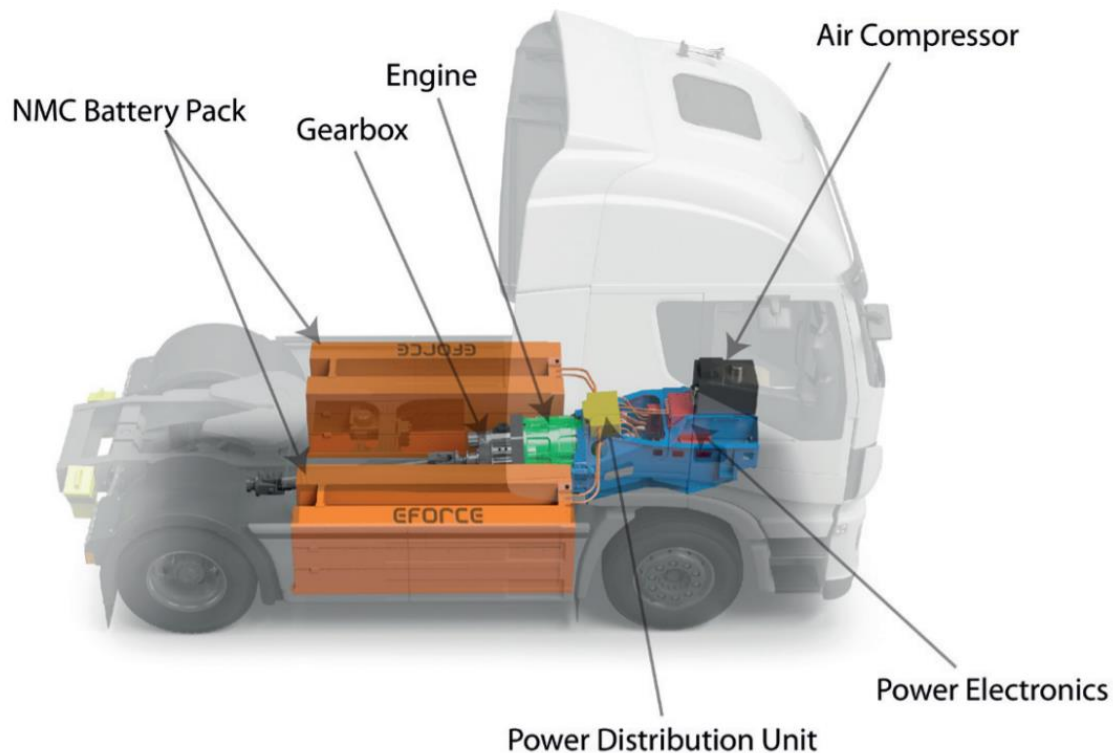


Figure 49. The placement of the battery packs in a conventional BET (E force, 2020).

4.8 Transmission

Unlike conventional ICE trucks which normally have 18 speed transmissions, BETs make use of just two to four speeds. The reason for this is that unlike diesel ICEs, electric motors have very wide peak torque ranges and with a torque band that operates at much higher revolutions per minute (RPMs). Another benefit of electric motors compared to diesel ICEs is that an electric motor can easily operate at very low RPMs whereas ICEs have a minimum idle speed. The consequence of having this minimum idle speed is that ICE trucks need to have torque converters added to the drivetrain to enable pull off from standstill. An electric drivetrain does not need a torque converter or clutch system.

Transmissions for EVs also do not need to have a separate reverse gear since the electric motor can just spin in the opposite direction.

Configuration 3 in section 4.2.3 has a transmission allocated to each electric motor. Work done by Verbruggen et al (2020:18) suggests that a multi-speed transmission for a heavy-duty truck is the optimal solution when total cost of ownership is considered.

Eaton, Spicer, and Cummins are three of the largest EV transmission manufacturers. Browsing their product range for an applicable transmission which can handle the peak power and peak torque outputs of the electric motor led to the selection of the Eaton 4-speed EV transmission (Eaton, 2021).

The basic specifications for this transmission can be seen in Table 9 below.

Table 9. Eaton 4-speed EV transmission specifications, redrawn from (Eaton, 2021).

Architecture	EV and PHEV
Total length	420 mm
Total mass	109 kg
Maximum torque capacity	1200 Nm
Maximum input speed	5000 rpm
Maximum gross vehicle weight rating	18 tons

The transmission can be seen in Figure 50 below.



Figure 50. Eaton 4-speed EV transmission (Eaton, 2021).

At the time of writing, further advancements in EV transmission technology are close to being commercialised. Mazaro is working on what it calls a Single Stage Variable Transmission (SVT) for heavy-duty EVs. An SVT allows the electric motor to stay within its best efficiency curve for a longer period of the drive cycle (Mazaro, n.d.). The technology promises to deliver an 11% cost saving and a 25% mass reduction over conventional EV transmissions (Megan Lampinen, 2021).

4.9 Autonomous systems

Autonomous systems contain an array of sensors and power electronics as described in section 2.10. These systems are not the major components in terms of physical size compared to those described in sections 4.6, 4.7, and 4.8. For this reason, a thorough individual component selection will not be done for the autonomous system of a BET. This is because the general overall BET topology is not constrained by the physical size of the autonomous components.

As with battery technology, autonomous sensor technology is an ever evolving area. It is reasonable to see further reductions in sensor size and energy consumption in the coming decades when an autonomous BET may come to market.

For the purposes of this research the individual sensors used for autonomous driving were not 3D modelled as they were not expected to be a limiting factor in terms of exterior vehicle design.

Modern BET manufacturers have integrated the sensors for autonomous driving into the bodywork of the vehicle. The result is a flowing exterior shape without the need for abrupt changes in geometry to accommodate sensors for autonomous driving.

Two examples of such design can be seen in Figure 51 and Figure 52 below.



Figure 51. The Mercedes-Benz Future Truck (Evans, 2014).



Figure 52. The Tesla Semi (Hill, 2021).

4.10 Technology roadmap

Unlike the decades which have passed, current and future expectations of passenger EVs and BETs is that they should perform as well as, if not exceed the performance of conventional ICE vehicles and hybrid vehicles. The technological, financial, and institutional barriers to meet this expectation are being tackled headlong by private companies, universities, and governments. Some of these barriers are described in this section.

4.10.1 Electric motor development

Unlike the radial flux motors described in section 4.6 and the motor selected in chapter 4.6.1, axial flux motors are in development which could improve drivetrain performance. An axial flux motor could produce more power than a radial flux motor of the same physical size. For EVs, component size and energy demand is a critical factor in extending driving range; for this reason, the superior power to size ratio of axial flux motors over radial flux motors make them of major interest for future EV development.

Electric motors are also being developed on a drive-cycle-specific basis, with a possible future situation where a transmission is not a requirement in the drivetrain system.

4.10.2 EV energy storage development

Perhaps the biggest improvement in EV technology will come from battery development. At present LFP batteries represent the optimal choice for heavy-duty EVs when total cost, safety, performance, durability and longevity are considered. LFP and other Li-Ion batteries currently have energy densities of approximately 250Wh/kg and cycle lives of approximately 4000 cycles. They are targeted to reach figures of 350Wh/kg and 5000 cycles and 500Wh/kg and 10000 cycles by 2025 and 2030 respectively (Arora et al., 2021:220).

Li-air batteries as mentioned in section 2.8, could produce an energy density near 11680Wh/kg (Arora et al., 2021:220).

These advancements in energy density and cycle life translate into the possibility of having much smaller physical size topology for an autonomous BET in the next three decades. A lighter battery pack would also result in lower energy demand for the vehicle which increases its driving range, and lower mass also reduces wear on the braking system and chassis structure.

4.10.3 Inverter drive development

Converting the electrical energy stored in the battery packs to mechanical energy to the wheels incurs losses across the vehicle speed range. The goal is to minimise these losses as much as possible. It is important that the inverter converts DC voltage from the battery pack into AC voltage for the motor with as little energy loss as possible.

Development is ongoing in creating inverters with silicon carbide (SiC) switching devices to achieve low losses (Arora et al., 2021:221).

At the time of writing, EV inverters have a power density of approximately 30kVA/L. This figure is targeted to reach 100kVA/L. Multiphase inverter topologies are also in development for high torque demand applications (Arora et al., 2021:221).

4.10.4 Policy barriers

Information regarding the infrastructure, safety, operational and technological requirements, as well as the societal impact of heavy-duty EVs has been noted as something that is lacking for policy decision makers.

Policy makers also have a lack of information on how to begin adoption of heavy-duty EVs in their cities or countries, combined with weak governmental coordination (Sclar et al., 2019:7).

4.10.5 Financial barriers

The operational costs of EVs are much lower than they are for conventional ICE vehicles; however, the initial cost of the vehicles is generally much higher than they are for conventional vehicles. This has historically been seen as the primary barrier to heavy-duty EV adoption in the global market.

Heavy-duty EVs are also a very new technology without the decades of proven on-road performance and reliability that conventional heavy-duty vehicles have. This attribute, of being fairly new, creates the perception in businesses that they present unknown risks (Arora et al., 2021:222).

An increase in EVs in the market brings with it an increase in the demand from the energy grid. Countries face the need to scale up their energy grids to accommodate an increase in EVs and heavy-duty EVs. This represents a significant financial investment. The positive aspects of low emissions from EVs would be countered by an expanding energy grid which depends on fossil fuels and non-renewable energy sources. For this reason, governments should make efforts to expand their energy grids with renewable energy sources.

4.10.6 Autonomous BET development

Autonomous trucking is expected to be a disruptive technology, dramatically changing operational cost, safety, and scale of the heavy-duty road freight industry. Autonomous BETs are expected to provide a 45% reduction in operating costs in the USA (Chottani, 2018).

With reductions in cost of this scale, it is of no surprise that research and design in this area is accelerating at a huge rate. Companies are already retrofitting heavy-duty trucks with autonomous driving sensors and performing road testing.

Tu Simple is an American company pushing forward with research and development of autonomous BETs. Their autonomous system has the ability to process large amounts of information and can execute 600 trillion operations per second. Their sensor fusion capability allows the system to “see” 1000m ahead of the truck, a value that is in the range of being three to four times further than the latest passenger vehicle autonomous system (Tu Simple, 2021).

The mainstream adoption of autonomous trucks is expected to be rolled out in four main stages, with each stage bringing a lowering of the operator’s total cost of ownership. These four stages can be seen in Figure 53 below.

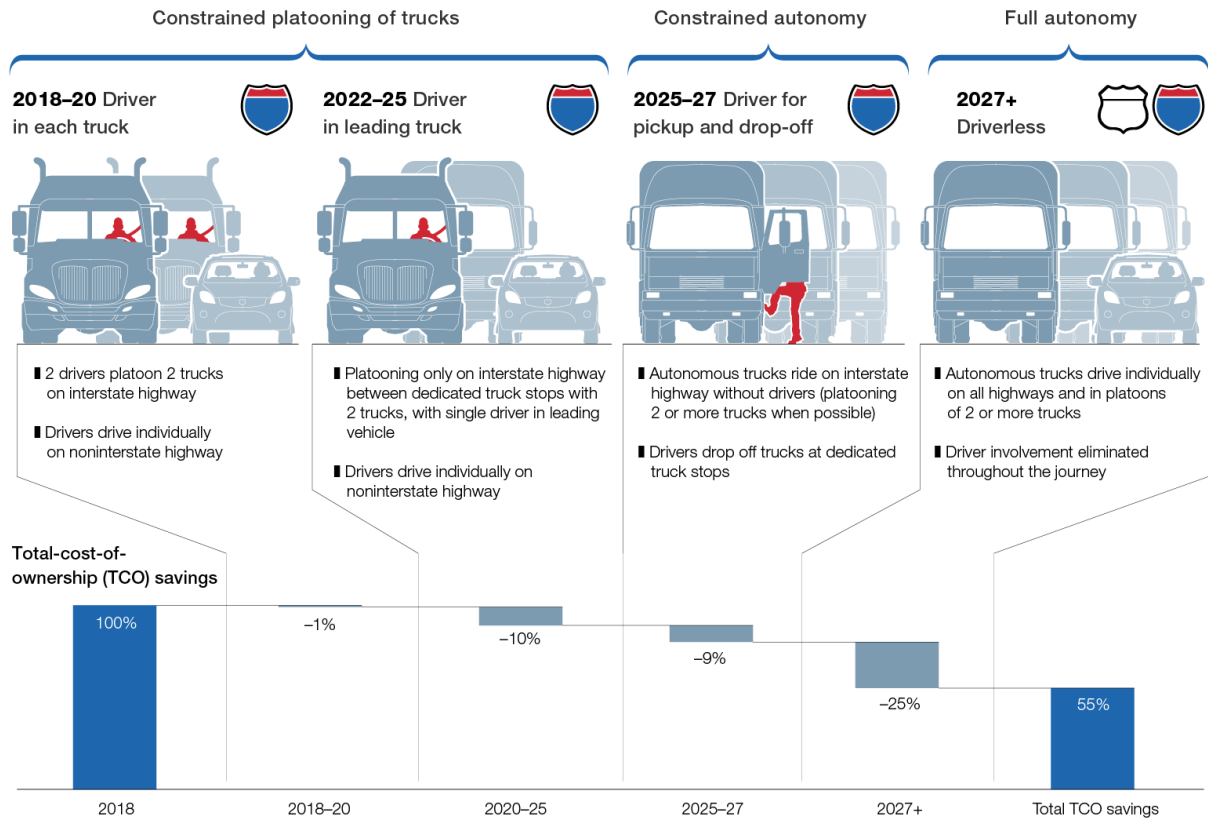


Figure 53. The possible roll out of autonomous BETs in the USA (Chottani, 2018).

Stage one will incorporate a technique called “platooning” which wirelessly connects a truck convoy. This allows them to follow closely behind each other, benefitting from lower aerodynamic drag and achieving greater fuel efficiency. These two stages require a driver to be present in the truck as a safety measure, and for the trucks themselves to be at the SAE autonomous driving level 3 (Chottani, 2018). This stage is expected to continue until the year 2022.

Stage two involves driverless platooning on highways. The lead truck will again have a safety driver with the following trucks being completely driverless. After leaving the highway, the driver takes full control of the truck (Chottani, 2018). This stage is expected to continue until the year 2025.

Stage three will correspond to the SAE level 4 for autonomous driving. In this stage the truck will be completely driverless, operating on specific routes without a following platoon. Drivers will pick up the trucks at highway exits and then drive them to their final destination. This stage is expected to reduce operating costs by 20% compared to traditional trucking with no autonomy (Chottani, 2018).

Stage four of the roll out is conservatively expected by the end of this decade. This stage will correspond to the SAE level 5 for autonomous driving, thus the truck will operate autonomously for every part of the journey, interacting with normal traffic and pedestrians.

With fully autonomous trucks on the road, all areas of business will need to shift to accommodate this change in transportation solutions. Some impacts on the value chain of the transportation sector are mentioned below.

- **Ports** – As deliveries increase in pace with operational costs being reduced, ports will need to increase operations accordingly. Shipping yards in some areas operate day shifts only, but with an autonomous BET they could stay open for all hours of the day.
- **Warehouses** – As with ports, warehouses could operate continuously with autonomous BETs eliminating the problem of finding truck drivers willing to work through the night. A faster turn-around of product shipping from warehouses has the effect of reducing the unit cost of warehousing a product. Investment in autonomous BET specific loading bays and pickup points will be needed on the part of the warehouses. More employees will likely be needed by warehouse operators to manage the increase in supply and delivery of goods in and out of the facility throughout the day and night.
- **Manufacturers** – The impact autonomous BETs will have on the supply chain is something shippers will need to adapt to. Especially the fact that autonomous BETs could work without interruption, without the need to observe national holidays and vacations as is the case with human drivers. Therefore, the time-based variations in supply chains will disappear. This aspect then drives production schedules for manufacturers operating factories, and production plans can be based around optimal efficiency instead of being planned around truck driver availability through the week, month, or year.

4.11 Truck size constraints

Current legislation on trucks constrain certain exterior dimensions, and hence the design envelope.

The maximum allowable width for a class 8 truck and trailer combination in the USA is 2.6m (Federal Highway Administration, 2004).

In the European Union the maximum width for a class 8 truck and trailer combination is also 2.6m (European Parliamentary Research Service, 2014).

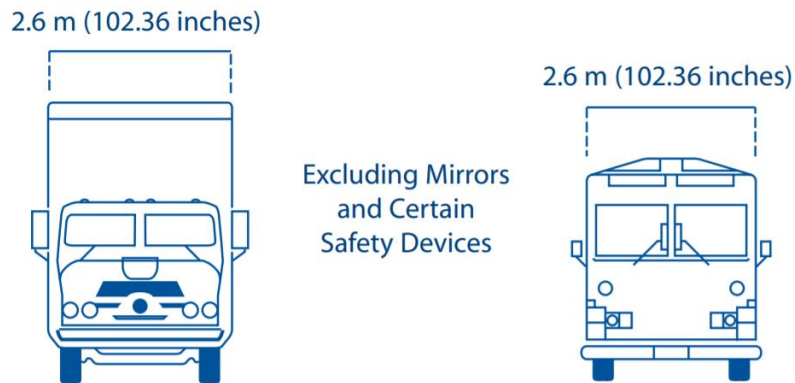


Figure 54. Class 8 truck width limit (Federal Highway Administration, 2004).

With reference to the configuration of truck and trailer show in Figure 55 below, the minimum length limit is 14.63m, with no overall length limit of the combination of the truck and trailer, or the distance between axles of the truck (Federal Highway Administration, 2004).

In the European Union the maximum length limit for the truck and tractor combination is 16.5m (European Parliamentary Research Service, 2014).

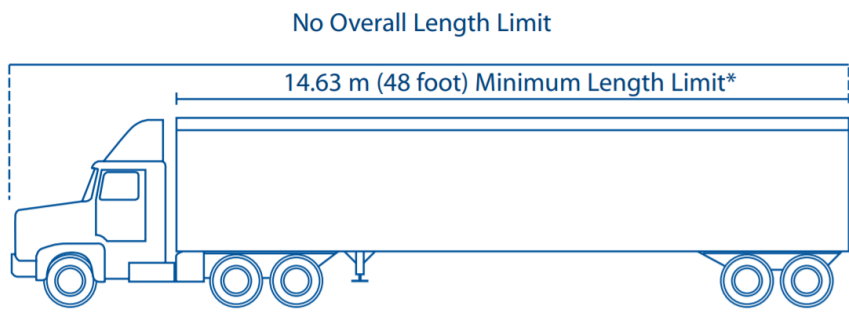


Figure 55. Class 8 truck length limits (Federal Highway Administration, 2004).

The maximum height for a truck trailer combination in the European Union is 4.0m (European Parliamentary Research Service, 2014).

Chapter 5

Numerical modelling

5.1 CFD Validation Model

The model used to validate the CFD setup and accuracy was the Generic Conventional Model (GCM). This is a simplified geometry used to represent a modern tractor-trailer model. The underbody of the tractor and the trailer in the GCM was simplified and approximated by flat surfaces (Storms et al., 2006:3). Based on experiments done by Satran (2004), the drag coefficient measured at a yaw angle of zero degrees was measured to be 0.397.

The GCM can be seen in Figure 56 below. The basic dimensions of the GCM are shown in Figure 57 and listed in Table 10 Below.

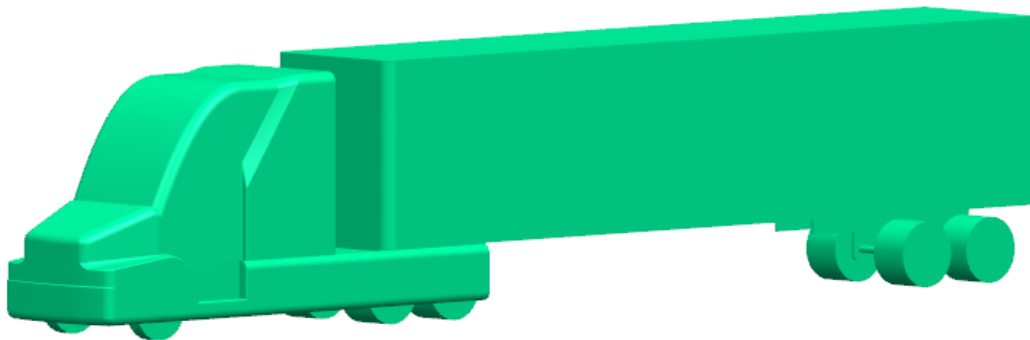


Figure 56. Generic Conventional Model (GCM).

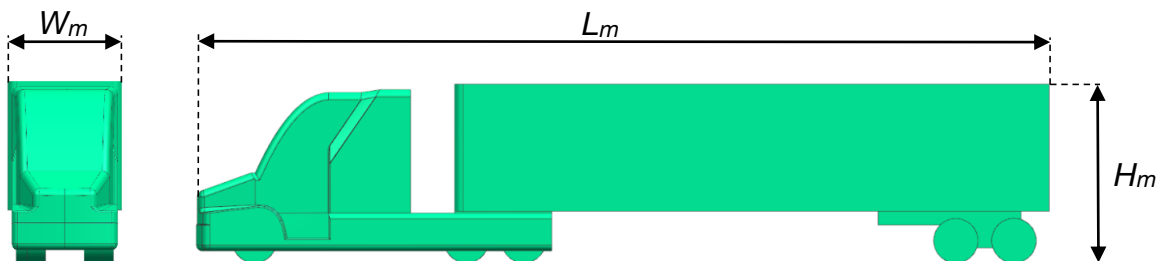


Figure 57. Basic dimensions of the GCM.

Table 10. Basic dimensions of the GCM.

Name	Symbol	Value (m)
Length of tractor-trailer	L_m	19.628
Width of tractor-trailer	W_m	2.591
Height of tractor-trailer	H_m	4.104

5.2 Computational domain

In terms of the size of the computational domain and the positioning of the GCM within the domain, Lanfrit (2005:2) recommends that the domain should extend three vehicle lengths in front of the GCM, and five vehicle lengths behind the GCM. Lanfrit (2005:2) also recommends that the GCM not displace more than 1.5% of the total cross-sectional area.

With these parameters taken into account, the CFD computational domain is shown in Figure 58, and its dimensions are listed in Table 11.

The GCM is a symmetrical model, and as such, the domain was symmetrical along the GCM longitudinal axis. This had the benefit of reducing the computational power demand and time by half. The available computing power limits the scope of this research to only consider flows without yaw.

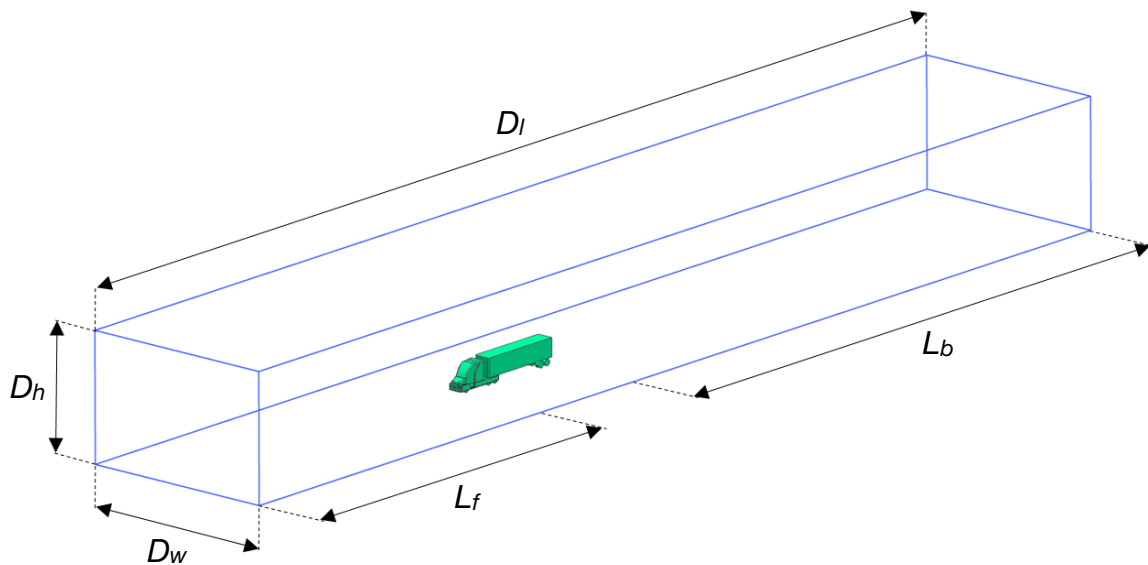


Figure 58. CFD computational domain.

Table 11. CFD computational domain dimensions.

Name	Symbol	Value (m)	
		Full-domain	Symmetrical-domain
<i>Domain length</i>	D_l	180	180
<i>Domain height</i>	D_h	20.1	20.1
<i>Domain width</i>	D_w	31.2	15.6
<i>Length in front of GCM</i>	L_f	60	60
<i>Length behind GCM</i>	L_b	100	100

5.3 Boundary conditions

For the purposes of the validation model, the floor of the domain was simulated as a stationary wall. This was done to replicate the conditions used in the real world experiment. The floor was simulated as a rolling road for all simulations after the validation. The floor was simulated to move in the direction and at the same speed as the incoming air flow. The reasons for having a simulated road are explained in section 2.5. The face of the domain where the air flow enters was modelled as a velocity inlet. The properties of the incoming flow, such as the speed magnitude, airflow direction and turbulence were specified at this velocity inlet plane. The domain exit was modelled as a pressure outlet, with a pressure equal to atmospheric pressure. The turbulence properties could also be set for this plane. The longitudinal symmetry plane was modelled with a symmetry boundary condition with zero shear stress. The GCM was modelled as a stationary wall with a no-slip shear condition.

5.4 Mesh

The accuracy of the results from a CFD simulation depends greatly on the quality of the generated mesh. Two mesh strategies were investigated for use in this research; that of an adaptable mesh which is iteratively refined during the simulation, and using what are called local bodies of influence.

The adaptable mesh strategy proved to be very time consuming for each simulation to reach a converged result. For this reason, the body of influence mesh strategy was used for all simulations.

The mesh was converted from a tetrahedron-based geometry to a polyhedral-based mesh. The reason for using a polyhedral mesh was that the computational time was greatly reduced without any great losses in accuracy. The generated polyhedral mesh can be seen in Figure 59 below.

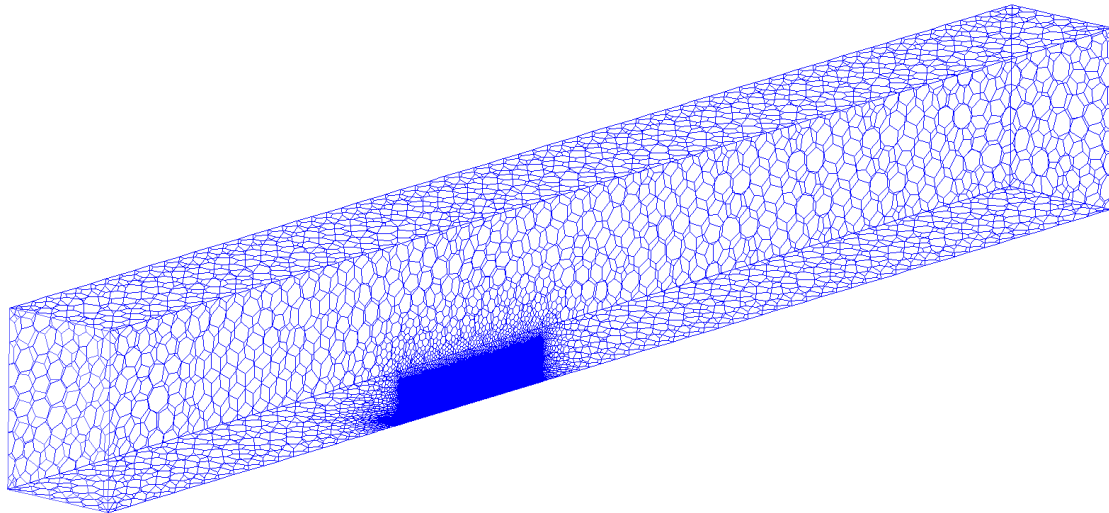


Figure 59. Generated polyhedral mesh.

A body of influence was used to refine the mesh in areas of interest. A rectangular refinement box was added which covered the entire truck, and extended into the wake region. The refinement box can be seen in Figure 60 below as the darker coloured rectangle that surrounds the truck.

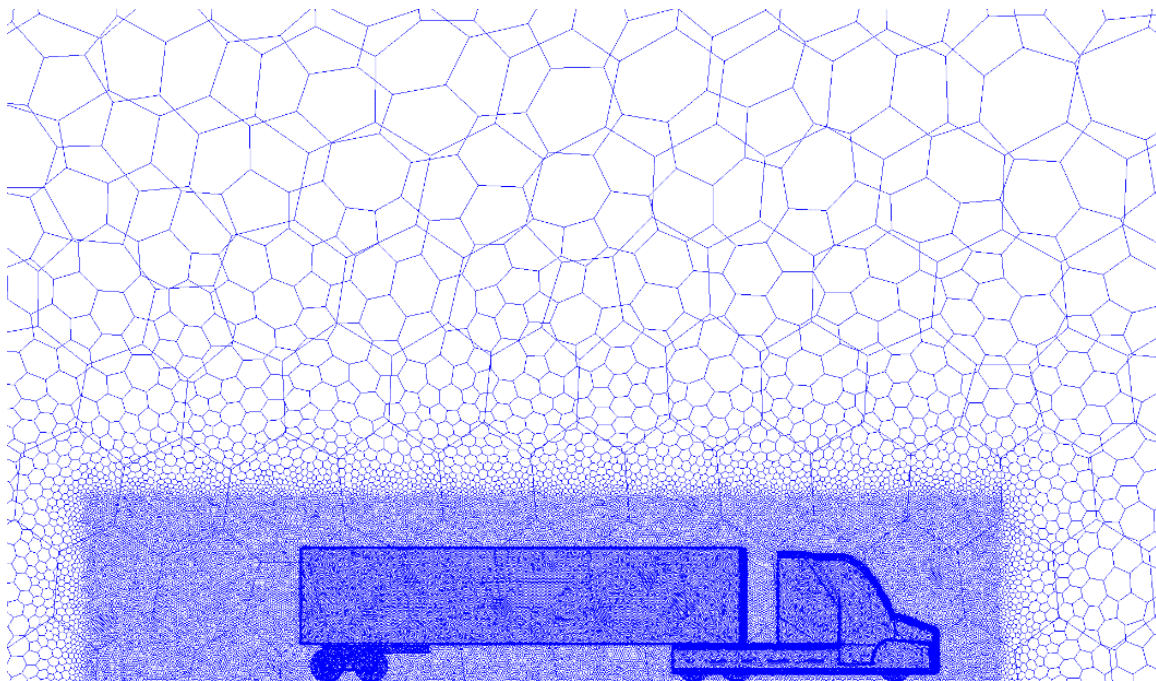


Figure 60. Mesh refinement box around the GCM.

In CFD software, the polyhedral elements at the surface of the truck are extruded into prism elements which make up the boundary layer over the truck surface.

One of the key attributes that define mesh quality is the dimensionless distance from the wall (Y^+). When solving the viscous sub-layer of the boundary layer, a Y^+ value of approximately <5 is required, however this requirement greatly increases the computational demand of the simulation (Versteeg & Malalasekera, 2007:58). While using a log-law wall function does not resolve the viscous sub-layer, it does reduce the computational demand. For this wall function approach, a Y^+ range of $30 < Y^+ < 500$ is acceptable (Versteeg & Malalasekera, 2007:58). The wall function approach is suitable to many bluff bodies as well as modern vehicle design (LEAP CFD Team, 2013).

Within the inflation layer of prism cells generated from the surface mesh, the height of the first prism cell (Δy_1) within this inflation layer is important to achieving an adequate Y^+ value.

To determine the required Δy_1 ; the Reynolds number for the GCM had to be determined. The equation for finding the Reynolds number is given by equation (5.1) below (Katz, 2016:126).

$$Re = \frac{\rho UL}{\mu} \quad (5.1)$$

Where ρ is the fluid density, U is the freestream velocity, L is the characteristic length, and μ is the fluid viscosity.

For simulations of the GCM: $\rho = 1.225 \text{ kg/m}^3$, $U = 27.8 \text{ m/s}$, $\mu = 1.79 \times 10^{-5} \text{ kg/m.s}$, and $L = 2.2675 \text{ m}$. L in this case is taken as the width of the frontal area of the GCM that is perpendicular to the incoming flow.

When these values are input into equation (5.1), the value of the Reynolds number is found to be 4.93×10^6 .

The governing equation for Δy_1 is given by equation (5.2) below (Versteeg & Malalasekera, 2007:275).

$$\Delta y_1 = \frac{Y^+ \mu}{\rho U_\tau} \quad (5.2)$$

Where U_τ is the fluid frictional velocity that is given by equation (5.3) below (Wendt, 2008:323).

$$U_\tau = \sqrt{\frac{\tau_w}{\rho}} \quad (5.3)$$

Where τ_w is the wall shear stress, which is given by equation (5.4) below (Nunn, 2018:220).

$$\tau_w = \frac{1}{2} C_f \rho U^2 \quad (5.4)$$

Where C_f is the skin friction coefficient for external flows, given by equation (5.5) below (Nunn, 2018:259).

$$C_f = 0.058Re^{-0.2} \quad (5.5)$$

Using a value for Y^+ of 100, and beginning with equation (5.5), working in reverse order through to equation (5.2), the value of Δy_1 is found to be 4mm. Thus the height of the first prism cell in the boundary layer is manually set to 4mm.

The equation for the approximation of the boundary layer thickness is given by equation (5.6) below (Anderson, 2010:375).

$$\delta = \frac{0.37x}{Re^{\frac{1}{5}}} \quad (5.6)$$

Where x is the characteristic length.

Using the calculated value of Re and using a value of 2.2675m for the characteristic length x , the approximate boundary layer thickness is calculated to be 39.5mm.

To define the inflation layer, the first layer height is set to 4mm, a growth rate for the subsequent layers is set to the default 20%. Sufficient layers are added to cover the calculated boundary layer thickness of 39.5mm. The inflation layer on the front of the GCM tractor can be seen in Figure 61.

The outward growth rate of the prism cells is noticeable. The default growth rate of 20% for the prism cells proved to be sufficient as it can be seen that prism cells merge into the polyhedral cells with relatively little skewness.

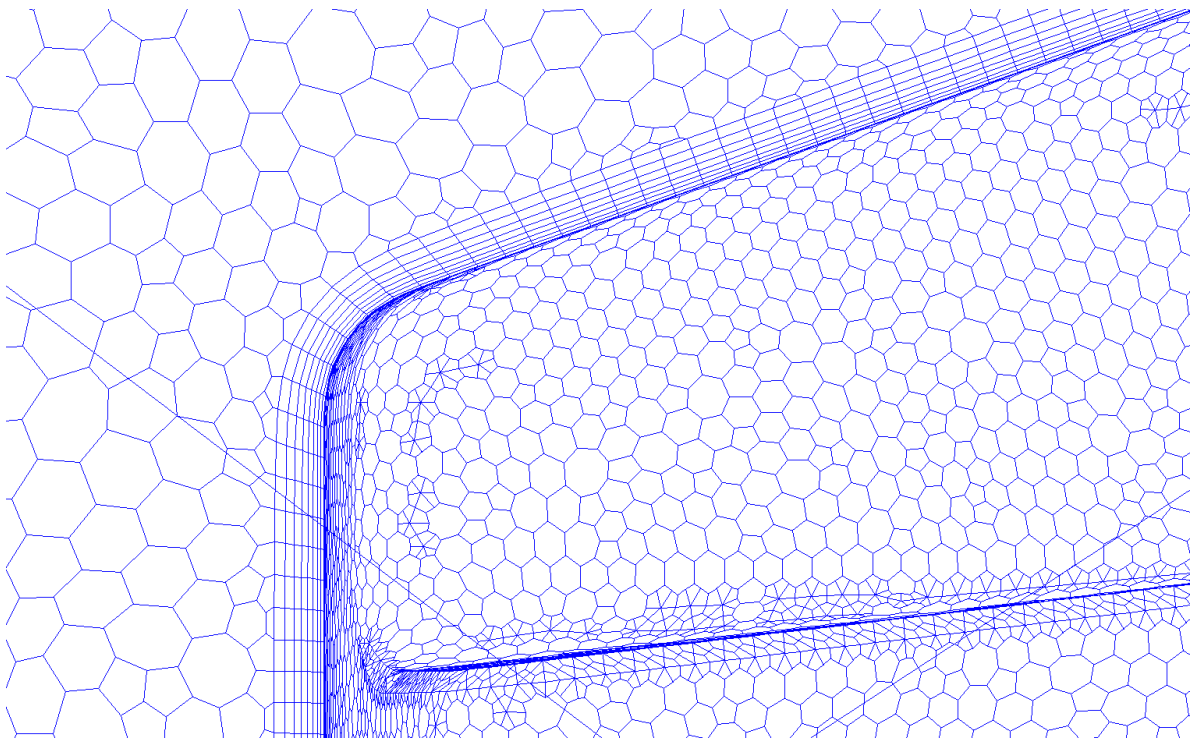


Figure 61. Inflation layer on the GCM.

5.5 CFD solver setup

The CFD software used in this study is ANSYS Fluent Student. The simulation utilises the RANS equations as this study is concerned with the effect and comparison of multiple geometry changes on drag. For this purpose, the average drag equations sufficed. As there were computational limits, both on the solving PC and the student version of the software, the RANS strategy had the advantage of reduced computational time compared to other simulation models.

The coupled solver was selected over a segregated solver. The reasoning behind this was that, while the coupled solver uses more computational resources, it reaches a converged result much faster than the segregated solver (ANSYS, 2009). This attribute proved to be important, especially when conducting simulations for multiple geometry concepts and changes.

As described in sections 3.3.4 and 3.3.5, the realizable $k-\varepsilon$ model was selected as the turbulence model.

Non-equilibrium wall functions were used to model the near-wall region of the domain. Non-equilibrium wall functions have an advantage over standard wall functions, in that they can account for the effects of pressure gradients, provide more accurate descriptions of flow separation, reattachment, and especially their ability to accurately predict skin-friction coefficients (ANSYS, 2009).

5.6 GCM drag coefficient validation

The CFD simulation of the GCM was conducted under the conditions mentioned from 5.2 to 5.5. The drag coefficient graph is shown in Figure 62 below.

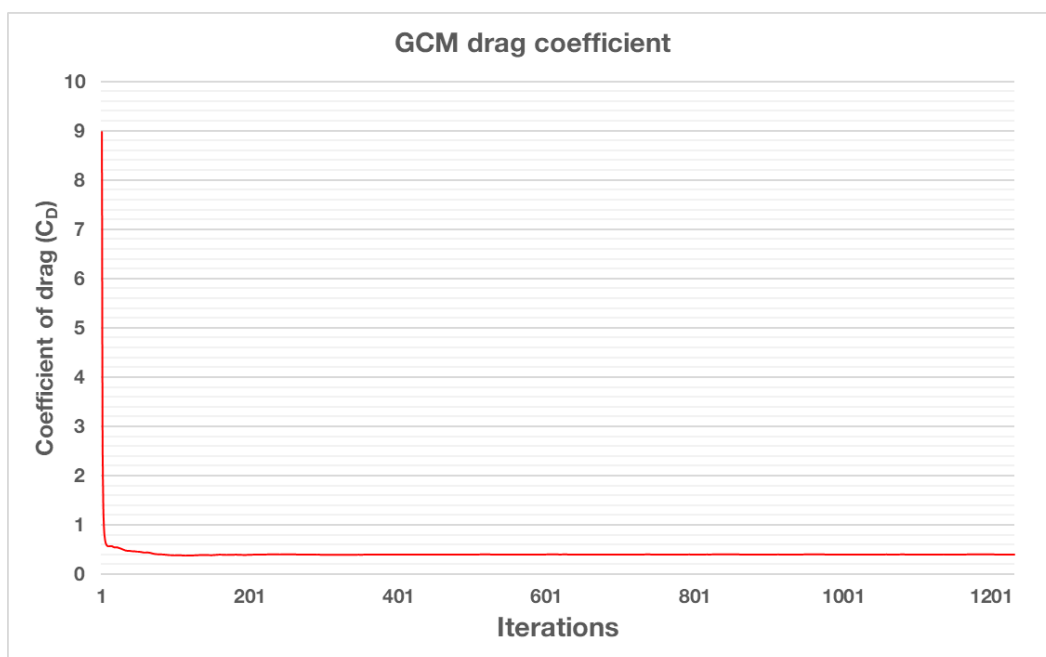


Figure 62. Drag coefficient graph for the GCM.

The drag coefficient value stabilised to 0.403 after 1232 iterations. Compared to the experimental value for C_D of 0.397, the CFD simulation result for C_D was 1.244% higher. This discrepancy was due to the limitation of element quantities of the student version of Ansys Fluent as well as the computational limits of the solving computer.

Figure 63 below shows the wall Y^+ values for the GCM; it can be seen that the Y^+ values were within the limit mentioned in 5.4.

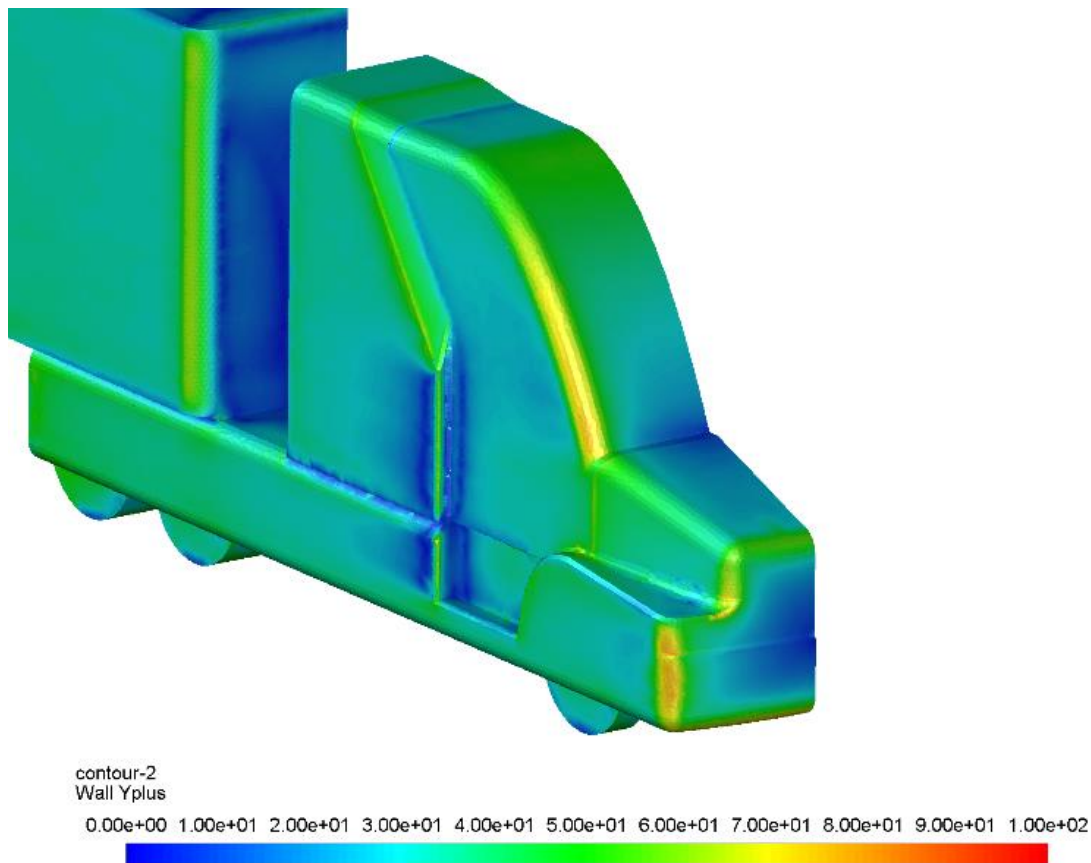


Figure 63. Wall Y^+ value for the GCM

5.7 Analysis of the GCM CFD simulation

Examining the pressure distribution over the GCM, as shown in Figure 64 below, high pressure zones can be seen at the nose, the intersection between the hood and windscreen, as well as in the frontal area of the trailer.

Another high pressure zone can be seen in the geometry of the cab door recess, and the step created for easier driver entry into the cabin.

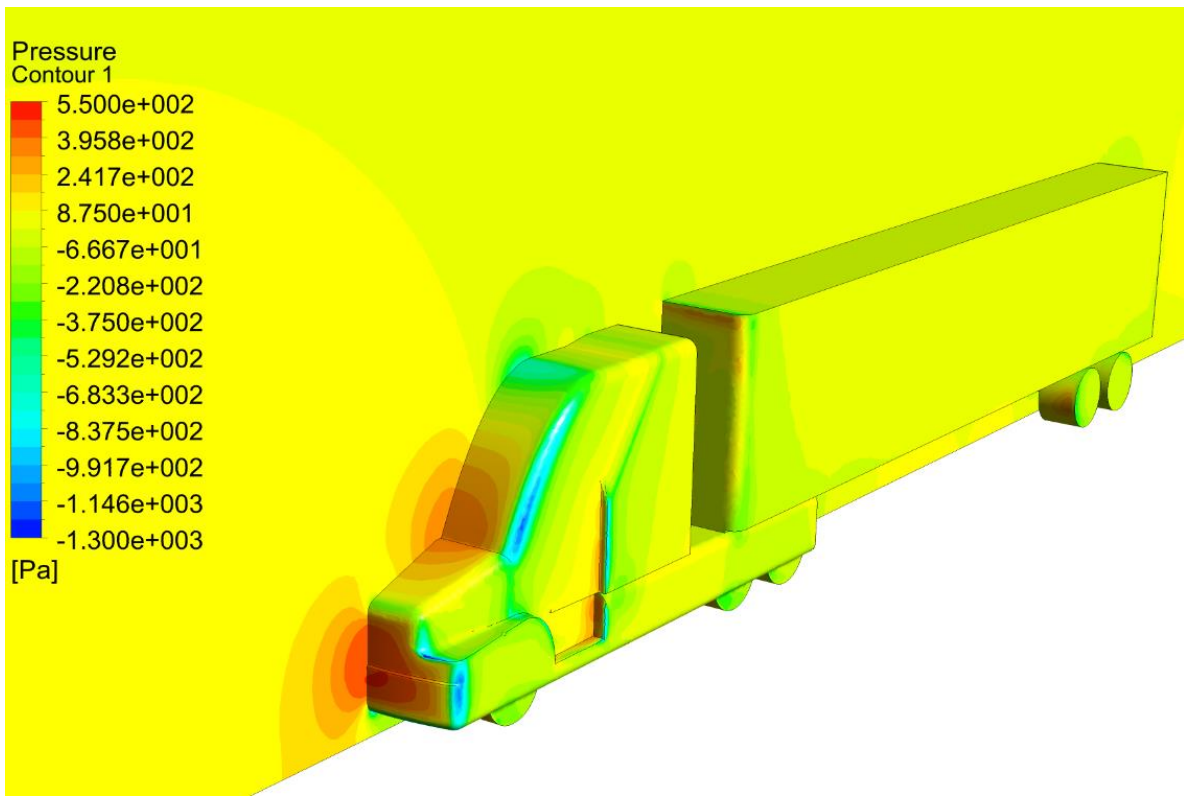


Figure 64. Pressure distribution over the GCM.

Figure 65 shows the flow velocity magnitude (top), the flow vorticity magnitude (middle), and the pressure coefficient (bottom) of the flow over the GCM. It can be seen how the blunt nose, cabin windscreen angle and the tractor-trailer gap contribute to generating flow effects that increase the aerodynamic drag.

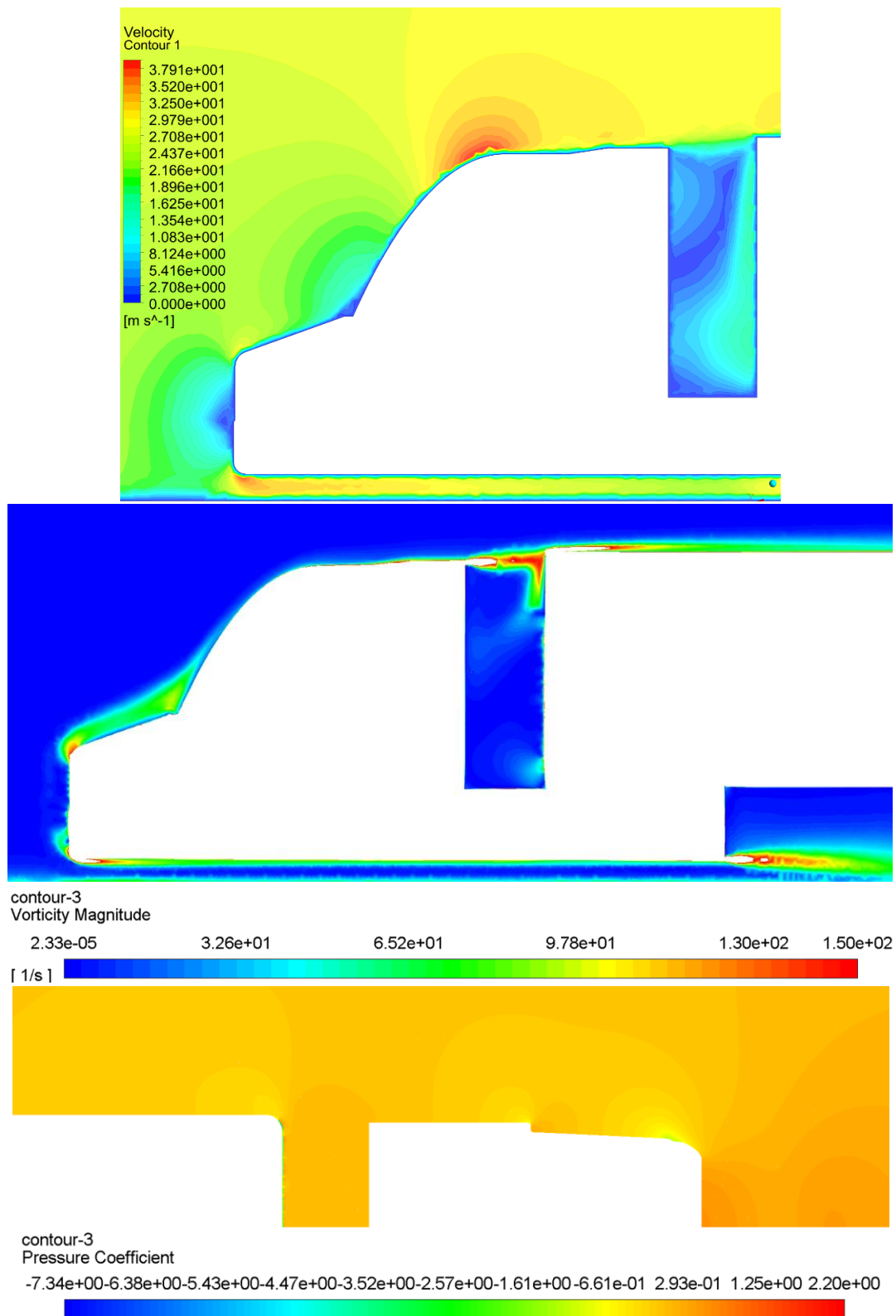


Figure 65. Flow velocity magnitude (top), flow vorticity magnitude (middle), and flow pressure coefficient as seen from the top view of the GCM (Bottom).

Aside from the high pressure zones shown in Figure 64 and Figure 65 (bottom), the GCM geometry also created highly turbulent flow on the front face of the trailer, increasing the overall drag on the vehicle.

The bluntness of the nose on the GCM as well as on modern trucks is a consequence of legislation on overall length as well having to accommodate the engine and cooling package/s of a modern diesel ICE into the design.

It is evident that there are areas of the GCM which contribute to the overall aerodynamic drag on the vehicle. The most prominent of these areas are the tractor blunt nose, the transition from the hood to the cabin windscreen, the tractor-trailer gap, as well as the transition of the floor of the tractor into the rear face of the tractor.

Chapter 6

Concept discussion

6.1 Concept autonomous BET

The potential aerodynamic advantage of an autonomous BET over a conventional ICE truck is that the geometry can be simplified and more streamlined. The inclusion of a cabin for the driver, as well as a raised nose to accommodate the ICE and associated systems gives the conventional ICE truck a larger frontal area which dramatically increases aerodynamic drag.

An autonomous BET does not have to include geometry provisions for these features, hence the bodywork can be smoother with fewer sharp transitions, and cooling ducts.

Two concepts were created: Concept One and Concept Two. Concept One is based on a least frontal area approach, which results in a theoretically lower aerodynamic drag for the tractor. Another perceived benefit of this approach is lower manufacturing cost and lower GHG emissions from the reduced raw material used. Concept Two is based on approximating the longitudinal geometry of the tractor-trailer combination to resemble that of an aerofoil, again for the purposes of reducing overall aerodynamic drag.

6.1.1 Concept One

The first concept was designed with a minimal frontal area approach, and a design envelope that fits around the auxiliary systems with no extra features exposed to the airflow. This was done as the frontal area of a vehicle is directly proportional to the aerodynamic drag. The nose section of Concept One was shaped to approximate as close as possible that of an aerofoil shape, for the purposes of reducing the aerodynamic drag. The geometry has a smooth transition from the nose to the rear of the tractor, which is to mitigate against flow separation which would otherwise increase the aerodynamic drag. For the purposes of direct comparison to the GCM, the wheel geometry and position on Concept One is the same as that used on the GCM. A blend between lower and upper surfaces is added to the geometry to allow a more gradual and smooth transition of airflow over these surfaces. The rear section of the tractor is created to approximate the geometry of GCM in this area, for initial direct comparison between the two. The nose also incorporates a smoothly tapering geometry transition from the front to the side of the tractor. This smooth transition is again added to mitigate the formation of flow separation in this area as the geometry transitions from the front surface to the side surfaces. Unlike the nose of the GCM, the nose on Concept One is devoid of any surfaces that are perpendicular to the

airflow which would otherwise greatly increase flow separation and aerodynamic drag.

Aside from these aspects, a smaller tractor also has benefits of lower manufacturing cost, lower material usage, easier maintenance access, lower mass, and lower energy consumption.

The concept was investigated with an unmodified trailer. Concept One is shown in Figure 66 below. The schematic showing the autonomous BET components is shown in Figure 67.

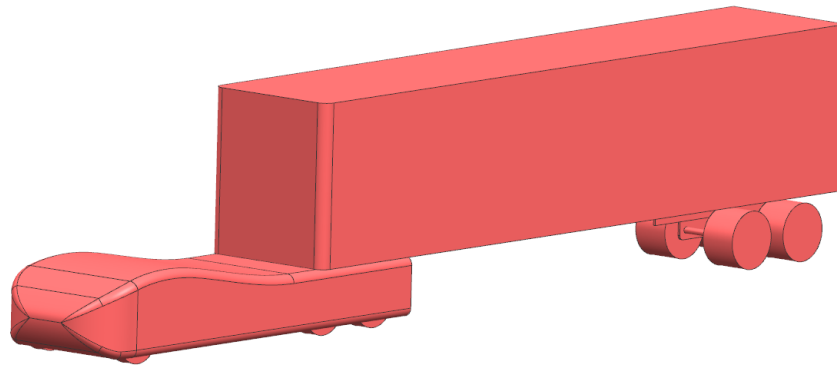


Figure 66. Autonomous BET Concept One.

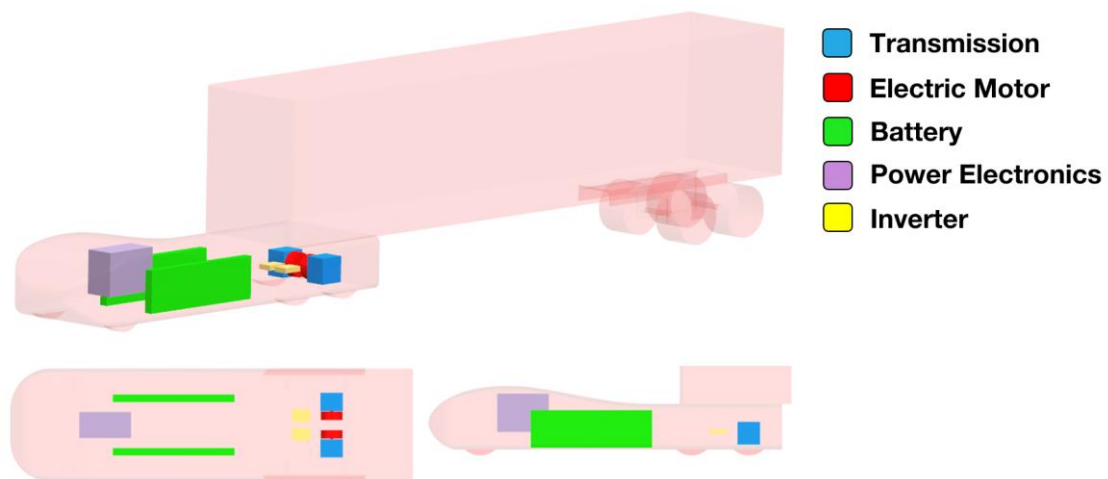


Figure 67. Concept one schematic shown in isometric view (top), plan view (bottom left), and side view (bottom right).

6.1.2 Concept Two

Concept Two was designed in a more integrative manner between tractor and trailer, smoothly transitioning the airflow along the surfaces without many abrupt geometry changes, because any abrupt changes could possibly induce flow separation and thereby increase the aerodynamic drag.

The initial design was again based on using an unmodified trailer for the purposes of direct comparison. The shape of the tractor-trailer was approximated as closely as possible to a traditional aerofoil shape, in an attempt to reduce aerodynamic drag and the number of geometric features which could lead to flow separation.

The tractor-trailer gap was reduced as much as possible while still allowing the trailer and tractor to rotate relative to each other without interference. As noted in the literature review, there is a proportional relationship between tractor-trailer gap and aerodynamic drag, hence the requirement for reducing this gap as much as possible for the goal of reducing the overall aerodynamic drag. The upper most surface of the tractor was 5mm higher than that of the leading edge of the trailer, in order to ensure the airflow that transitioned from the tractor to the trailer did not encounter the perpendicular front face of the trailer, but rather flowed over the top of the trailer.

As with Concept One, a smooth blended geometry was added as a transition between top, front and side surfaces, and the concept was devoid of any surfaces that were perpendicular to the airflow which would otherwise greatly increase flow separation and aerodynamic drag.

For the purposes of direct comparison to the GCM, the wheel geometry and position on Concept Two was the same as that used on the GCM. The rear section of the tractor was created to approximate the geometry of GCM in this area, for initial direct comparison between the two.

Concept Two incorporates the same components and topology as was used for Concept One.

Figure 68 below shows the CAD geometry of Concept Two.

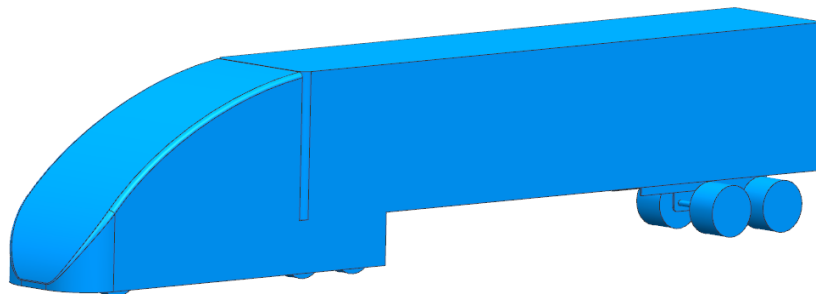


Figure 68. Autonomous BET Concept Two.

Chapter 7

Results and discussion

7.1 Concept One – Results

This concept was simulated under the exact domain specifications as was used in the GCM CFD validation, but with one major change; this concept as well as the concepts that follow were simulated with a rolling road condition applied to the floor of the CFD domain.

The C_D value for this concept was found to be 0.68. This is a 40.7% increase over the validated GCM. The main reason for this dramatic increase in drag is that the entirety of the trailer front face was exposed to the incoming airflow. This flow separation area proved to be the single greatest area responsible for the aerodynamic drag on the vehicle.

While this result means an autonomous BET in this configuration is not suitable for long-haul transport on highways, the reduced size and material usage for this concept could make it an applicable design for autonomous BETs used in ports and shipping yards for trailer transportation over small distances and speeds lower than 30km/h.

Figure 69 shows the flow pressure coefficient (top), and flow velocity magnitude (bottom) over Concept One.

It can be clearly seen how the trailer creates a very high pressure zone in front, and a low pressure zone on top of the trailer front edge, as the flow separates in this region.

It can also be seen how the flow velocity decreases significantly in this same trailer frontal region. The tractor nose also presents a significant pressure rise. To lessen this effect, the nose radius as well as its height above the ground plane would need to be lowered.

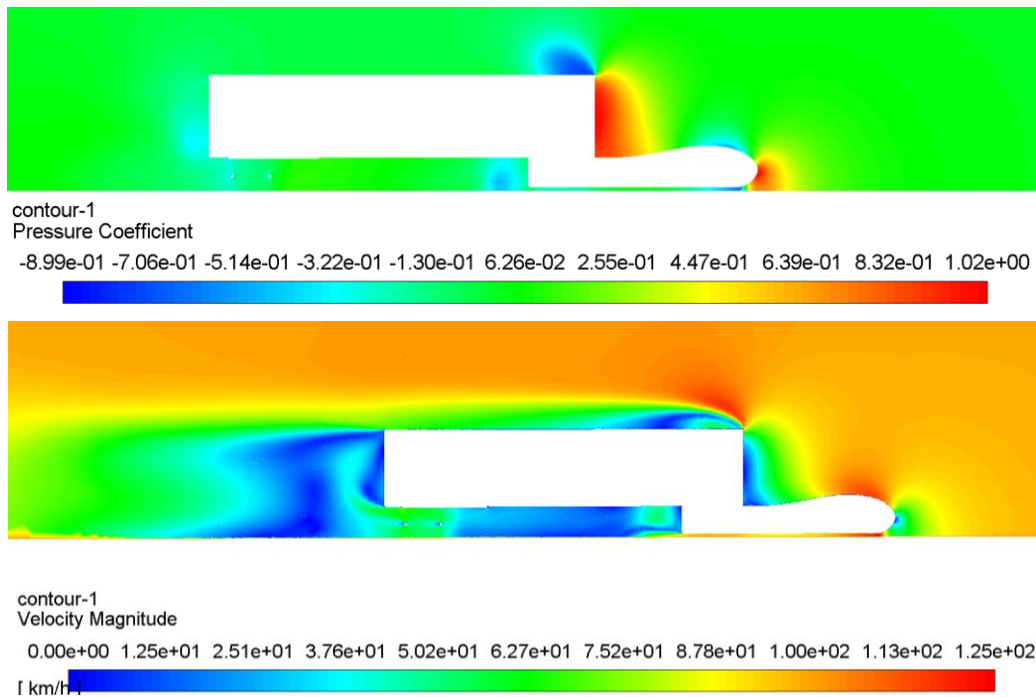


Figure 69. The flow pressure coefficient (top), and flow velocity magnitude (bottom) over Concept One.

7.2 Concept Two – Results

The lessons learned from Concept One were applied to the construction of Concept Two, especially in the area of the tractor nose.

The converged C_D value for this concept was found to be 0.354. This represents a reduction of 13.8% over the GCM. Looking at the flow pressure coefficient over Concept Two, as shown by Figure 70 below, it is clear that the high pressure zone at the nose had been reduced compared to Concept One. From Figure 70 it is also clear that the transition area from the front of the truck to the sides create a sharp drop in pressure in this area. To reduce this sharp low pressure effect, a larger radius transition is examined in the revision to Concept Two.



Figure 70. Flow pressure coefficient over Concept Two (left), and a magnified view of the frontal area (right).

Figure 71 below shows the flow velocity magnitude (top), and the flow vorticity magnitude (bottom) over Concept Two. From this, it is seen that the lower surface of the truck in Concept Two creates a sharp geometry change which results in flow separation and an increase in vorticity in this area, both of which contribute to increased aerodynamic drag. To reduce this effect, a radius was added to the floor of the truck in subsequent revisions of Concept Two. This geometry change will henceforth be referred to as Concept Two revision A.

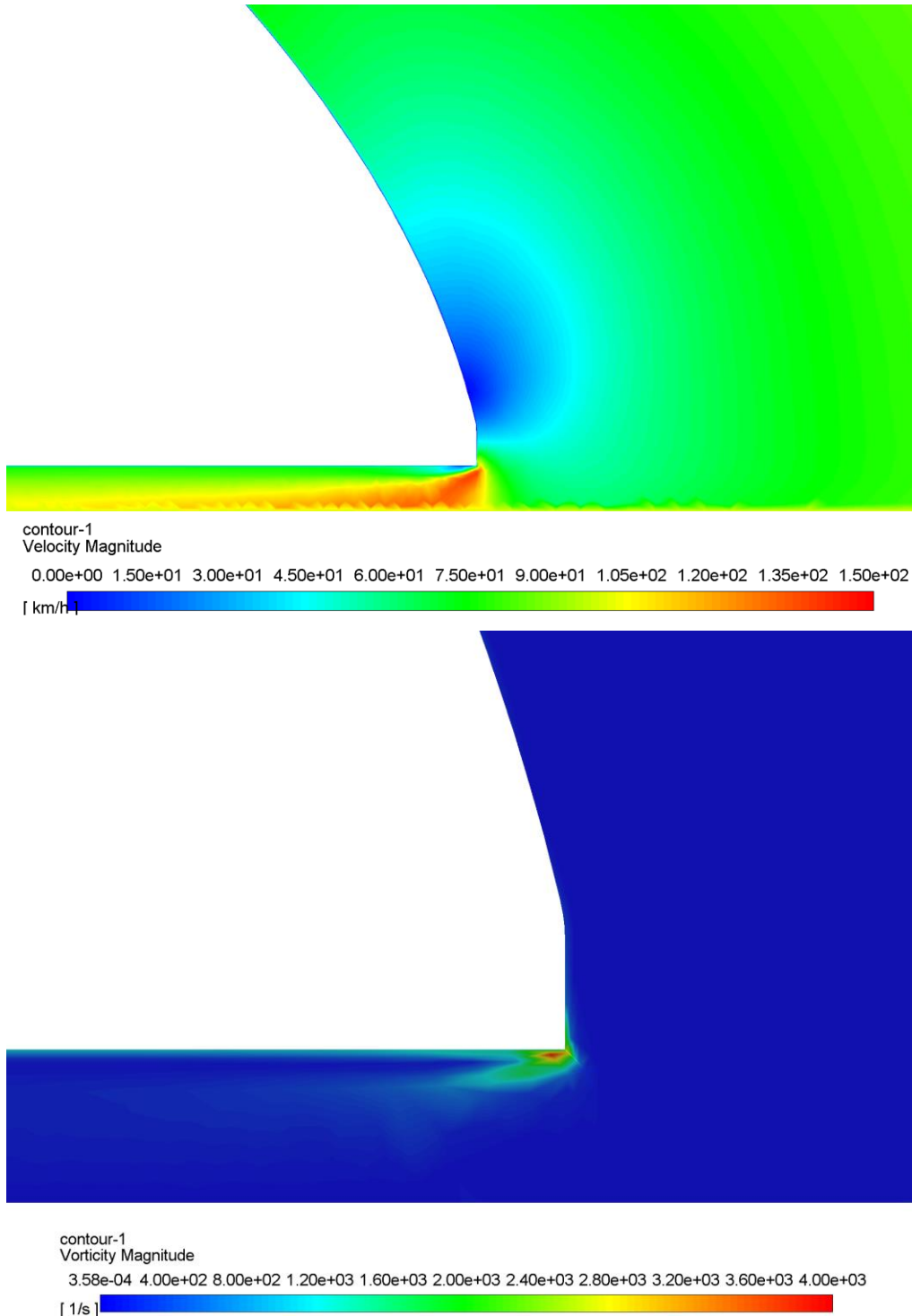


Figure 71. Flow velocity magnitude (top), and flow vorticity magnitude (bottom) over Concept Two.

7.2.1 Concept Two – Revision A

The required geometry changes mentioned above are shown in Figure 72 below. For the side radius, a non-linear radius was created. A large radius of 500mm was added at the lower area, while a tighter 80mm radius was added at the top.

The reason for a tighter radius at the top was to avoid an abrupt transition of airflow from the tractor to the top front edge of the trailer. A tighter radius at the top also maintained a no-interference condition between the tractor and trailer rotation mode.

A linear 200mm radius was added to the tractor floor to reduce the aerodynamic effects shown in Figure 71 above.

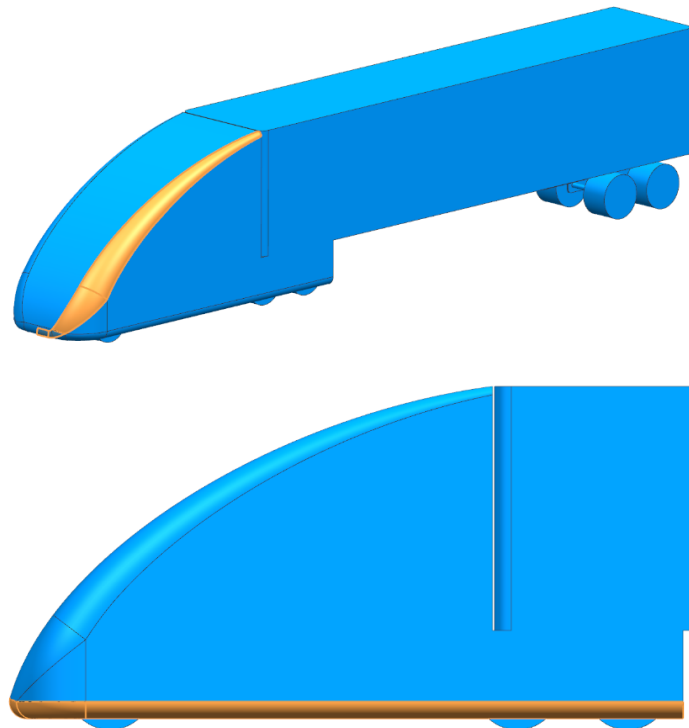


Figure 72. Tractor side (top) and floor (bottom) radius changes for Concept Two - Revision A, highlighted in orange.

The converged C_D value for Concept Two with these two geometry changes was found to be 0.331. This figure represents a 6.49% reduction in C_D when compared to the baseline for Concept Two, and a 17.87% reduction in C_D when compared to the GCM.

Figure 73 below shows a comparison of the pressure coefficient between Concept Two (left) and Concept Two - Revision A (right).

It is clear that the radius changes have reduced the sharp pressure drop on the side of the vehicle – the strong blue region in Figure 73 (left) has been dispersed evenly across the geometry (right).

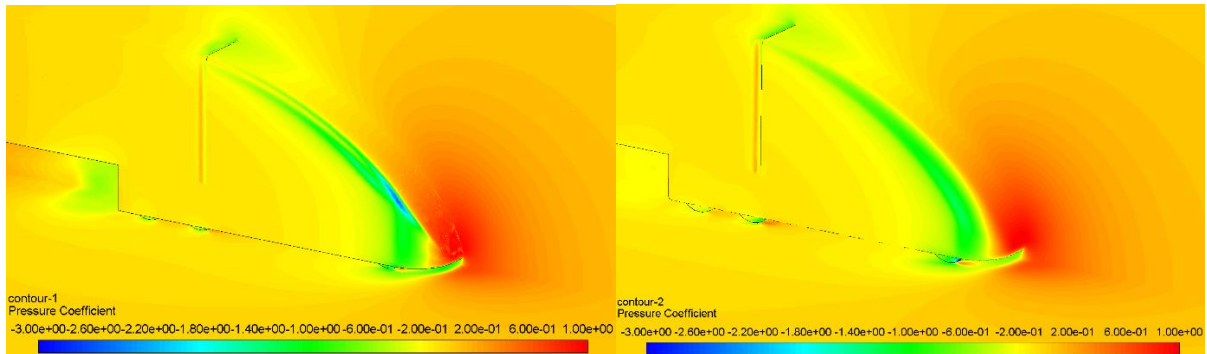


Figure 73. Comparison of pressure coefficient between Concept Two baseline (left), and Concept Two - Revision A (right).

Figure 74 below shows the dramatic reduction in vorticity at the nose of the truck from Concept Two baseline (left) to Concept Two Revision A (right).

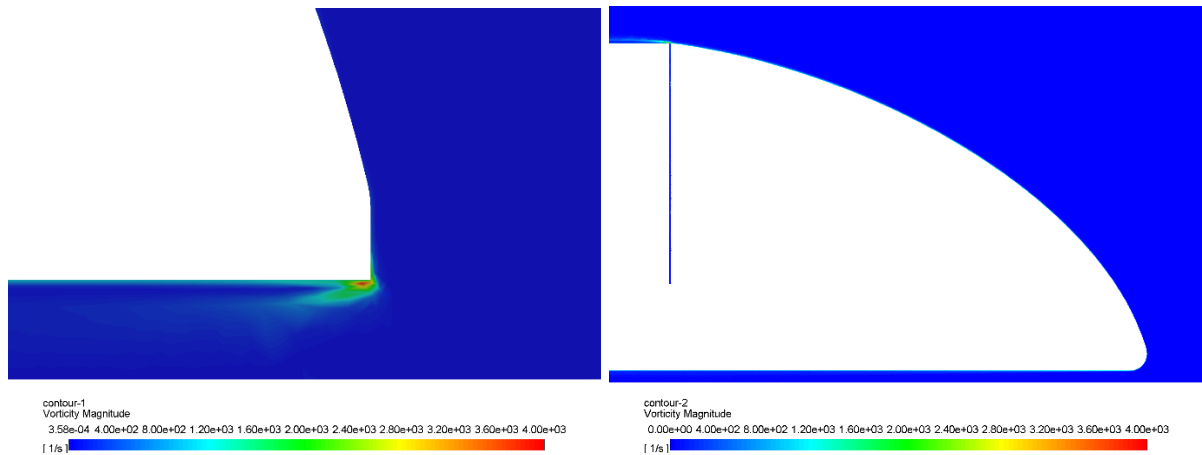


Figure 74. Comparison of vorticity magnitude between Concept Two baseline (left), and Concept Two - Revision A (right).

7.2.2 Concept Two – Revision B

The next area of interest was to reduce the wake and vorticity at the rear of the trailer. Boat tails, as discussed in section 2.3.3 have proven to be successful in reducing the wake in this region, and lowering the overall aerodynamic drag of the truck (Miralbes & Castejon, 2012). Commercial bolt-on solutions of this design are already available.

Hyams et al. (2011:37) have found that boat tail sections which have a 15° angle from the trailer centreline and a length equal to a quarter the width of the trailer have proven to work well in reducing wake formation and size, as well as reducing the aerodynamic drag.

The boat tail configuration is shown in Figure 75 below (highlighted in grey).

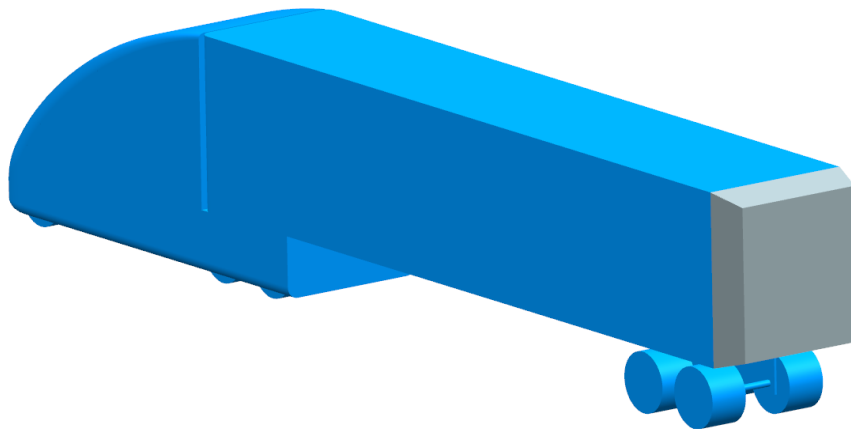


Figure 75. Concept Two – Revision B.

The converged C_D value for this configuration was found to be 0.275. This configuration of the autonomous BET shows a 31.76% reduction in C_D when compared to the validated GCM.

Figure 76 and Figure 77 below examine visually the effect of adding a boat tail. The wake size as well as the intensity have been dramatically reduced. This has resulted in a large drop in overall aerodynamic drag of the truck.

Figure 78 below also shows a ~33% reduction in vorticity magnitude when the boat tail is added to the trailer, when compared to Concept Two – Revision A.

The reduced wake size also has an impact on the vehicles travelling in the wake behind this autonomous BET.

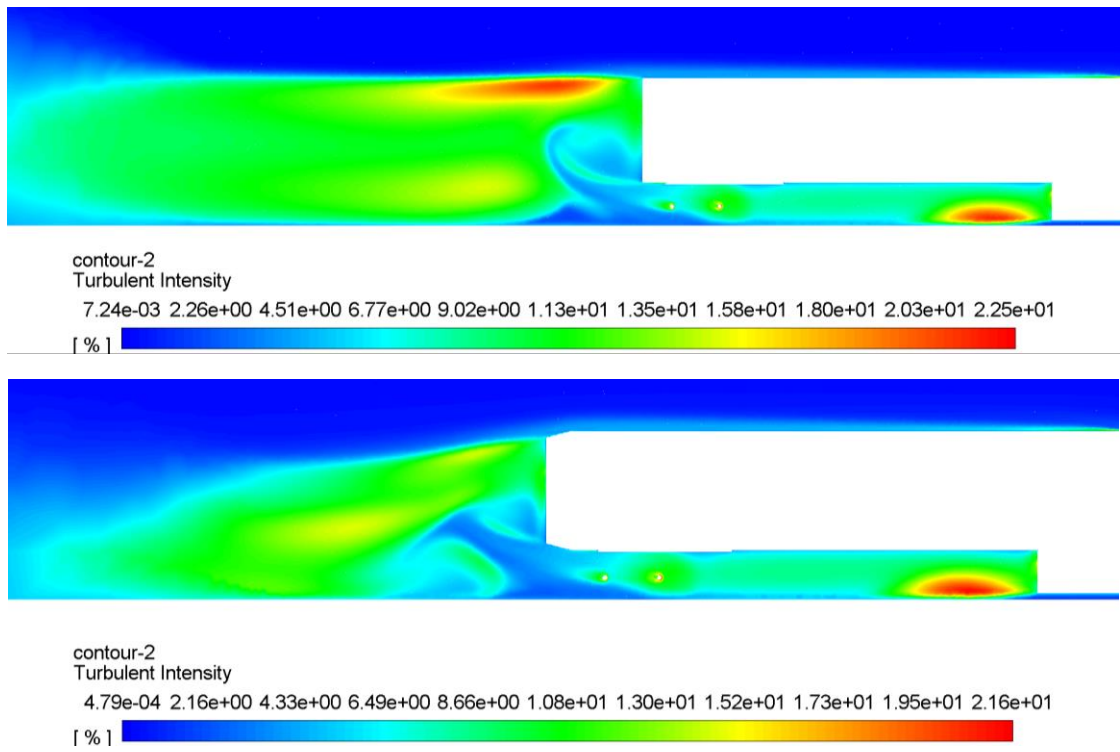


Figure 76. Side view comparison of the turbulent intensity of the flow between Concept Two – Revision A (top), and Concept Two – Revision B (bottom).

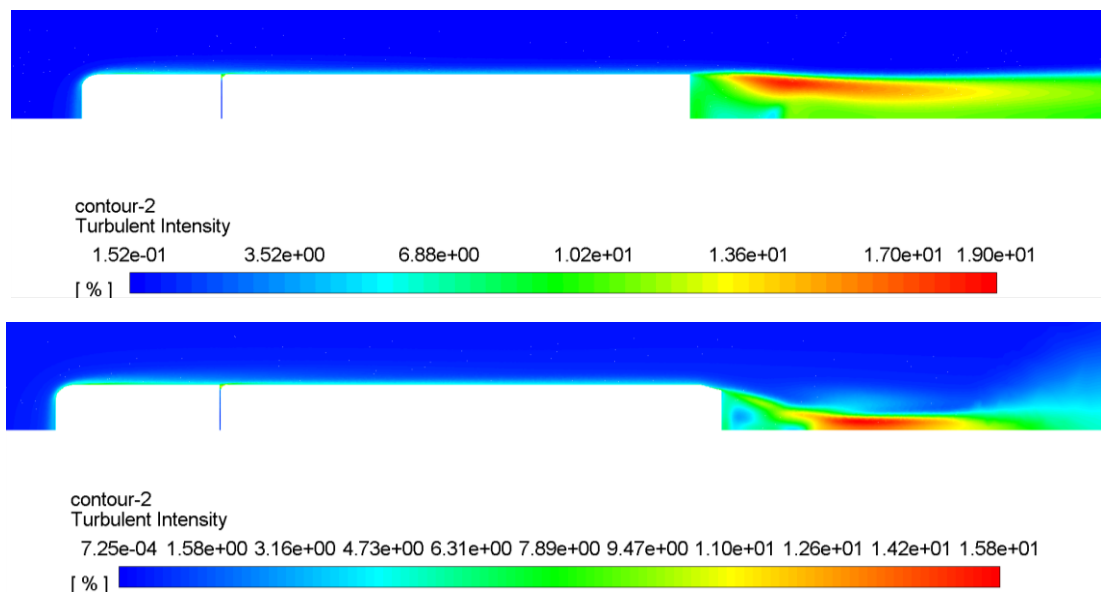
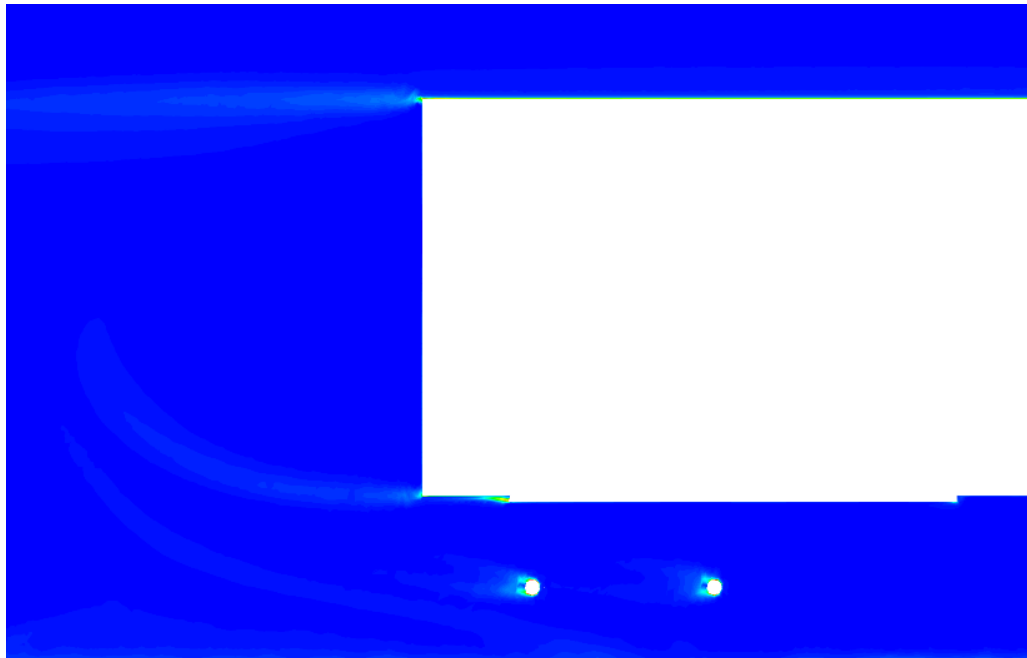
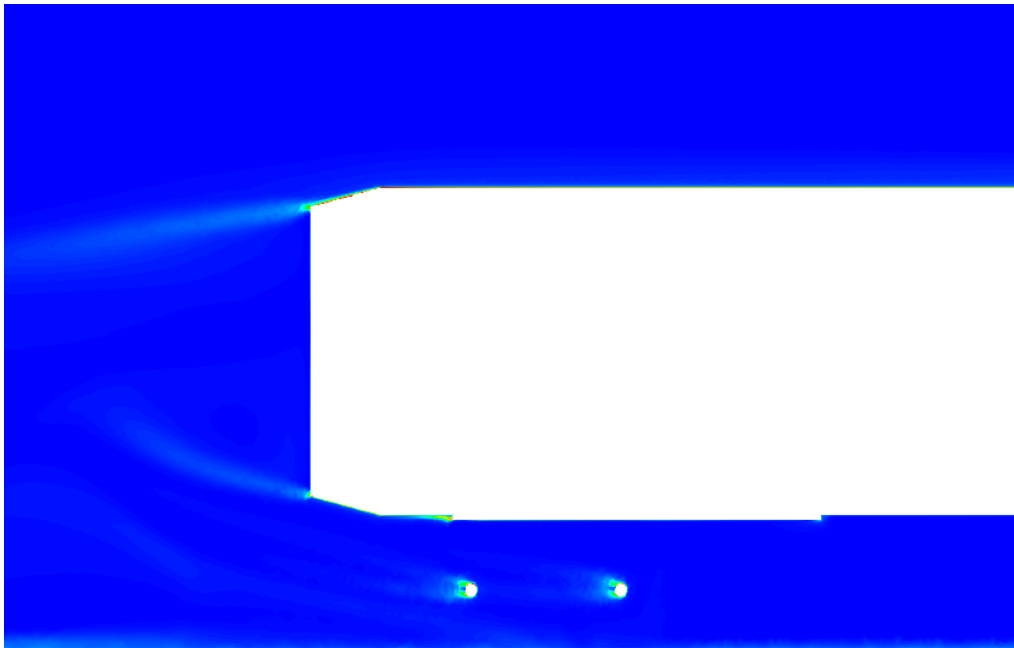


Figure 77. Plan view comparison of the turbulent intensity of the flow between Concept Two – Revision A (top), and Concept Two – Revision B (bottom).



contour-2
 Vorticity Magnitude
 3.96e-04 2.14e+02 4.29e+02 6.43e+02 8.57e+02 1.07e+03 1.20e+03
 [1/s]



contour-2
 Vorticity Magnitude
 7.18e-06 8.00e+01 1.60e+02 2.40e+02 3.20e+02 4.00e+02 4.80e+02 5.60e+02 6.40e+02 7.20e+02 8.00e+02
 [1/s]

Figure 78. Side view comparison of the vorticity magnitude of the flow between Concept Two – Revision A (top), and Concept Two – Revision B (bottom).

7.2.3 Concept Two – Revision C

Skirts were the next design feature that was examined. Figure 79 below shows the geometry for Concept Two – Revision C. Figure 79 (bottom) also shows a section of the tractor rear floor that was modified to promote a smoother transition of airflow over the back of the tractor. The skirts were not extended beyond the trailer wheels. This was done to maintain the practicality of easily changing a trailer wheel. The skirts were extended as far forward as possible without causing interference with the tractor when the truck turned. The gap that between the front of the skirts and the rear of the tractor would admit airflow into the area under the trailer. However, it was not practically possible to completely seal off this gap.

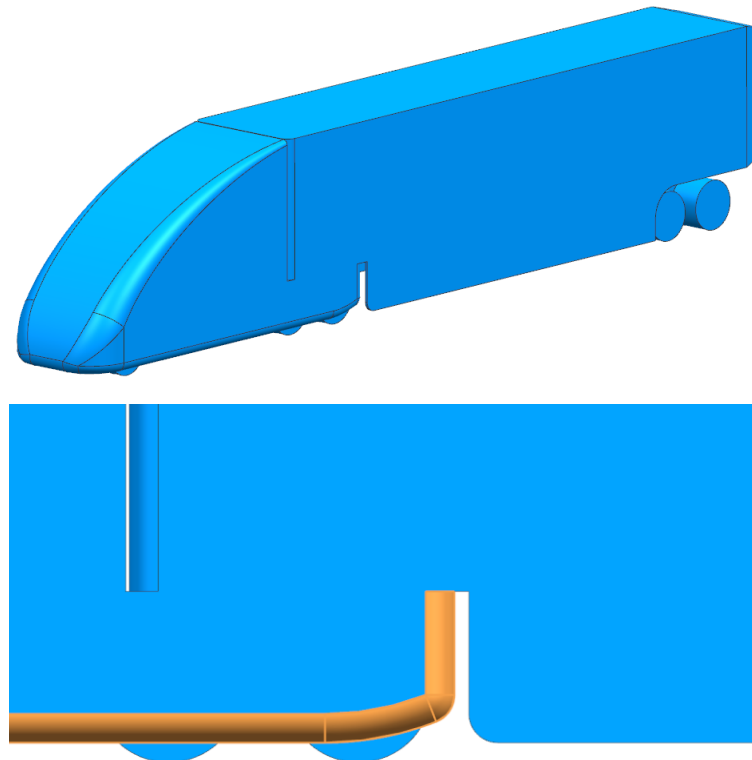


Figure 79. Concept Two – Revision B – full view (top), modified tractor rear (bottom – highlighted in orange).

The converged C_D value for this configuration was found to be 0.260.

Figures 80 and 81 below show a comparison of the pressure coefficient of the flow between Concept Two – Revision B (top), and Concept Two – Revision C (bottom). The effect of adding the skirts in combination with the tractor floor modification has seen a ~80% reduction in pressure coefficient seen by the trailer leading wheel.

Figure 81 shows that a general lowering of pressure coefficient in the area under the trailer can be seen with the introduction of Concept Two Revision C. Figure 82 below shows the general reduction in turbulent intensity with Concept Two – Revision C, especially in the area of the trailer wheels.

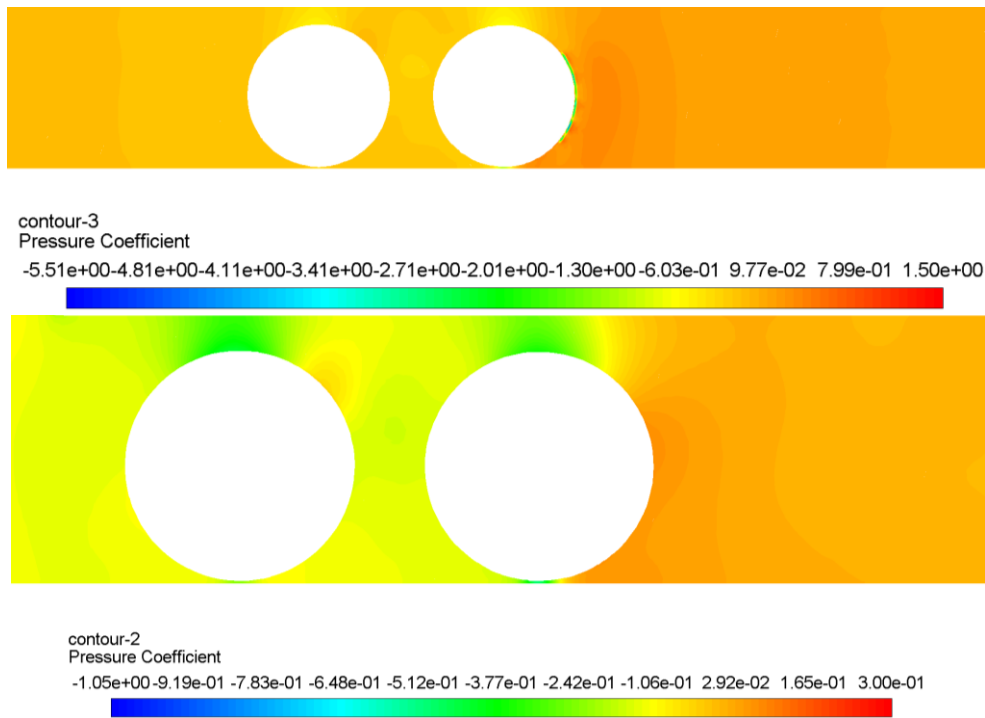


Figure 80. Side view comparison of the pressure coefficient of the flow between Concept Two – Revision B (top), and Concept Two – Revision C (bottom).

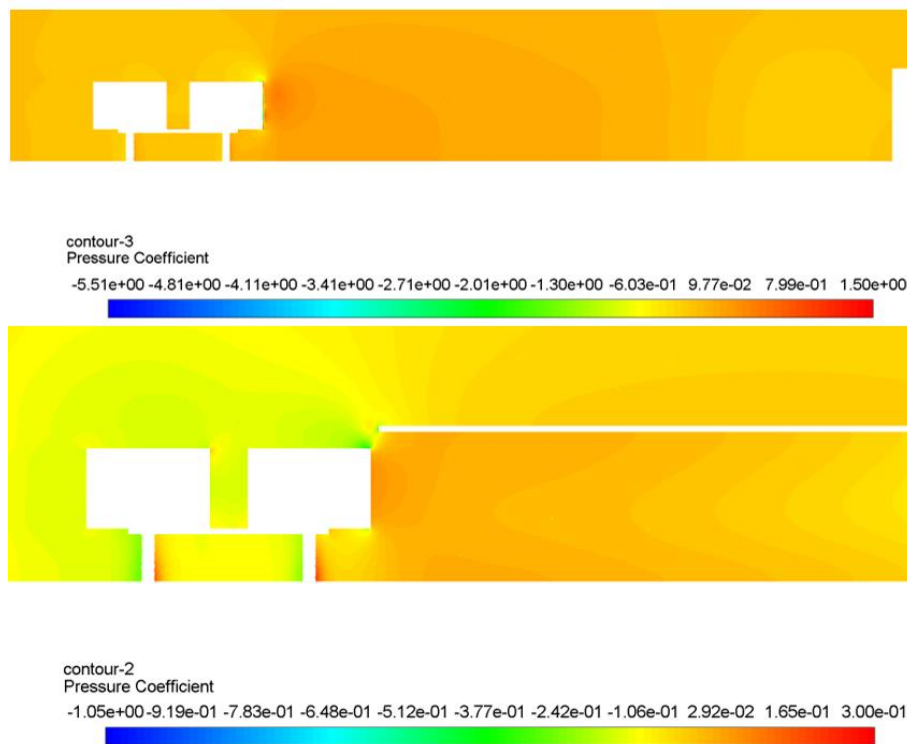


Figure 81. Plan view comparison of the pressure coefficient of the flow between Concept Two – Revision B (top), and Concept Two – Revision C (bottom).

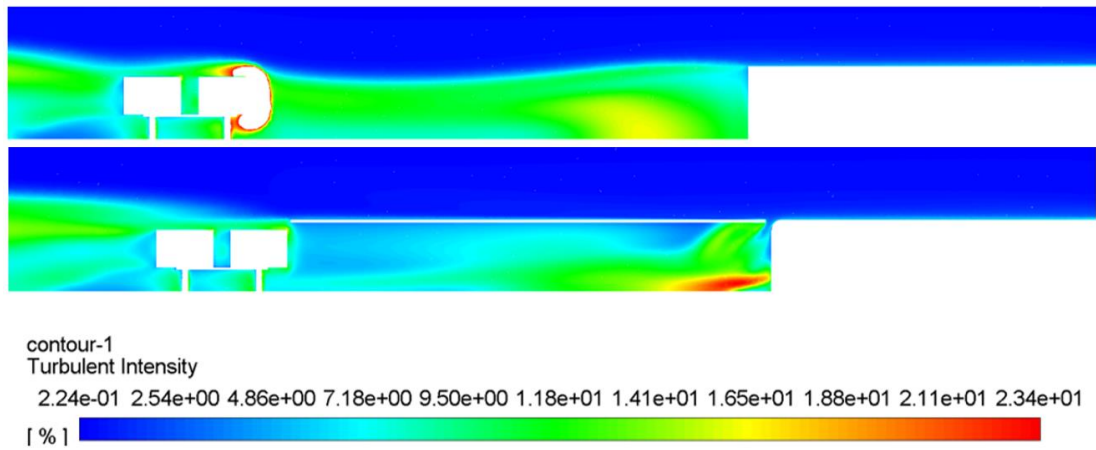


Figure 82. Plan view comparison of the turbulent intensity of the flow between Concept Two – Revision B (top), and Concept Two – Revision C (bottom).

7.2.4 Concept Two – Revision D

The final design feature examined was a tapered trailer roof. This is to simulate the aerofoil profile as much as practically possible. A 1° taper of the roofline, measured from the front edge of the trailer roof was added. This modification can be seen in Figure 83 below, highlighted in orange.

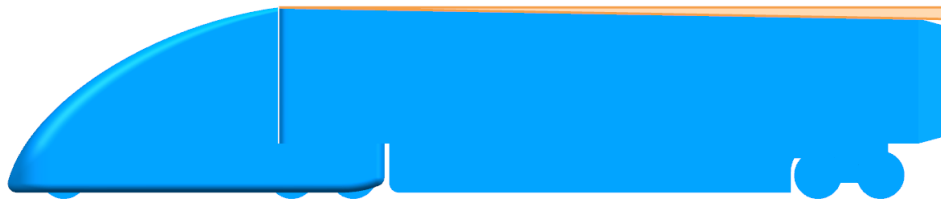


Figure 83. Concept Two – Revision D, removed geometry for the tapered roof feature is highlighted in orange.

The converged C_D value for this configuration was found to be 0.251.

Table 12 below shows a comparison of the C_D values for all the tested concepts as well the GCM.

From the table it is clear that without any modification to the trailer, an autonomous BET can provide an approximately 18% reduction in aerodynamic drag.

Table 12. Comparison of C_D values for all CFD simulated models.

3D CAD	Model name	C_D	% change in C_D relative to GCM
	GCM	0.403	0.00
	Concept One	0.680	+40.70
	Concept Two	0.354	-12.16
	Concept Two – Revision A	0.331	-17.87
	Concept Two – Revision B	0.275	-31.76
	Concept Two – Revision C	0.260	-35.48
	Concept Two – Revision D	0.251	-37.72

A discussion of each simulation result is given below.

GCM – There are obvious areas in the GCM which contribute to increased drag, namely the very blunt nose, the abrupt angle change that is present in the transition of the tractor hood to the windscreen, the driver entry step, the cabin doors and the tractor-trailer gap. These areas also have higher flow vorticity magnitudes, and lower flow velocity magnitudes which result in increased aerodynamic drag. The GCM is modelled with a smooth floor for the purposes of simplicity and reduced simulation complexity. As a result, the aerodynamic drag is lower for the GCM when compared to real world ICE trucks.

Concept One – While the tractor for this concept represents the smallest frontal area exposed to airflow of all the models simulated, the frontal area of the tractor-trailer combination is approximately the same as all other models tested. As a result, the

front face of the trailer presents a large perpendicular obstacle to the incoming airflow greatly increasing drag. The generated wake for this model is also greater than that of the GCM, due to the flow separation that occurs at the trailer front leading edges disrupting the flow along the length of the trailer.

Concept Two – Compared to the GCM and Concept One, the trailer front face on this model is the least exposed to the incoming airflow. The smooth transition from nose to the top of the trailer leading edge also resulted in the fewest flow separation points compared to the two models discussed above. The transition from nose to floor created a flow separation point as well as a source for increased vorticity, resulting in disrupted flow along the floor of the truck. While the blended geometry that transitions from upper surface of the tractor to the left and right sides of the tractor was added to reduce the possibility of flow separation, this area also resulted in creating a pressure drop on the blended surface.

Concept Two – Revision A – Following on from the findings of Concept Two, the transition area was modified with an increased radius transition, as well as adding a curved transition to the floor. The vorticity magnitude at the nose lower surface was reduced by approximately 40% when compared to Concept Two. The addition of the curved floor transition also increased the velocity magnitude under the floor of the tractor by approximately 3%.

Concept Two – Revision B – With the introduction of the boat-tail in this concept, focus shifted to analysis of the rear of the trailer. Both the wake size and intensity was reduced in the concept when compared to Concept Two – Revision A. The optimal shape of the boat-tail was taken directly from research in the literature review. In both Concept Two – Revision A and Concept Two – Revision B, there are two vortex flows that occur at the rear of the trailer, one from the top surface of the trailer and one from the lower surface of the trailer. The vortex generated at the top is larger in magnitude than that of the one created at the bottom surface, due to the trailer wheels and axles disrupting the airflow and removing energy from the airflow. With the addition of the boat-tail, the upper vortex turbulent intensity was reduced by approximately 38% when compared to Concept Two – Revision A.

Concept Two – Revision C – Trailer skirts as well as a smoother tractor rear transition were added to this concept. The most significant aspect for adding the trailer skirts was limiting the amount of airflow flowing from the tractor sides to the underside of the trailer, as well as limiting the amount airflow from the sides of the trailer itself flowing to the underside of the trailer. The skirts resulted in lowering the turbulent intensity caused by the trailer leading wheel by approximately 65% compared to the absence of skirts. The overall turbulent intensity under the trailer was reduced with the addition of the skirts, as well as being more localised towards the rear of tractor. The turbulent intensity of the flow was locally higher just behind the tractor with the addition of the skirts, due mainly to the gap between the skirt leading edge and the tractor rear face. However, the overall aerodynamic drag of the truck was reduced compared to Concept Two – Revision B which did not have any skirts added.

Concept Two – Revision D – The tapered roofline more closely approximates the profile of an aerofoil, which should theoretically provide a reduction in aerodynamic drag. This expectation was confirmed by the results. The addition of a taper to the trailer roofline also resulted in reducing the turbulent intensity of the flow by approximately 5% when compared to Concept Two – Revision C. The flow vorticity at the top rear of the trailer was reduced by approximately 32% compared to that of Concept Two – Revision C.

Figure 84 and 85 below show the pressure coefficient over the longitudinal centreline section of the GCM and Concept Two – Revision D respectively.

Inspecting the curves for the top surface of each model for the range 0m to 6m, it is clear how much smoother the curve is for Concept Two – Revision D. This is a reflection of fewer flow detachment areas, and lower turbulence for Concept Two – Revision D.

Peak high and peak low values are also lower for Concept Two – Revision D. The curves for the bottom surface show similar trends between models, with higher peak values for the Concept Two – Revision D trailer. This is due to the influence of a rolling road, road boundary layer, the sealing effect of the skirts, and higher flow velocity under the Concept Two – Revision D trailer.

Plot of the GCM pressure coefficient along the longitudinal centerline

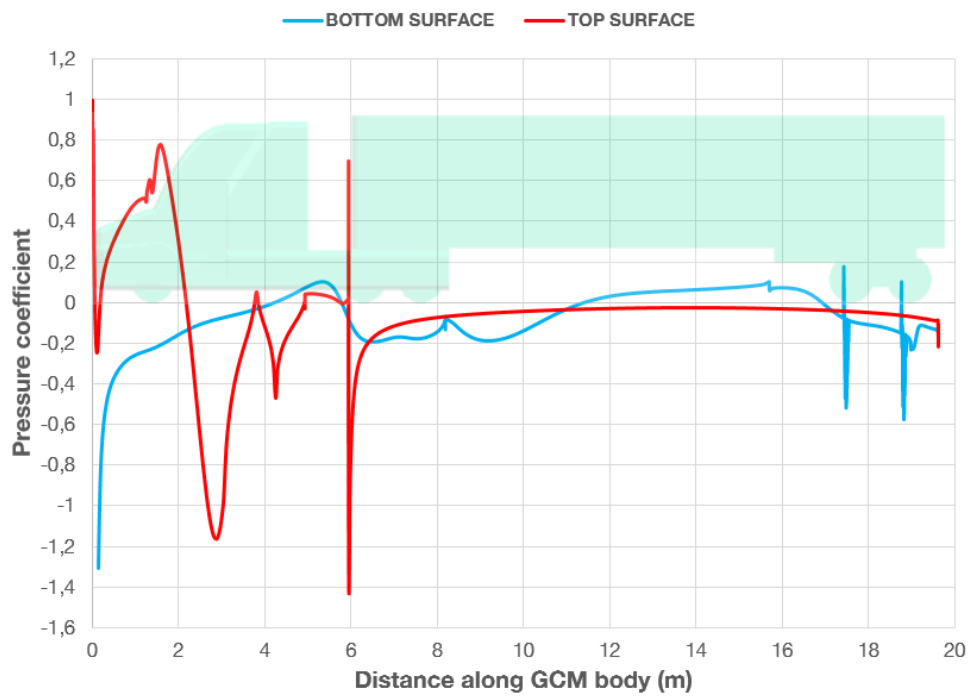


Figure 84. Pressure coefficient over the GCM body.

Plot of Concept Two - Revision D pressure coefficient along the longitudinal centerline

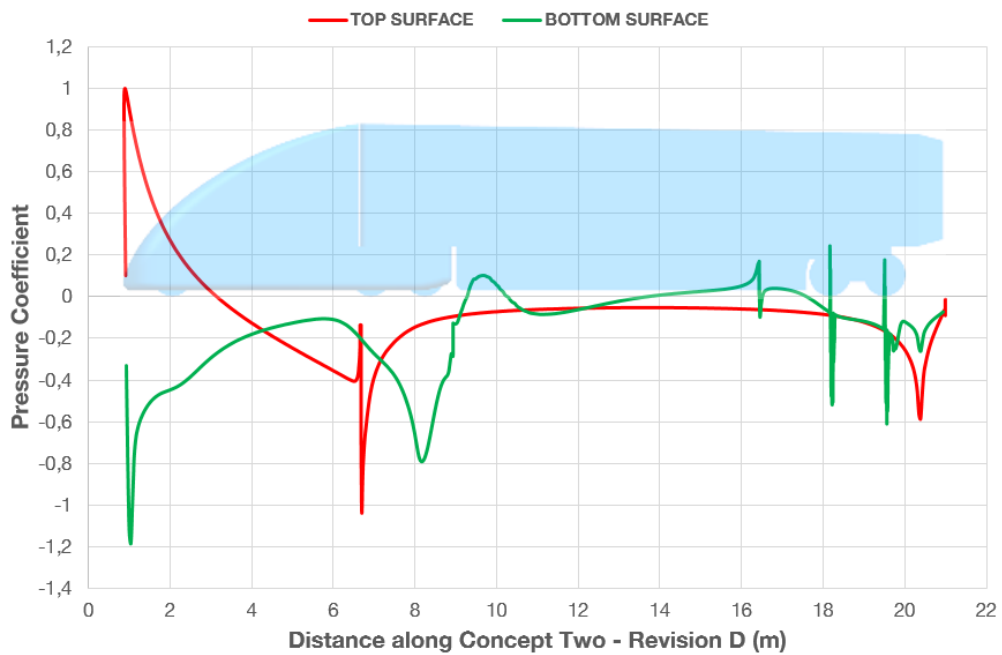


Figure 85. Pressure coefficient over the Concept Two – Revision D body.

Figure 86 and 87 below show the airflow turbulent intensity over Concept Two – Revision D and the GCM respectively. It is clear that the size, and particularly the turbulent intensity is greatly reduced in Concept Two – Revision D compared to the GCM. This difference is further emphasised when viewing the plan views of the GCM and Concept Two – Revision D.

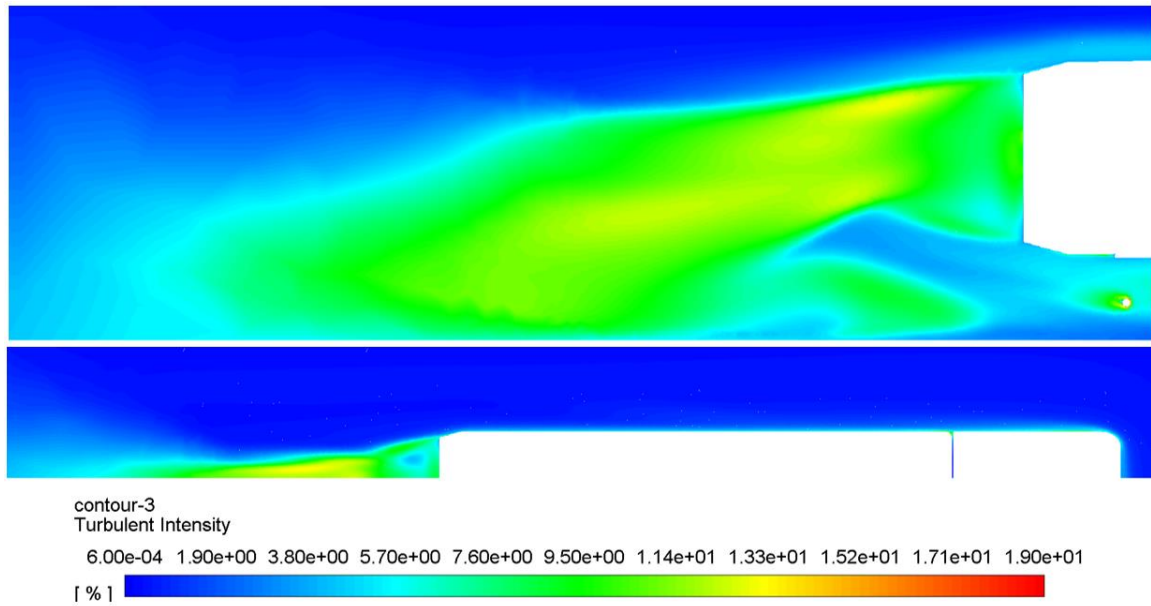


Figure 86. Side view (top) and plan view (bottom) of the airflow turbulent intensity over Concept Two – Revision D.

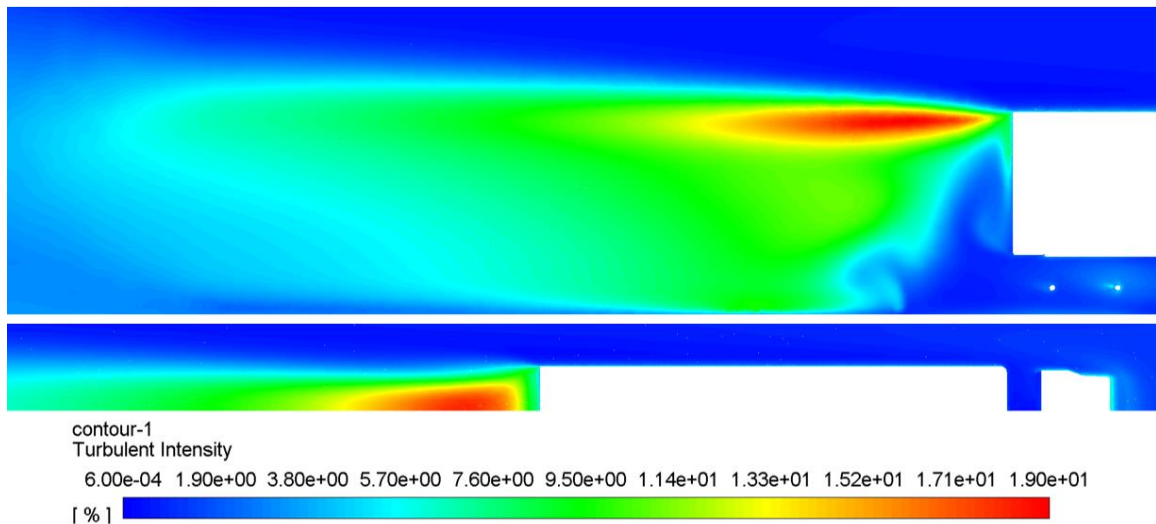
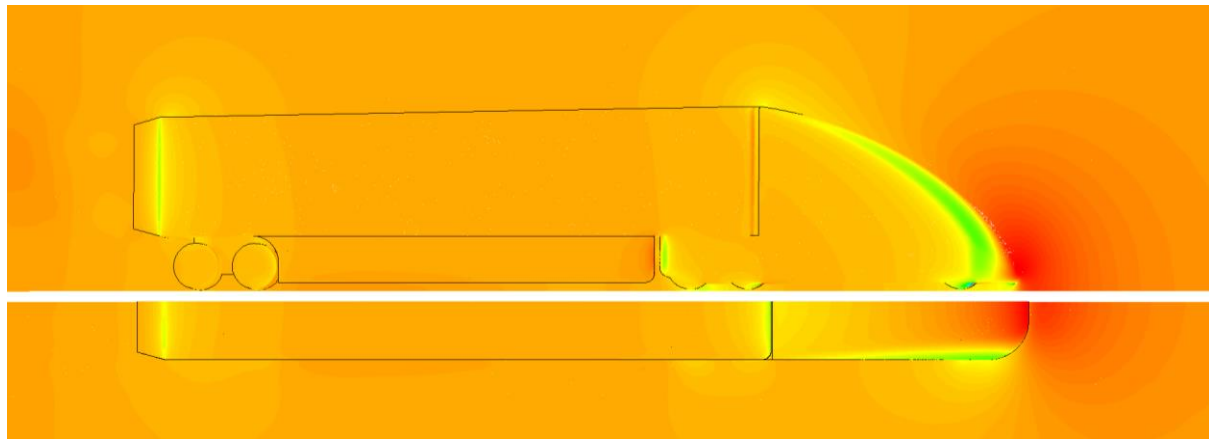


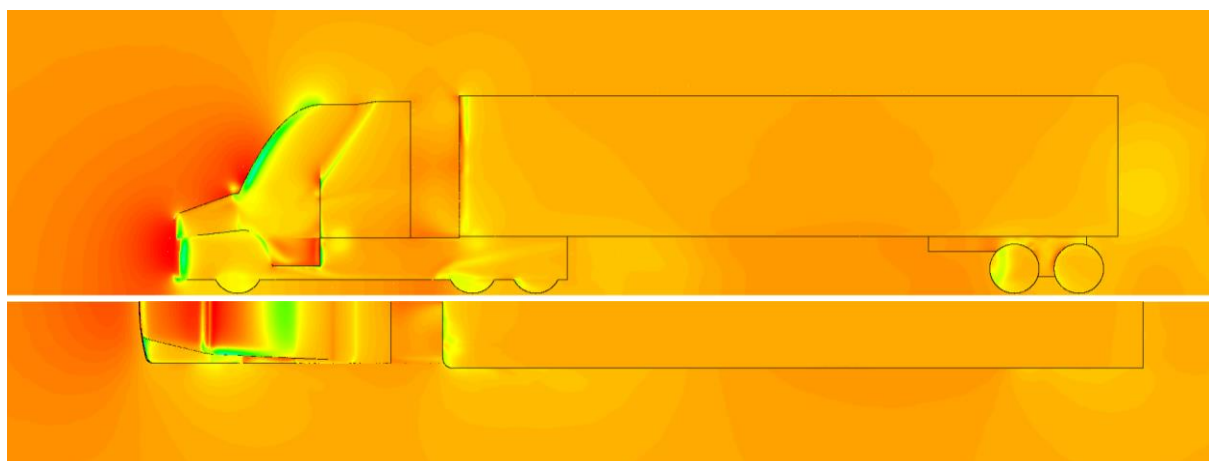
Figure 87. Side view (top) and plan view (bottom) of the airflow turbulent intensity over the GCM.

Figure 88 and 89 below show the pressure coefficient over Concept Two – Revision D and the GCM respectively. The multiple high pressure spots on the GCM tractor have been reduced to a single high pressure zone at the front of the Concept Two – Revision D tractor, with a smoother transition of the airflow over the tractor body. The GCM high pressure zone between the rear of the tractor and the front of the trailer, as seen in Figure 89, is dramatically reduced in Concept Two – Revision D. The GCM also has a localised high pressure zone under the trailer, whereas the pressure distribution is more evenly dispersed and of a lower magnitude in Concept Two - Revision D.



contour-3
Pressure Coefficient
-4.14e+00 -3.63e+00 -3.11e+00 -2.60e+00 -2.08e+00 -1.57e+00 -1.06e+00 -5.42e-01 -2.80e-02 4.86e-01 1.00e+00

Figure 88. Side view (top) and plan view (bottom) of the airflow pressure coefficient over Concept Two – Revision D.



contour-1
Pressure Coefficient
-4.14e+00 -3.63e+00 -3.11e+00 -2.60e+00 -2.08e+00 -1.57e+00 -1.06e+00 -5.42e-01 -2.80e-02 4.86e-01 1.00e+00

Figure 89. Side view (top) and plan view (bottom) of the airflow pressure coefficient over the GCM.

Chapter 8

Conclusion and recommendations

8.1 Conclusion

The aim of this work has been to determine the possible aerodynamic drag reduction for an autonomous BET. There has been a considerable amount of research on large heavy-duty trucks, and on how the aerodynamic drag can be reduced either through ground up design or with the addition of ancillary items.

There has not been a lot of research, however, into the aerodynamic analysis of fully autonomous BETs. The focus of this work was to first understand the requirements for a heavy-duty long-haul truck, and generate an appropriate topology for such a vehicle. With a baseline geometry created, the next steps were to investigate what geometry changes can iteratively be made to the autonomous BET to reduce the overall aerodynamic drag, based on CFD simulations.

This study found that approximately 18% reduction in aerodynamic drag (as shown by Concept Two – Revision A in Table 12) can be gained without the truck owner or logistics company having to invest in trailer modifications such as adding a boat-tail, side skirts, or a tapering trailer roofline.

With low investment options such as a boat tail (Concept Two – Revision B) and trailer side skirts (Concept Two – Revision C), a reduction of aerodynamic drag of approximately 32% and 35.5% respectively is possible. In terms of practicality, maintenance and load space, the boat tail and side skirts have no negative effects.

When a tapered trailer roofline is introduced, the resulting aerodynamic drag is reduced by 37.72% (as shown by Concept Two – Revision D in Table 12), compared to the GCM. There is a reduction in practicality with this solution as the load space is reduced.

The literature review on current technology, as well as on the energy demands of an autonomous BETs found that currently available batteries, electric motors, transmissions and autonomous systems are adequate to meet the driving requirements of a long-haul heavy-duty truck.

A C_D value of 0.260 (as shown by Concept Two – Revision C in Table 12) can be achieved for an autonomous BET compared to 0.403 for a simplified conventional diesel ICE truck (as shown by the GCM in Table 12), with no compromise in load practicality for the autonomous BET.

The findings of this research illustrate the significant gains in energy efficiency that can be achieved with a fully autonomous BET compared to traditional ICE long-haul trucks. This research contributes to the currently small body of work on the subject of drag reduction for autonomous BETs, especially with regard to the tractor nose shape and tractor-trailer gap. The autonomous BET discussed in this research, specifically Concept Two – Revision C, shows that it is currently possible to engineer and manufacture such a vehicle to carry out the long-haul tasks of a traditional ICE truck, using currently available commercial solutions. With reference to the BET roadmap discussed in section 4.10.6, Concept Two – Revision C is suited for application in stage three of this roadmap. The overall reduction in wake size and intensity is significant to future work regarding autonomous truck platooning.

8.2 Recommendations

This research has aimed to remain as practical and achievable as possible with existing technology, retaining a conventional trailer and specifying existing driveline and energy source components. However, a conceptual approach was used and as such there are some recommendations for future work in this area. A few of these recommendations are listed below.

The CFD work provides an overview of the airflow characteristics and the aerodynamic drag, and attention was given to ensure the highest level of accuracy from the simulation for the given computational capacity. These CFD simulation results should be checked against a real world wind tunnel test.

The model should also be evaluated for a full sweep of yaw angles relative to the incoming flow. This is especially useful to characterise the effects of cross wind on the tractor-trailer gap, as well as the side skirt-tractor gap.

The advantage of an autonomous BET is that driver reaction times are not a factor. A possible scenario that results from this is that the trucks can more easily travel in a platoon formation at very close following distances. A platoon formation has the possibility of a reduced aerodynamic drag on the trucks following the lead truck in a platoon. Another aspect to investigate is the reduction in traffic for a city with autonomous BETs travelling in platoon formation on highways.

A more integrated tractor-trailer design can be investigated. With the possibility of autonomous BETs becoming the mainstream long-haul transportation solution by 2050, a more holistic design should be investigated where the trailer works more cohesively with the aerodynamics of the tractor.

References

- Ambel, C.C., Earl, T., Kenny, S., Cornelis, S. & Sihvonen, J. 2017. *Roadmap to climate-friendly land freight and buses in Europe*. [Online] Available at: <https://www.transportenvironment.org/discover/roadmap-climate-friendly-land-freight-and-buses-europe/> [Accessed 01 July 2021].
- Anderson Jr, J.D. 2010. *Fundamentals of aerodynamics*. 5th ed. McGraw-Hill Education.
- ANSYS. 2009. ANSYS FLUENT 12.0 Theory Guide - 18.4.3 Pressure-Velocity Coupling. [Online] Available at: <https://www.afs.enea.it/project/neptunius/docs/fluent/html/th/node373.htm> [Accessed 13 September 2021].
- Arora, S., Abkenar, A.T., Jayasinghe, S.G. & Tammi, K. 2021. *Heavy-duty Electric Vehicles: From Concept to Reality*. 1st ed. Butterwoth-Heinemann.
- Association, E. and T.M.I.R. 2001. Good practice guide 308, truck aerodynamic styling. [Online] Available at: https://trimis.ec.europa.eu/sites/default/files/project/documents/20060210_121817_04842_GPG308.pdf [Accessed 09 July 2021].
- Birk, L. 2019. *Fundamentals of Ship Hydrodynamics: Fluid Mechanics, Ship Resistance and Propulsion*. John Wiley & Sons.
- Campagnol, N., Erriquez, M., Schwedhelm, D., Wu, J., & Wu, T. 2021. *Building better electric batteries for battery electric vehicles*. [Online] Available at: <https://www.mckinsey.com/industries/automotive-and-assembly/our-insights/building-better-batteries-insights-on-chemistry-and-design-from-china#> [Accessed 08 August 2021].
- Cargo-Partner. n.d. *A vehicle named Vera*. [Online] Available at: <https://www.cargo-partner.com/trendletter/issue-13/volvo-vera> [Accessed 10 May 2021].
- Cascadia. 2021. Cascadia Datasheet. [Online] Available at: <https://freightliner.com/trucks/cascadia/> [Accessed 03 July 2021].
- Cazzola, P. & Gerner, M. 2017. *Global EV Outlook 2017: Two million and counting*. [Online] Available at: <https://www.oecd.org/publications/global-ev-outlook-2017-9789264278882-en.htm> [Accessed 01 July 2021].
- Chottani, A. 2018. *Autonomous trucks disrupt US logistics*. [Online] Available at: <https://www.mckinsey.com/industries/travel-logistics-and-infrastructure/our-insights/distraction-or-disruption-autonomous-trucks-gain-ground-in-us-logistics> [Accessed 10 August 2021].
- Cooper, K.R. 2003. Truck aerodynamics reborn - Lessons from the past. *Journal of Commercial Vehicles*, 112: 132-142. doi: 10.4271/2003-01-3376
- Daimler. 2007. *Freightliner Cascadia Is More Aerodynamic than Other Class 8 Vehicles*. [Online] Available at: <https://daimler-trucksnorthamerica.com/company/press-releases/pressdetail/freightliner-cascadia-is-more-aerodynamic-than-2007-08-29> [Accessed 03 July 2021].

- Daimler. 2021. *The new EQS: Aerodynamics*. [Online] Available at: <https://media.daimler.com/marsMediaSite/en/instance/ko/The-new-EQS-Aerodynamics.xhtml?oid=49581781> [Accessed 03 July 2021].
- Dana TM4. 2021. TM4 SUMO HP Datasheet. [Online] Available at: <https://www.danatm4.com/products/systems/sumo-hp/> [Accessed 07 August 2021].
- David, D. 2013. *Camille Jenatzy - Biography*. [Online] Available at: http://www.grandprixhistory.org/jenatzy_bio.htm [Accessed 02 July 2021].
- Davis, A. 2020. *TRL analysis enables legislation to drive greener and safer trucks - Highways Today*. [Online] Available at: <https://highways.today/2020/02/27/trl-safer-trucks/> [Accessed 03 June 2021].
- Den Boer, E., Aarnink, S., Kleiner, F. & Pagenkopf, J. 2013. *Zero emissions trucks. An overview of state-of-the-art technologies and their potential*. [Online] Available at: https://theicct.org/sites/default/files/publications/CE_Delft_4841_Zero_emissions_trucks_Def.pdf [Accessed 01 July 2021].
- Dunietz, J. 2018. *Autonomous Driving Takes Power. Will That Matter for Electrification?*. [Online] Available at: <https://energyfuse.org/autonomous-driving-takes-power-will-that-matter-for-electrification/> [Accessed 06 August 2021].
- E-FORCE ONE AG. 2020. EF26 Datasheet. [Online] Available at: <https://www.eforce.ch/products/ef26> [Accessed 08 August 2021].
- Earl, T., Mathieu, L., Cornelis, S., Kenny, S., Ambel, C.C. & Nix, J. 2018. Analysis of long haul battery electric trucks in EU: marketplace and technology, economic, environmental, and policy perspectives. *8th Commercial Vehicle Workshop, Graz, 17-18 May*.
- Eaton. 2021. 4 speed EV transmission Datasheet. [Online] Available at: <https://www.eaton.com/us/en-us/catalog/emobility/4-speed-ev.specifications.html> [Accessed 09 September 2021].
- European Parliamentary Research Service. 2014. *Weights and dimensions of road vehicles in the EU*. [Online] Available at: <https://epthinktank.eu/2014/04/10/weights-and-dimensions-of-road-vehicles-in-the-eu/> [Accessed 11 August 2021].
- Evans, B.T. 2014. *Autonomous Mercedes-Benz Future Truck 2025 Previews the Future of Shipping*. [Online] Available at: <https://www.motortrend.com/news/1409-autonomous-mercedes-benz-truck-2025-previews-the-future-of-shipping?galleryimageid=2b774fd7-d7e5-464c-9b30-7a0a666f155c> [Accessed 09 August 2021].
- Fan, D., Yang, L., Wang, Z., Triantafyllou, M.S. & Karniadakis, G.E. 2020. Reinforcement learning for bluff body active flow control in experiments and simulations. *Proceedings of the National Academy of Sciences*, 117(42): 26091–26098. doi: 10.1073/pnas.2004939117.
- Federal Highway Administration. 2004. *Federal Size Regulations for Commercial Motor Vehicles*. [Online] Available at: https://ops.fhwa.dot.gov/freight/publications/size_regs_final_rpt/ [Accessed 11 August 2021].

- Feng, Y. & Dong, Z. 2020. Optimal energy management with balanced fuel economy and battery life for large hybrid electric mining truck. *Journal of Power Sources*, 454, 227948. doi: 10.1016/j.jpowsour.2020.227948.
- Genta, G. & Morello, L. 2020. *The Automotive Chassis*. 2nd ed. Berlin: Springer International Publishing.
- Graichen, J. 2016. *Targets for the non-ETS sectors in 2040 and 2050*. [Online] Available at: <https://www.oeko.de/fileadmin/oekodoc/Targets-for-the-non-ETS-sectors-in-2040-and-2050.pdf> [Accessed 09 May 2021].
- Hariram, A., Koch, T., Mårdberg, B. & Kyncl, J. 2019. A study in options to improve aerodynamic profile of heavy-duty vehicles in Europe. *Sustainability*, 11(19):5519. doi: 10.3390/su11195519
- Hill, J. 2021. *Frito-Lay chip factory to host first Tesla Semi 'megacharger' stations*. [Online] Available at: <https://thedriven.io/2021/05/26/frito-lay-chip-factory-to-host-first-tesla-semi-megacharger-stations/> [Accessed 09 August 2021].
- Hjelm, L. & Bergqvist, B. 2009. European truck aerodynamics - A comparison between conventional and CoE truck aerodynamics and a look into future trends and possibilities. In: *Browand F., McCallen R., Ross J. (eds) The Aerodynamics of Heavy Vehicles II: Trucks, Buses, and Trains. Lecture Notes in Applied and Computational Mechanics, vol 41*. Springer, Berlin, Heidelberg. https://doi.org/10.1007/978-3-540-85070-0_45
- Humphreys, L. & Bevly, D. 2016. Computational Fluid Dynamic Analysis of a Generic 2 Truck Platoon. *SAE Technical Papers*. doi:10.4271/2016-01-8008.
- Hyams, D.G., Sreenivas, K., Pankajakshan, R., Nichols, S D., Briley, R. W. & Whitfield, D.L. 2011. Computational simulation of model and full scale Class 8 trucks with drag reduction devices. *Computers and Fluids*, 41(1): 27-40. doi: 10.1016/j.compfluid.2010.09.015
- IEA. 2021. *Global EV Outlook 2021 - Accelerating ambitions despite the pandemic*. [Online] Available at: <https://iea.blob.core.windows.net/assets/ed5f4484-f556-4110-8c5c-4ede8bcba637/GlobalEVOutlook2021.pdf> [Accessed 01 July 2021].
- Katz, J. 2016. *Automotive aerodynamics*. Chichester: John Wiley & Sons.
- Khosravi, M., Osaddeghi, F., Veisi, M. & Hodayari-b, A. 2015. Aerodynamic drag reduction of heavy vehicles using append devices by CFD analysis. *Journal of Central South University*, 22(12): 4645-4652. doi: 10.1007/s11771-015-3015-7
- Kosivi, J., Gomez, J., Nelson, R., Kalu, E.E. & Weatherspoon, M.H. 2014. Non-Paste Based Composite Cathode Electrode for Lithium Air Battery. In *ECS Meeting Abstracts*, MA2014-01: 206. doi: 10.1149/MA2014-01/2/206
- Kouchak, S.M. & Gaffar, A. 2017. Determinism in future cars: why autonomous trucks are easier to design. *IEEE SmartWorld, Ubiquitous Intelligence & Computing, Advanced & Trusted Computed, Scalable Computing & Communications, Cloud & Big Data Computing, Internet of People and Smart City Innovation, SmartWorld/SCALCOM/UIC/ATC/CBDCOM/IOP/SCI 2017*. Institute of Electrical and Electronics Engineers Inc: 1–6. doi: 10.1109/UIC-ATC.2017.8397598
- Krajnović, S. & Davidson, L. 2005. Influence of floor motions in wind tunnels on the aerodynamics of road vehicles. *Journal of Wind Engineering and Industrial*

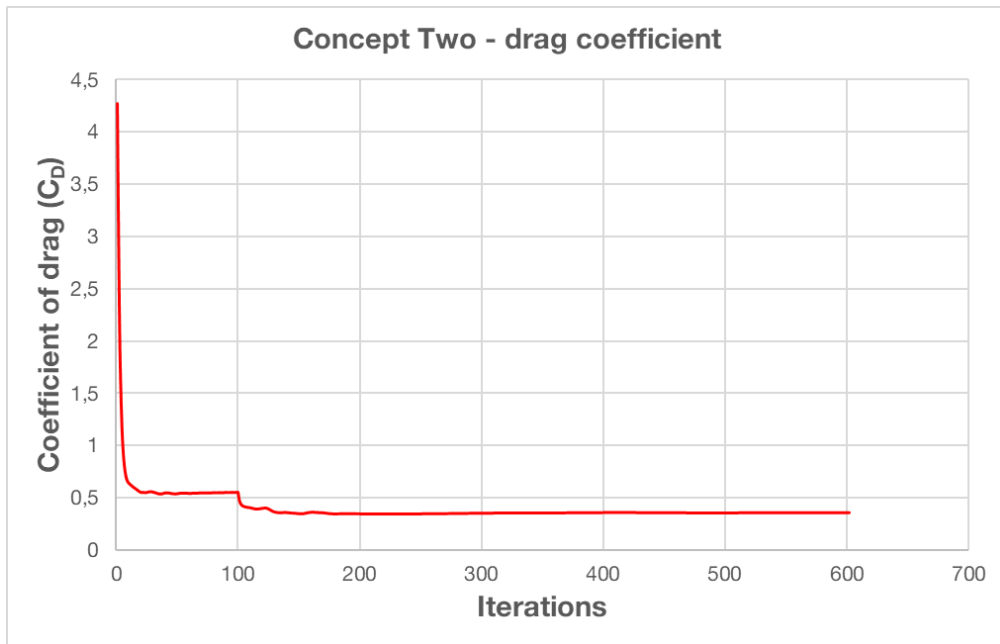
Aerodynamics, 93(9): 677-696. doi: 10.1016/j.jweia.2005.05.002

- Lanfrit, M. 2005. A best practice guideline to handle Automotive External Aerodynamics with FLUENT. *Fluent Inc. Technical Notes*. [Online] Available at: https://www.southampton.ac.uk/~nwb/lectures/GoodPracticeCFD/Articles/Ext_Aero_Best_Practice_Ver1_2.pdf [Accessed 15 July 2021].
- LEAP CFD Team. 2013. *Tips & tricks: Estimating the First Cell Height for correct Y+* [Online] Available at: <https://www.computationalfluidynamics.com.au/tips-tricks-cfd-estimate-first-cell-height/> [Accessed 12 September 2021].
- Liu, S., Li, L., Tang, J., Wu, S. & Gaudiot, J.-L. 2017. Creating autonomous vehicle systems. *Synthesis Lectures on Computer Science*. Morgan & Claypool Publishers.
- Mareev, I., Becker, J. & Sauer, D.U. 2018. Battery dimensioning and life cycle costs analysis for a heavy-duty truck considering the requirements of long-haul transportation. *Energies*, 11(1): 55. doi: 10.3390/en11010055
- Mazaro. n.d. *Pioneering transmission technology*. [Online] Available at: <https://www.mazaro.eu/en/pioneering-transmission-technology> [Accessed 09 August 2021].
- McCallen, R.C., Salari, K., Ortega, J.M., DeChant, L.J., Hassan, B., Roy, C.J., Pointer, W.D., Browand, F., Hammache, M., Hsu, T.Y., Leonard, A., Rubel, M., Chatalain, P., Englar, R., Ross, J., Satran, D., Heineck, J.T., Walker, S., Yaste, D. & Storms, B. 2004. Doe's effort to reduce truck aerodynamic drag - joint experiments and computations lead to smart design. *34th AIAA Fluid Dynamics Conference and Exhibit*. doi: 10.2514/6.2004-2249
- Megan Lampinen. 2021. *New transmission tech could prove game-changing for electrified trucks*. [Online] Available at: <https://www.automotiveworld.com/articles/new-transmission-tech-could-prove-game-changing-for-electrified-trucks/> [Accessed 09 August 2021].
- Miralbes, R. & Castejon, L. 2012. Aerodynamic analysis of some boat tails for heavy vehicles. *International Journal of Heavy Vehicle Systems*, 19(2): 115-127. doi: 10.1504/IJHVS.2012.046830
- Mobility and Transport. n.d. *Intelligent transport systems*. [Online] Available at: https://ec.europa.eu/transport/themes/its/road_it [Accessed 30 May 2021].
- Mohamed-Kassim, Z. & Filippone, A. 2010. Fuel savings on a heavy vehicle via aerodynamic drag reduction. *Transportation Research Part D: Transport and Environment*, 15(5): 275-284. doi: 10.1016/J.TRD.2010.02.010
- Morozov, A., Humphries, K., Zou, T., Rahman, T. & Angeles, J. 2018. Design, Analysis, and Optimization of a Multi-Speed Powertrain for Class-7 Electric Trucks. *SAE International Journal of Alternative Powertrains*, 7(1): 27-42. doi:10.4271/08-07-01-0002
- Moultak, M., Lutsey, N. & Hall, D. 2017. *Transitioning to zero-emission heavy-duty freight vehicles*. [Online] Available at: https://theicct.org/sites/default/files/publications/Zero-emission-freight-trucks_ICCT-white-paper_26092017_vF.pdf [Accessed 09 May 2021].

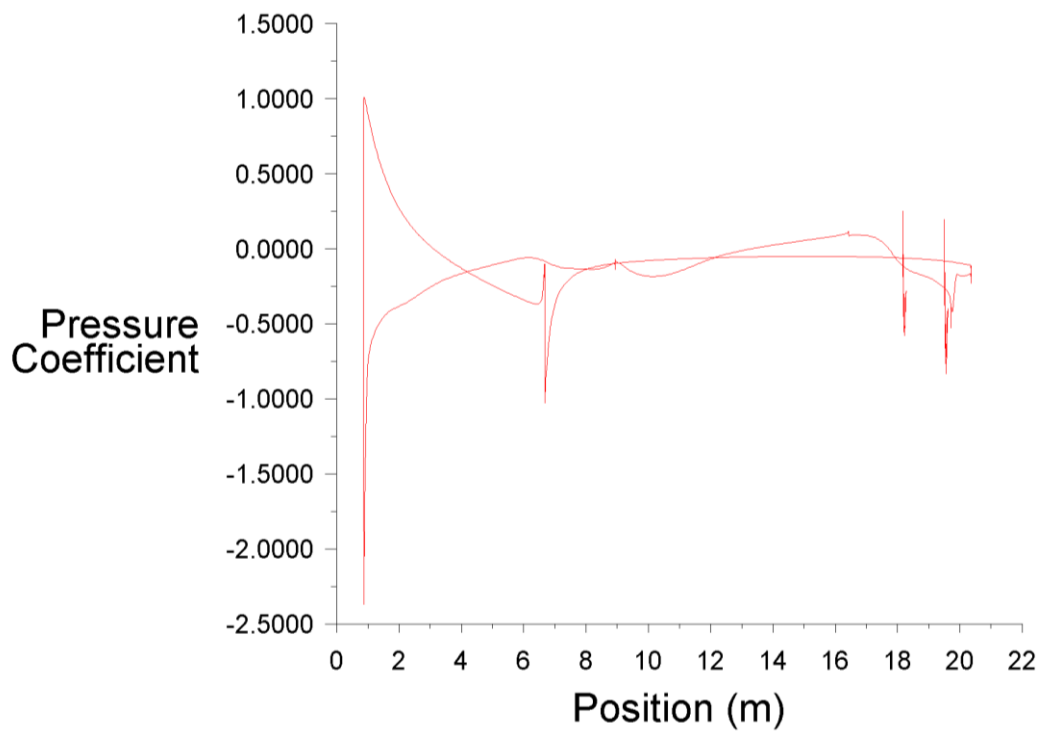
- National Academies of Sciences and Medicine. 2020. *Reducing fuel consumption and greenhouse gas emissions of medium-and heavy-duty vehicles, Phase Two*. [Online] Available at: <https://www.nap.edu/catalog/25542/reducing-fuel-consumption-and-greenhouse-gas-emissions-of-medium-and-heavy-duty-vehicles-phase-two> [Accessed 08 August 2021]. doi: 10.17226/25542
- Nunn, R.H. 2018. *Intermediate fluid mechanics*. New York: Routledge.
- Petit, F. 2020. *How sensors enable autonomous driving*. [Online] Available at: <https://www.blickfeld.com/blog/sensor-fusion-for-autonomous-driving/> [Accessed 29 May 2021].
- Proterra. 2021. *The Proterra Battery Platform*. [Online] Available at: <https://www.proterra.com/proterra-powered/battery-technology/> [Accessed 08 August 2021].
- Ramey, J. 2017. *Self-driving systems need lots of power. So do EV motors. That's a problem*. [Online] Available at: <https://www.autoweek.com/news/technology/a1832781/brain-drain-autonomous-systems-require-lot-power/> [Accessed 06 August 2021].
- Sanguesa, J.A., Torres-Sanz, V., Garrido, P., Martinez, F.J. & Marquez-Barja, J.M. 2021. A Review on Electric Vehicles: Technologies and Challenges. *Smart Cities*, 4(1): 372-404. doi: 10.3390/SMARTCITIES4010022
- Satran, D. 2004. An experimental study of the generic conventional model (gcm) in the nasa ames 7-by-10-foot wind tunnel. *The Aerodynamics of Heavy Vehicles: Trucks, Buses, and Trains*, 171. doi: 10.1007/978-3-540-44419-0_18
- Sclar, R., Gorguinpour, C., Castellanos, S. & Li, X. 2019. *Barriers to adopting electric buses*. [Online] Available at: <https://www.wri.org/research/barriers-adopting-electric-buses> [Accessed 10 August 2021].
- Selenbas, B., Gunes, H., Gocmen, K., Bahceci, U. & Bayram, B. 2010. An aerodynamic design and optimization of a heavy truck for drag reduction. In *ASME 2010 10th Biennial Conference on Engineering Systems Design and Analysis, ESDA2010*, 3:121-129. doi: 10.1115/ESDA2010-24482
- Singh, S. 2018. *Critical reasons for crashes investigated in the National Motor Vehicle Crash Causation Survey*. [Online] Available at: <https://crashstats.nhtsa.dot.gov/Api/Public/ViewPublication/812506> [Accessed 31 May 2021].
- Skrucany, T., Sarkan, B. & Gnap, J. 2016. Influence of aerodynamic trailer devices on drag reduction measured in a wind tunnel. *Eksploatacja i Niezawodnosc - Maintenance and Reliability*, 18(1): 151-154. doi: 10.17531/ein.2016.1.20
- Storms, B.L., Satran, D.R., Heineck, J.T. & Walker, S.M. 2006. *A summary of the experimental results for a generic tractor-trailer in the ames research center 7-by 10-foot and 12-foot wind tunnels*. [Online] Available at: <https://ntrs.nasa.gov/api/citations/20060051856/downloads/20060051856.pdf> [Accessed 03 June 2021].
- Talay, T.A. 1975. *Introduction to the aerodynamics of flight*. [Online] Available at: <https://ntrs.nasa.gov/api/citations/19760003955/downloads/19760003955.pdf> [Accessed 09 July 2021].

- Tashakori, A., Ektesabi, M. & Hosseinzadeh, N. 2011. Characteristics of suitable drive train for electric vehicle. *International Conference on Instrumentation, Measurement, Circuits and Systems (ICIMCS)*, 2: 51-5. doi: 10.1115/1.859902.paper119
- Tu Simple. 2021. *Self-Driving Technology Designed For Trucks*. [Online] Available at: <https://www.tusimple.com/technology/> [Accessed 10 August 2021].
- Verbruggen, F.J.R., Silvas, E. & Hofman, T. 2020. Electric powertrain topology analysis and design for heavy-duty trucks. *Energies*, 13(10): 2434. doi: 10.3390/EN13102434
- Versteeg, H.K. & Malalasekera, W. 2007. *An Introduction to the fluid dynamics - The Finite Volume Method*. 2nd ed. Harlow: Pearson Education Limited.
- Verster, T. & Fourie, E. 2018. The good, the bad and the ugly of South African fatal road accidents. *South African Journal of Science*, 114(7–8). doi: 10.17159/SAJS.2018/20170427.
- Volvo. 2018. *Ground-breaking innovations for future autonomous and electric transport solutions*. 2018. [Online] Available at: <https://www.volvogroup.com/en/news-and-media/news/2018/sep/news-3048902.html> [Accessed 09 May 2021].
- World Health Organization. 2018. *Global status report on road safety 2018*. [Online] Available at: <https://www.who.int/publications/i/item/9789241565684> [Accessed 30 May 2021].
- Weiss, C.. 2021. *478-mile Mercedes EQS brings top-of-range electric luxury*. [Online] Available at: <https://newatlas.com/automotive/mercedes-eqs-debut/> [Accessed 03 July 2021].
- Wendt, J.F. 2008. *Computational fluid dynamics: an introduction*. 3rd ed. Heidelberg: Springer Science & Business Media.
- Wolff, S., Kalt, S., Bstieler, M. & Lienkamp, M. 2021. Influence of powertrain topology and electric machine design on efficiency of battery electric trucks – a simulative case-study. *Energies*, 14(2): 328. doi: 10.3390/en14020328
- Wood, R.M. 2006. A Discussion of a Heavy Truck Advanced Aerodynamic Trailer System. *International Forum for Road Transport Technology (IFRTT) 9th International Symposium on Heavy Vehicle Weights and Dimensions*.
- Yeong, D.J., Velasco-hernandez, G., Barry, J. & Walsh, J. 2021. Sensor and sensor fusion technology in autonomous vehicles: A review. *Sensors*, 21(6): 2140. doi: 10.3390/s21062140

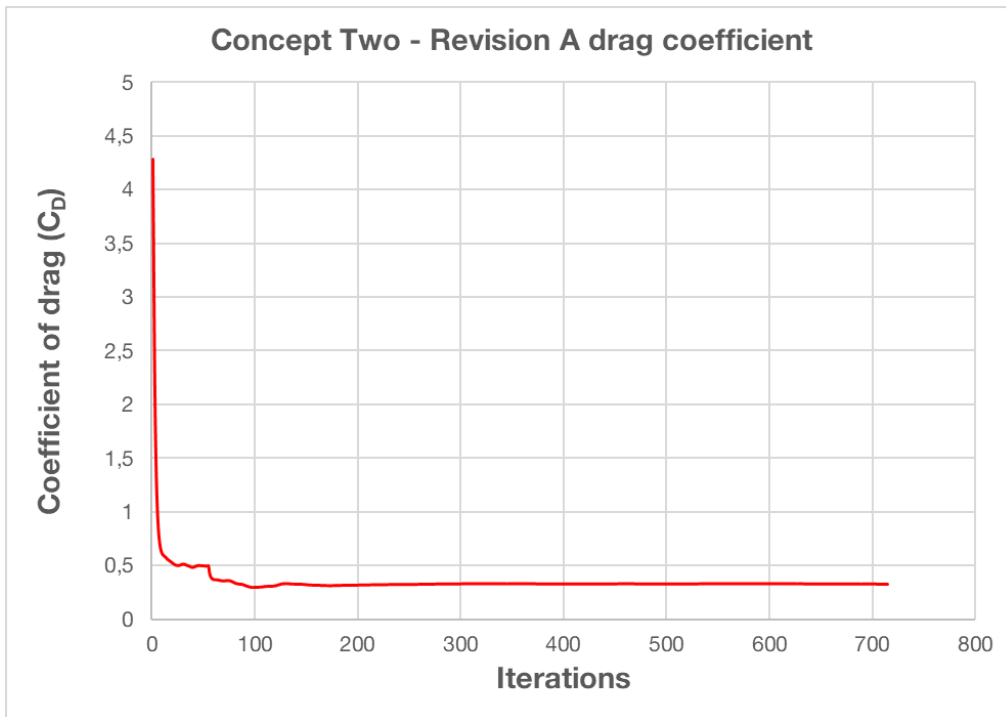
Appendix



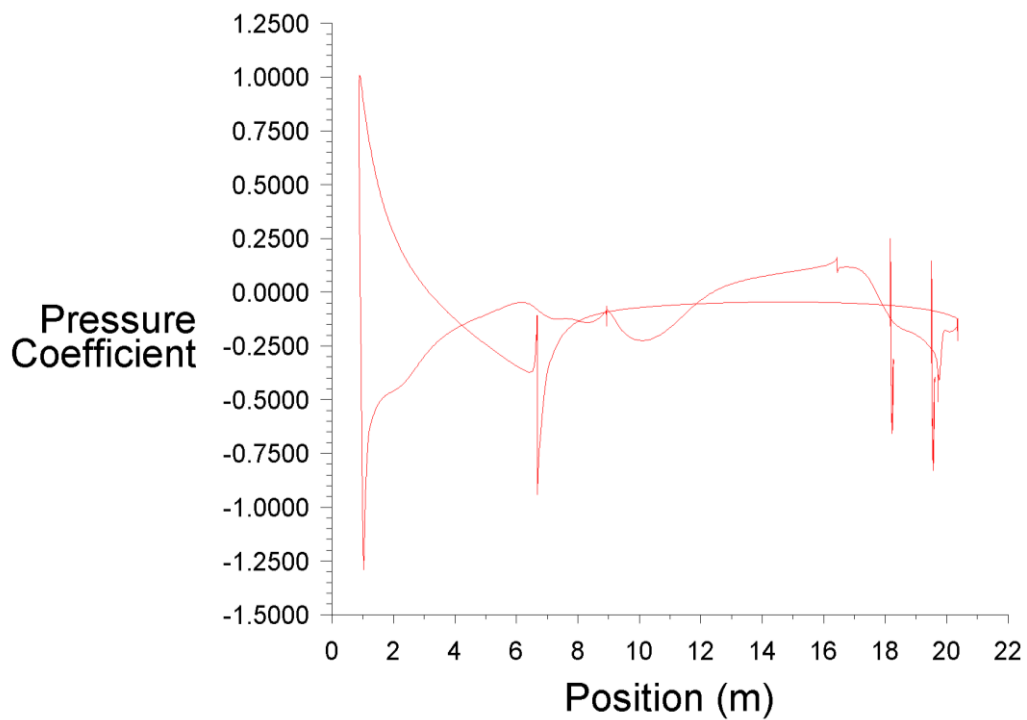
Concept Two – Drag convergence plot.



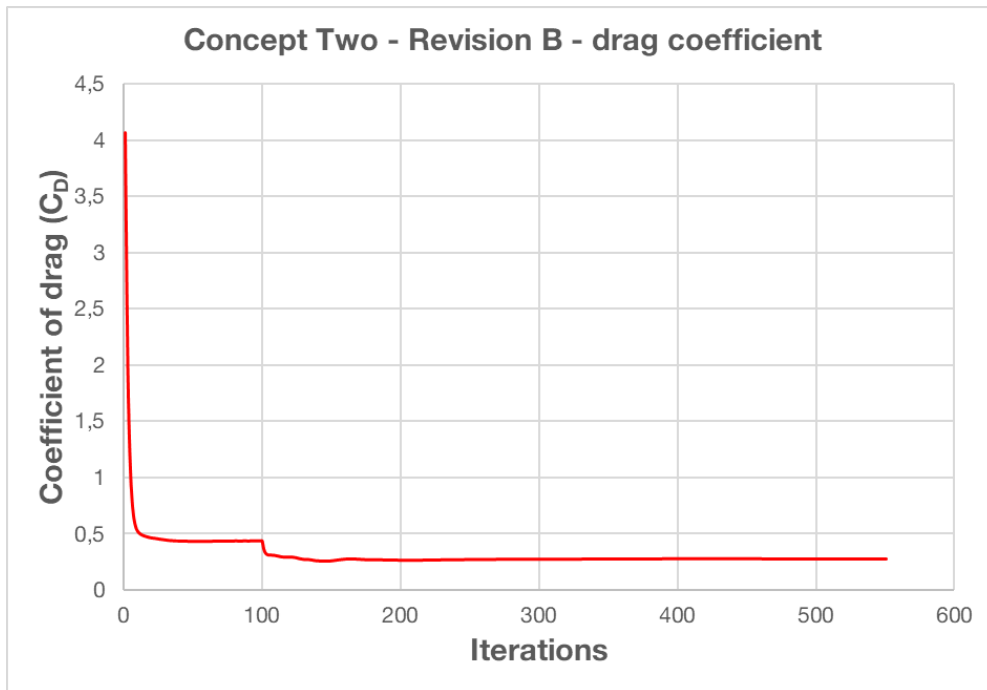
Concept Two – Plot of the pressure coefficient over the body, measured along the longitudinal axis of the vehicle.



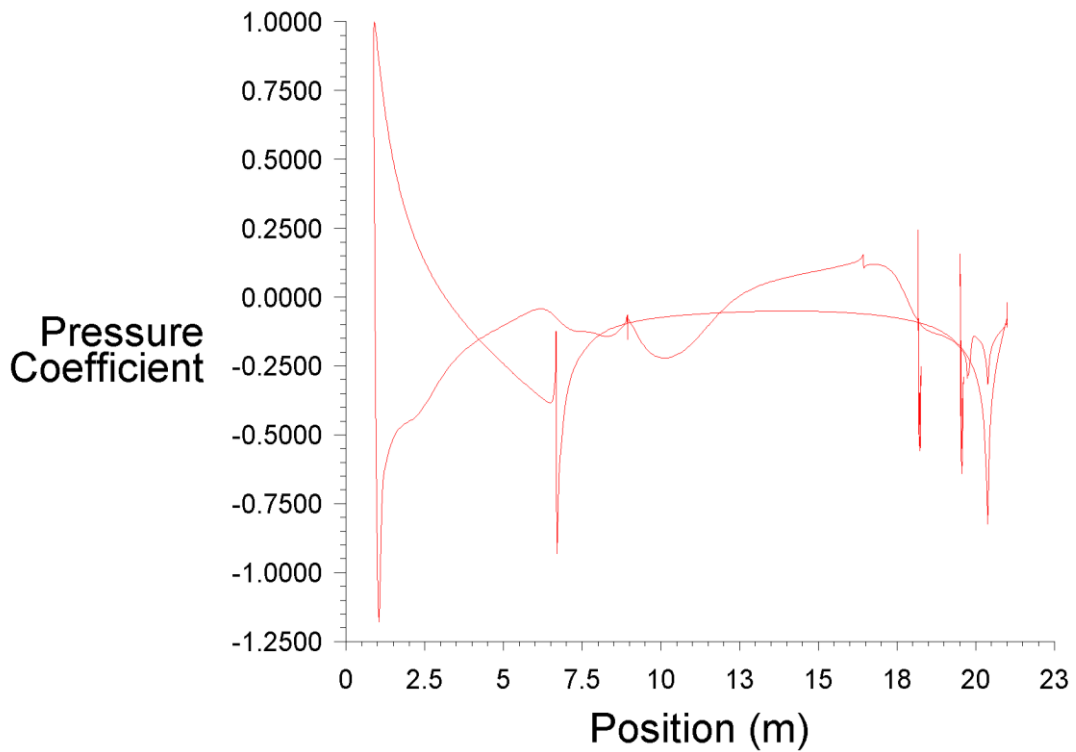
Concept Two – Revision A – Drag convergence plot.



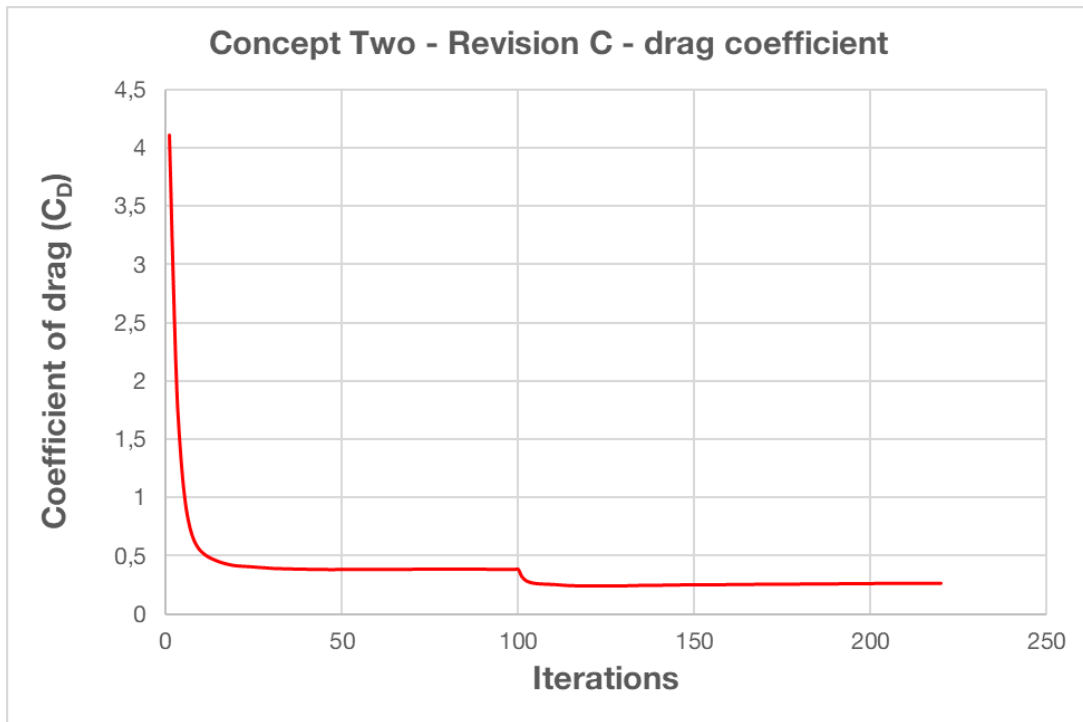
Concept Two – Revision A – Plot of the pressure coefficient over the body, measured along the longitudinal axis of the vehicle.



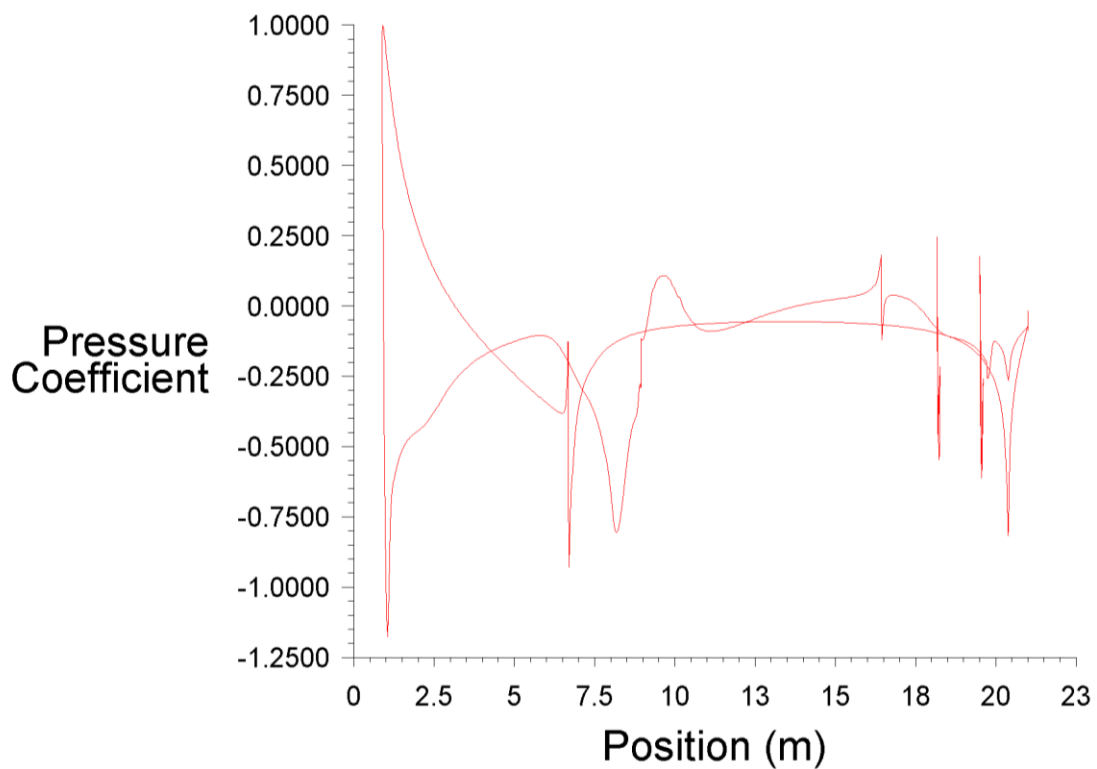
Concept Two – Revision B – Drag convergence plot.



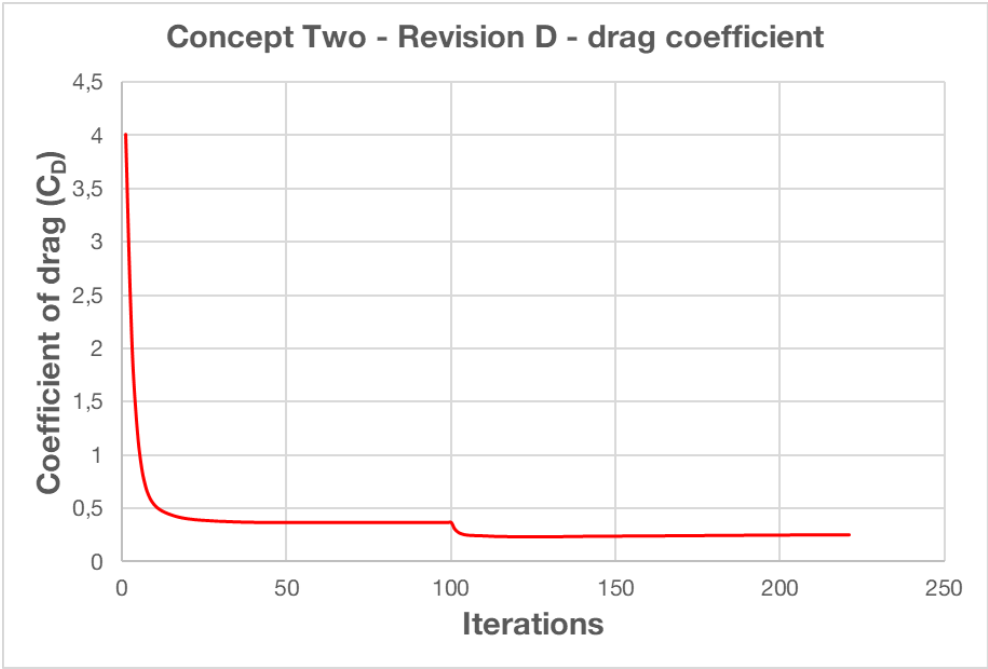
Concept Two – Revision B – Plot of the pressure coefficient over the body, measured along the longitudinal axis of the vehicle.



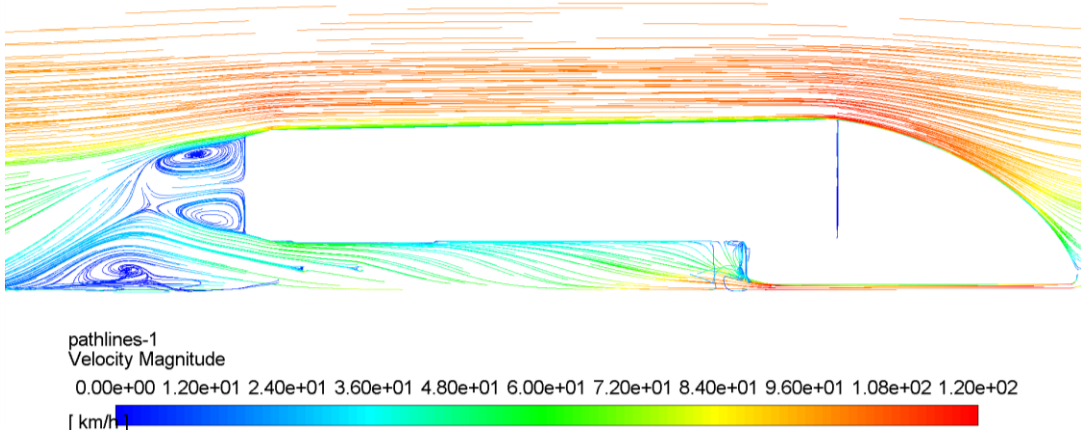
Concept Two – Revision C – Drag convergence plot.



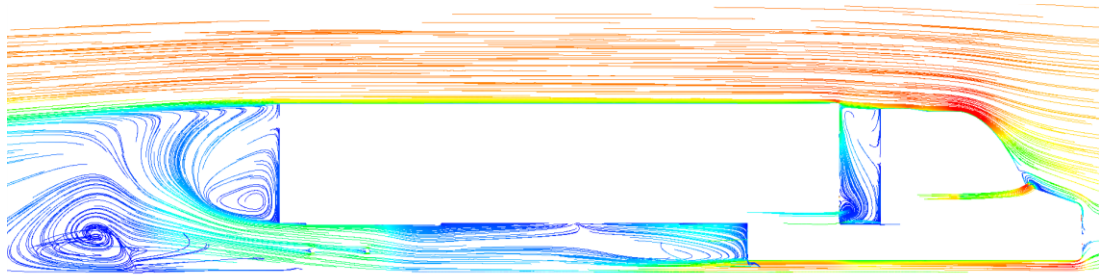
Concept Two – Revision C – Plot of the pressure coefficient over the body, measured along the longitudinal axis of the vehicle.



Concept Two – Revision D – Drag convergence plot.

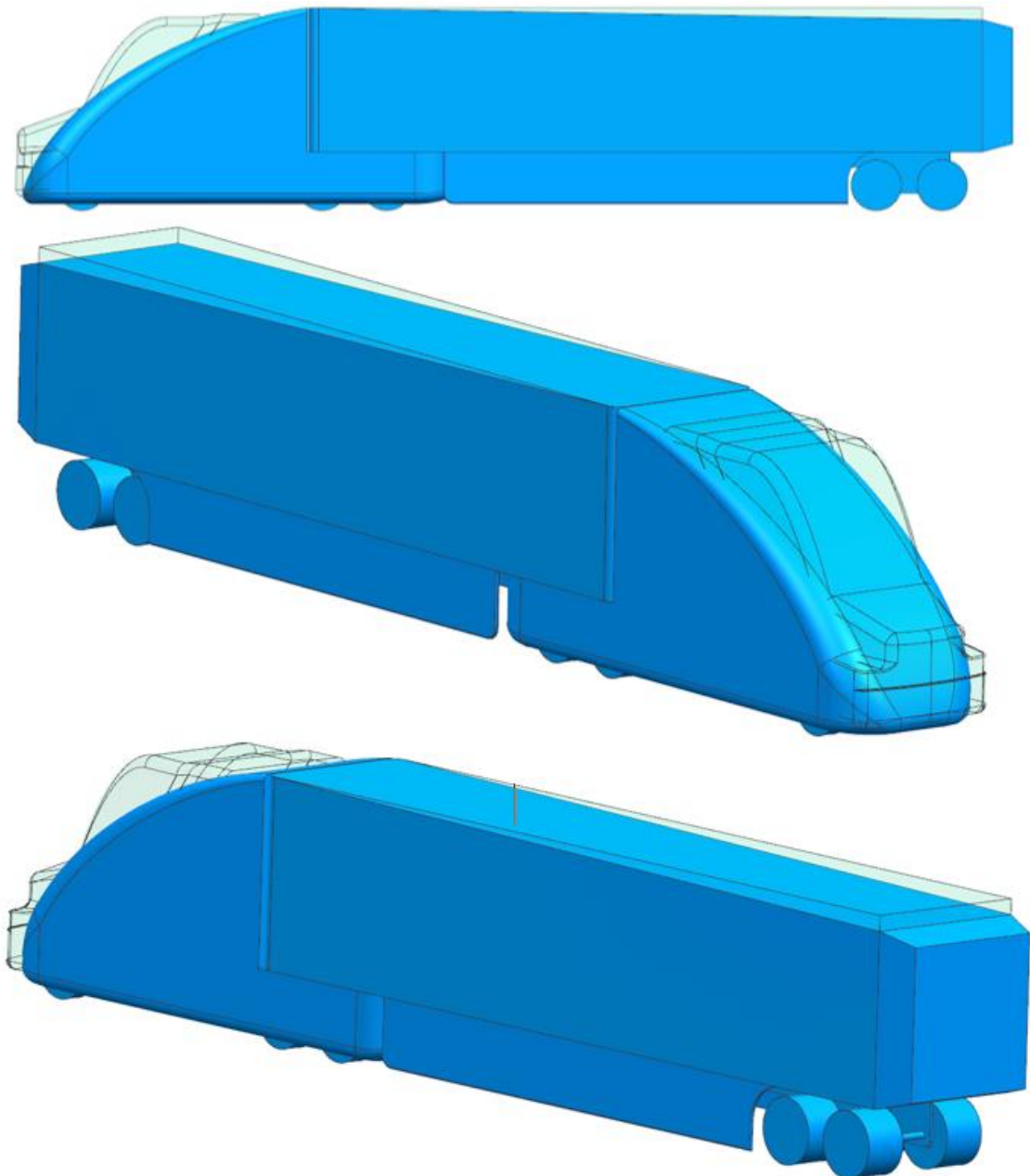


Concept Two – Revision D flow velocity magnitude.



pathlines-1
Velocity Magnitude
0.00e+00 1.20e+01 2.40e+01 3.60e+01 4.80e+01 6.00e+01 7.20e+01 8.40e+01 9.60e+01 1.08e+02 1.20e+02
[km/h]

GCM flow velocity magnitude.



Geometry comparison between Concept Two – Revision D (Solid blue) and the GCM (Transparent green).